

# KNOSOS:

## KiNetic Orbit-averaging SOlver for Stellarators



Technical Documentation and User Manual

Version 1 (last revised, November 16, 2019)

**KNOSOS** is a freely available open-source code. You are very welcome to use it and/or to contribute to its development. It is also under continuous development, which means that, although it has been benchmarked, it might contain minor bugs and that its documentation may be incomplete. We are very happy to receive any feedback, which you can send us to

[joseluis.velasco@ciemat.es](mailto:joseluis.velasco@ciemat.es).

**KNOSOS** is part of a long-term project\* aimed at the study of kinetic transport of multispecies plasmas of stellarators, in collaboration with researchers from the National Fusion Laboratory at CIEMAT (Spain), the University of Oxford (United Kingdom), the Max-Planck Institute for Plasma Physics, Greifswald (Germany) and the National Institute for Fusion Science (Japan). You can learn about our work and interests, which cover topics from the theory of energy transport in optimized stellarators to the experimental validation of impurity transport modelling in real stellarators, on our website

<http://fusionsites.ciemat.es/multitranstell/>,

on the websites of our previous projects

<http://fusionsites.ciemat.es/stellaratortransport/>,  
<http://fusionsites.ciemat.es/kinetictransport/>,

and on the personal website

<http://fusionsites.ciemat.es/jlvelasco/>.

\* The work is carried out within the framework of the EUROfusion Consortium and has received funding from the Euratom research and training programme 2014-2018 under grant agreement No 633053. The views and opinions expressed herein do not necessarily reflect those of the European Commission. It has also been supported in part by grant ENE2015-70142-P of the Ministerio de Economía y Competitividad, Spain, and by grant PGC2018-095307-B-I00, Ministerio de Ciencia, Innovación y Universidades, Spain.

# Contents

<b>1</b>	<b>Introduction</b>	<b>6</b>
1.1	Main features . . . . .	7
1.2	Limitations . . . . .	8
<b>2</b>	<b>Motivation and scope</b>	<b>9</b>
<b>3</b>	<b>Equations</b>	<b>12</b>
<b>4</b>	<b>Solution of the equations</b>	<b>17</b>
4.1	Final expression of the drift-kinetic equation . . . . .	17
4.2	Calculation of the coefficients of the drift-kinetic equation . . . . .	18
4.2.1	Analytical calculation of the divergences of some bounce-integrals . . . . .	19
4.2.2	Evaluation of the magnetic field strength along a field line . . . . .	20
4.3	Spatial and velocity grid . . . . .	21
4.4	Discretization of the drift-kinetic equation . . . . .	24
4.5	Solution of the quasineutrality equation . . . . .	30
<b>5</b>	<b>Installing KNOSOS</b>	<b>32</b>
5.1	Public repository . . . . .	32
5.2	Setting up KNOSOS on a new system . . . . .	32
5.2.1	System requirements . . . . .	32
5.2.2	Makefile . . . . .	33
5.2.3	Next steps . . . . .	33
<b>6</b>	<b>Running KNOSOS</b>	<b>34</b>
6.1	General workflow . . . . .	34
6.2	How to run KNOSOS . . . . .	35
6.2.1	Model . . . . .	35
6.2.2	Species . . . . .	36
6.2.3	Plasma profiles . . . . .	36
6.2.4	Magnetic configuration . . . . .	37
6.2.5	Parameters . . . . .	37
<b>7</b>	<b>Inputs</b>	<b>39</b>
7.1	The <code>model</code> namelist . . . . .	39
7.2	The <code>parameters</code> namelist . . . . .	53

7.3	The <code>surfaces</code> namelist . . . . .	63
7.4	The <code>species</code> namelist . . . . .	65
<b>8</b>	<b>Plasma profiles</b>	<b>69</b>
8.1	Workflow . . . . .	69
8.2	Kinetic profiles . . . . .	69
8.3	Scan in the plasma parameters . . . . .	72
8.4	Error estimates . . . . .	73
<b>9</b>	<b>Magnetic configuration</b>	<b>74</b>
9.1	Workflow . . . . .	74
9.2	Input magnetic field . . . . .	75
9.3	Some useful quantities in Boozer coordinates . . . . .	76
9.4	From VMEC left-handed coordinates to standard right-handed coordinates . . . . .	78
9.5	Relation between Fourier expansions . . . . .	81
9.6	Scan in the magnetic configuration parameters . . . . .	81
<b>10</b>	<b>Output parameters</b>	<b>83</b>
10.1	Standard output and standard error, warnings . . . . .	83
10.2	<code>B.map</code> . . . . .	84
10.3	<code>results.knosos</code> : monoenergetic transport coefficients . . . . .	84
10.4	<code>knosos.dk</code> . . . . .	84
10.5	<code>varphi1.map</code> . . . . .	84
10.6	<code>varphi1.modes</code> . . . . .	85
10.7	<code>flux.amb</code> . . . . .	85
10.8	<code>knososTASK3D.flux</code> . . . . .	85
10.9	<code>flux.modes</code> . . . . .	85
10.10	<code>flux.knosos</code> . . . . .	86
10.11	<code>knososTASK3D.ambEr</code> . . . . .	86
10.12	<code>flux.av</code> . . . . .	86
10.13	<code>imp.knosos</code> . . . . .	86
10.14	??.???. <code>2d.in</code> . . . . .	87
<b>11</b>	<b>Examples</b>	<b>88</b>
11.1	DKES-like monoenergetic transport coefficients . . . . .	88
11.2	Effect of the tangential magnetic drift on the radial transport of energy . . . . .	94
11.3	Tangential electric field . . . . .	97
<b>12</b>	<b>Concluding remarks</b>	<b>103</b>
<b>A</b>	<b>High collisionalities</b>	<b>104</b>
A.1	Bulk species in the Pfirsch-Schlüter regime . . . . .	104
A.2	Bulk species in the plateau regime . . . . .	106
A.3	Classical flux and neoclassical flux of trace impurities species in the presence of bulk ions at low collisionalities . . . . .	108

<b>B DKES</b>	<b>109</b>
B.1 Input . . . . .	109
B.2 Use of DKES database . . . . .	110
B.3 Normalization . . . . .	111

# Chapter 1

## Introduction

**KNOSOS** (KiNetic Orbit-averaging SOlver for Stellarators) is a freely available, open-source code that calculates local neoclassical transport (i.e. transport caused by inhomogeneities of the magnetic field and collisions) in low-collisionality plasmas of three-dimensional magnetic confinement devices. This includes stellarators (helias, heliotrons, quasisymmetric devices, heliacs...) and perturbed tokamaks.

The main difference with respect to other local neoclassical codes is that **KNOSOS** relies on the orbit-averaging technique, which makes it very fast, since it allows to remove one of the coordinates of the problem. The code solves a drift-kinetic equation for each species with two independent variables: the angle  $\alpha$  that labels magnetic field lines on a flux-surface and the pitch angle  $\lambda$ ; the radial coordinate  $\psi$  and the particle speed  $v$  are parameters, and the gyro-angle and the spatial coordinate along the magnetic field line  $l$  have been removed by gyro-averaging and orbit-averaging of the equations, respectively. It should be emphasized that, as we will discuss in forthcoming chapters, orbit-averaging does not imply a simplification on the treatment of the magnetic geometry of the stellarator: it can be done rigorously, and the code recovers, for real stellarators and at low collisionalities, the results (radial fluxes, variation of the electrostatic potential along the flux-surface, etc) of local neoclassical codes that do not perform orbit-averaging.

After this short overview, the rest of the manual is organized as follows: chapter 2 explains the motivation and scope of this project. Chapter 3 presents the equations solved by the current version of **KNOSOS**, using methods described in chapter 4. Chapter 5 contains the instructions to set up the code, and chapter 6 shows how to run it. The details are given in the rest of the manual: chapter 7 lists the input files and their variables, chapter 8 describes how the plasma profiles are read and processed, and chapter 9 does the same thing with the magnetic configuration; chapter 10 lists the output files and describes their content. Finally, chapter 11 shows some examples of simulations that can be reproduced by the user. Chapter 12 provides some concluding remarks, and there are two appendices: appendix A derives the additional equations that are solved for high-collisionality regimes; appendix B shows how to use DKES results as input for **KNOSOS**, or how to compare monoenergetic simulations of the two codes.

This manual describes “version 1” of **KNOSOS**, the one used in [Velasco et al., 2019]\*. We

---

\*The source code itself has also comments, but they often look like [this](#).

note that the code is still under development.

## 1.1 Main features

Below we list the main features of the code, which will be explained in detail in later chapters:

- KNOSOS can read realistic magnetic equilibria in Boozer coordinates, generated e.g. with VMEC plus `BOOZER_XFORM` or `COTRANS`, as well as model magnetic fields.
- Bounce-averaging, combined with the monoenergetic approximation, reduces the number of variables to 2 (to be compared to 3 in the case of DKES, 4 in radially local codes such as `EUTERPE` and `SFINCS`, and 5 in radially global codes such as `FORTEC-3D`). This makes the code very fast, while retaining the physics necessary to describe important features of neoclassical transport at low collisionalities.
- In particular, the magnetic drift tangential to the flux-surface, which gives rise to the superbanana-plateau regime, can be retained, including the effect of the magnetic shear.
  - These calculations have been benchmarked against `FORTEC-3D`<sup>†</sup> and analytical expressions.
- The variation of the electrostatic potential on the flux-surface  $\varphi_1$  can be calculated by solving consistently the drift-kinetic and the quasineutrality equations. The computing time is  $\sim$ 1 minute in a single computer.
  - These calculations have been benchmarked against `EUTERPE`.
- The code typically calculates the radial fluxes for given input density and temperature profiles, but it can also provide a set of *monoenergetic* transport coefficients for later use by transport solvers. The computing time is  $\sim$ seconds in a single computer.
  - These calculations have been benchmarked against `DKES`.
- KNOSOS can calculate the effective ripple in the same manner as NEO does, but it can also provide figures of merit of neoclassical transport for low-collisionality regimes different than the  $1/\nu$  (namely, the  $\sqrt{\nu}$  and `superbanana-plateau` regimes).
- The calculated fluxes are moments the distribution function, which is explicitly computed and `can be provided` in the output, for its use by e.g. gyrokinetic codes.
- KNOSOS has been combined with analytical formulas to provide fast computations of impurity transport in several neoclassical regimes.
- KNOSOS can be used from the `neotransp` suite developed at IPP and from the `TASK3D` suite developed at NIFS.

---

<sup>†</sup>Red color means "to do" or "in progress".

## 1.2 Limitations

- KNOSOS assumes that closed magnetic surfaces exist; magnetic islands and regions of stochastic fields or open field lines cannot be described.
  - Regions in which the rotational transform is close to being a (low-order) rational number **may be** numerically hard to converge.
- The bounce-averaged technique is limited to low collisionalities: if the contribution from the plateau or Pfirsch-Schlüter regimes is not negligible, the calculation with KNOSOS will not be accurate.
  - The appendices describe semianalytical methods to cover these regimes.
  - KNOSOS can be used in combination with DKES and then employed to calculate the radial fluxes for arbitrary collisionality correctly including the effect of the tangential magnetic drift.
- KNOSOS is, as most neoclassical codes, radially local: finite-orbit effects (that arise when the size of radial excursions of the particles from the flux surface are large as compared with other radial scales of the problem) cannot be described.
- KNOSOS considers non-negligible but small  $\varphi_1$ , so that e.g. the bounce points are not altered by it.
  - These effects are typically small if the stellarator is optimized with respect to neoclassical transport.
- Collisions are described by a pitch-angle-scattering collision operator that does not conserve momentum or energy. This is correct for low-collisionality regimes of large aspect-ratio devices.
- Only the part of the distribution function that is even in the parallel velocity is computed, which means that the parallel flows are not calculated.

Some of these limitations will be removed in the near future (and you are very welcome to contribute to this!).

## Chapter 2

# Motivation and scope

\* Stellarators are non-axisymmetric devices in which the magnetic field is created basically by external magnets, without the need of any mechanism to drive current within the plasma. This provides them with an inherent capability for steady state operation and makes them less prone to plasma magnetohydrodynamic instabilities, but it also generally produces larger energy losses: at low collisionalities, the combination of magnetic geometry and particle collisions leads to a variety of stellarator-specific neoclassical transport regimes, which usually give a large contribution to the radial energy and particle transport in the core of the device [Dinklage et al., 2013; Dinklage and the W7-X Team, 2018]. Of special relevance are the  $1/\nu$ , the  $\sqrt{\nu}$  and the superbanana-plateau regimes [Ho and Kulsrud, 1987; Beidler et al., 2011; Calvo et al., 2017], in which the energy transport coefficients show a positive temperature dependence, much more unfavourable than the negative  $T^{-1/2}$  scaling of the banana regime of the axisymmetric tokamak.

The fundamental reason for this behaviour is that in a generic stellarator, unlike in an axisymmetric tokamak, trapped particle orbits have non-zero secular radial drifts. The exception are omnigenous stellarators: in these magnetic configurations, the secular radial drifts vanish [Cary and Shasharina, 1997; Parra et al., 2015], and the level of neoclassical transport is low, similar to that of the tokamak. Quasisymmetric stellarators [Boozer, 1983] are a particular family of omnigenous stellarators, see e.g. [Landreman and Catto, 2012].

The two world's largest stellarators in operation, Wendelstein 7-X (W7-X) [Klinger et al., 2017; Wolf and et al., 2017] and the Large Helical Device (LHD) [Takeiri and the LHD team, 2017], have relied on optimization of neoclassical transport for their design and operation. The magnetic configuration of W7-X has been designed to be close to omnogeneity with poloidally-closed contours of the magnetic field strength; one of the goals of the project has been to prove the constructability and reliability of such designs [Sunn-Pedersen et al., 2016]. In LHD, the plasma column can be shifted inwards so that the minimum values of the magnetic field along the field line have approximately the same value (see figure 2 of [Beidler et al., 2011]), a well-known geometric property of some omnigenous magnetic fields [Mynick et al., 1982; Landreman and Catto, 2012]; discharges performed using this magnetic configuration consistently show better energy confinement [Yamada et al., 2005]. Finally, a particular kind of quasisymmetry, quasaxisymmetry, was the design criterion of the National Compact Stellarator Experiment (NCSX) [Zarnstorff et al., 2001]. Power

---

\*This chapter corresponds to the introduction of [Velasco et al., 2019].

reactor designs exist for these three stellarator concepts [Sagara et al., 2010].

It is then clear that optimization of neoclassical transport is a crucial issue for a stellarator reactor. One of the most common goals of stellarator optimization efforts is the minimization of the so-called *effective ripple*, a figure of merit that provides information of the level of transport in the  $1/\nu$  regime. While there is little doubt that minimization of this quantity should be a design criterion in any future stellarator, it has important limitations. On the one hand, empirical studies of the energy confinement time of several devices aimed at obtaining a unified International Stellarator Scaling law (ISS04) have not shown a very strong correlation between reduced effective ripple and improved energy confinement [Yamada et al., 2005; Fuchert et al., 2018]; on the other hand, self-consistent neoclassical transport simulations performed in the configuration space of W7-X, complemented with simplified anomalous modelling (accounting for non-negligible turbulent contributions to transport), have shown mild increases of the energy confinement time for configurations of significantly reduced effective ripple [Geiger et al., 2015]. This points towards one of the obvious limitations of the effective ripple: it is only an appropriate figure of merit for neoclassical transport if the plasma species are in the asymptotic  $1/\nu$  regime. However, bulk particles are distributed close to a Maxwellian that typically spans across several transport regimes. Even in cases in which the collisionality is low and the neoclassical predictions of the radial energy flux agree with the experiment, the parameter dependence of the experimental energy flux does not follow the scaling expected for any specific neoclassical transport regime, see e.g. [Alonso et al., 2017b], because the flux is caused by a combination of transport regimes.

The reason for choosing the effective ripple as a figure of merit is that the  $1/\nu$  regime is the low-collisionality regime of stellarators in which the effect of the magnetic geometry on transport can be encapsulated in a straightforward manner in a single quantity that is independent of density, temperature and radial electric field. Furthermore, this quantity can be efficiently calculated by solving the bounce-averaged drift-kinetic equation, e.g. with the `NEO` code [Nemov et al., 1999]. None of this has been possible so far for other low-collisionality regimes for arbitrary stellarator geometry.

Moreover, for other regimes such as the  $\sqrt{\nu}$  and the superbanana-plateau regimes, the effect of the electric field (radial and tangential to the flux surface, the latter associated to the variation of the electrostatic potential on the flux surface,  $\varphi_1$ ) has to be considered [Calvo et al., 2017], and this quantity is determined by imposing ambipolarity of the neoclassical particle fluxes and quasineutrality, which in turn depend on the plasma profiles, and specifically on the gradients. In order to address this issue, self-consistent neoclassical transport simulations have been performed in the last few years: the neoclassical fluxes are calculated with the `DKES` code [Hirshman et al., 1986] and then the ambipolar and energy transport equations are solved (the latter with a prescribed energy source) [Turkin et al., 2011; Geiger et al., 2015]. Although we will see that `DKES` makes use of the so-called monoenergetic approximation, which reduces the problem from five dimensions to three, using `DKES` to self-consistently solve neoclassical energy transport is still computationally expensive at low collisionality. Moreover, `DKES` is inaccurate at sufficiently low collisionality: it uses an incompressible  $E \times B$  drift [Beidler et al., 2007] and does not include the tangential magnetic drift or the radial  $E \times B$  drift caused by the variation of the electrostatic potential within the flux surface (the latter makes the fluxes depend non-linearly on the

plasma gradients [Calvo et al., 2018b]). Some or all of these approximations are absent in more recent codes such as SFINCS [Landreman et al., 2014], EUTERPE [García-Regaña et al., 2013; García-Regaña et al., 2017] or FORTEC-3D [Satake et al., 2006], but at the expense of higher computational cost.

We have developed a new code, the KiNetic Orbit-averaging Solver for Optimizing Stellarators, KNOSOS, based on the analytical techniques developed in a series of papers [Calvo et al., 2013, 2014, 2015, 2017, 2018b]. It solves local drift-kinetic equations that will be summarized in the next section and that accurately describe neoclassical transport in the  $1/\nu$ ,  $\sqrt{\nu}$  and superbanana-plateau regimes. The equations include the effect of the magnetic drift tangential to flux surfaces and the radial  $E \times B$  drift due to the variation of the electrostatic potential within the flux surface; the radial electric field  $E_r$  and  $\varphi_1$  are obtained by imposing ambipolarity and quasineutrality, respectively. Local drift kinetic equations are valid for large-aspect-ratio stellarators or configurations close to omnigeneity (see the discussion before equation (3.27) in chapter 3). Unlike preliminary versions of KNOSOS [Velasco et al., 2018; Calvo et al., 2018b], this version does not require an explicit split of the magnetic field magnitude into omnigeneous and non-omnigeneous pieces. The goal of this code is to be, at the same time, accurate and fast, so that it allows one to perform comprehensive parameter scans and to provide input to other codes or suites of codes. Generally speaking, the goal is to improve our confidence in neoclassical predictions, in light of recent theory developments, and to be able to fully exploit these predictive capabilities. To facilitate this objective, the code is freely-available and open-source.

# Chapter 3

## Equations

\* In this chapter, we briefly present the equations solved by KNOSOS. Their derivation and further details can be found in previous work by [Calvo et al., 2017, 2018b]. We first define the coordinate system that we will use. The flux surfaces are labelled by the radial coordinate

$$\psi = |\Psi_t|, \quad (3.1)$$

where  $2\pi\Psi_t$  is the toroidal magnetic flux. The magnetic field lines on the surface are labelled by an angular coordinate

$$\alpha = \theta - \iota\zeta, \quad (3.2)$$

where  $\theta$  and  $\zeta$  are poloidal and toroidal Boozer angles, respectively, and  $\iota$  is the rotational transform. Finally,  $l$  is the arc-length along the magnetic field line. In these coordinates, the magnetic field  $\mathbf{B}$  can be written as

$$\mathbf{B} = \Psi'_t \nabla \psi \times \nabla \alpha, \quad (3.3)$$

where primes stand for derivatives with respect to  $\psi$ , and  $\Psi'_t = \pm 1$  depending on whether the magnetic field is parallel or antiparallel to the direction of the Boozer toroidal angle (i.e. depending on the sign of  $\mathbf{B} \cdot \nabla \zeta$ ).

As velocity coordinates, we choose the particle velocity

$$v = |\mathbf{v}|, \quad (3.4)$$

the pitch-angle coordinate

$$\lambda = \frac{1}{B} \frac{v_\perp^2}{v^2}, \quad (3.5)$$

and the sign of the parallel velocity

$$\sigma = \frac{v_\parallel}{|v_\parallel|} = \pm 1, \quad (3.6)$$

where, as usual,

$$\begin{aligned} v_\parallel &= \mathbf{v} \cdot \mathbf{b} = \mathbf{v} \cdot \frac{\mathbf{B}}{|\mathbf{B}|} = \mathbf{v} \cdot \frac{\mathbf{B}}{B}, \\ v_\perp &= \sqrt{v^2 - v_\parallel^2}. \end{aligned} \quad (3.7)$$

---

\*This chapter corresponds to section 2 and appendix A of [Velasco et al., 2019].

For each species  $b$  ( $i$  will denote bulk ions and  $e$  electrons), we need to calculate the deviation of the distribution function from a Maxwellian for trapped particles, that we denote by  $g_b(\psi, \alpha, l, v, \lambda, \sigma)$ . The Maxwellian distribution function reads

$$F_{M,b} = n_b \left( \frac{m_b}{2\pi T_b} \right)^{3/2} \exp \left( -\frac{m_b v^2}{2T_b} \right), \quad (3.8)$$

where  $n_b$  is the density,  $T_b$  the temperature and  $m_b$  the mass. Trapped particles are those for which  $v_{\parallel} = 0$  at some point along their trajectories. For them,  $1/B_{max} \leq \lambda \leq 1/B_{min}$ , where  $B_{max}$  and  $B_{min}$  are the maximum and minimum values of the magnetic field strength on the flux surface, respectively.

The equation for  $g_b(\psi, \alpha, v, \lambda)$  is

$$\int_{l_{b_1}}^{l_{b_2}} \frac{dl}{|v_{\parallel}|} \mathbf{v}_{D,b} \cdot \nabla \alpha \partial_{\alpha} g_b + \int_{l_{b_1}}^{l_{b_2}} \frac{dl}{|v_{\parallel}|} \mathbf{v}_{D,b} \cdot \nabla \psi \Upsilon_b F_{M,b} = \int_{l_{b_1}}^{l_{b_2}} \frac{dl}{|v_{\parallel}|} C_b^{\text{lin}}[g_b], \quad (3.9)$$

complemented with the condition at the boundary between passing and trapped,  $\lambda = 1/B_{max}$  ( $B_{max}$  is the maximum value of the magnetic field strength on the flux surface),

$$g_b(\lambda = 1/B_{max}) = 0, \quad (3.10)$$

and the condition

$$\int_0^{2\pi} g_b \, d\alpha = 0. \quad (3.11)$$

The coefficients of equation (3.9) are integrals over the arc-length between the bounce points  $l_{b_1}$  and  $l_{b_2}$ , i.e., between the points where the parallel velocity of the particle is zero (see a sketch in figure 3.1). On the right-hand side of equation (3.9),  $C_b^{\text{lin}}[g_b]$  is the linearized pitch-angle-scattering collision operator:

$$C_b^{\text{lin}}[g_b] = \frac{\nu_{\lambda,b} v_{\parallel}}{v^2 B} \partial_{\lambda} (v_{\parallel} \lambda \partial_{\lambda} g_b). \quad (3.12)$$

For the ions, since  $\sqrt{m_e/m_i} \ll 1$ , this single-species collision operator is correct, but electron-ion collisions need to be retained in the electron drift-kinetic equation. For both species, we follow the common practice (see e.g. [Beidler et al., 2011]) of using equation (3.12) with an effective collision frequency accounting for inter-species collisions, given by the sum<sup>†</sup>

$$\nu_{\lambda,b} = \sum_{b'} \nu_0^{b/b'} \left[ \text{erf} \left( \sqrt{m_{b'} v^2 / (2T_{b'})} \right) - \chi \left( \sqrt{m_{b'} v^2 / (2T_{b'})} \right) \right], \quad (3.13)$$

with

$$\nu_0^{b/b'} = \frac{8\pi n_{b'} Z_{b'}^2 Z_{b'}^{-2} e^4 \ln \Lambda^{b/b'}}{m_b^2 v^3}. \quad (3.14)$$

Here,  $\ln \Lambda^{b/b'}$  is the Coulomb logarithm,

$$\chi(x) = \frac{\text{erf}(x) - (2x/\sqrt{\pi}) \exp(-x^2)}{2x^2}, \quad (3.15)$$

---

<sup>†</sup>We note that  $\nu_{\lambda,b} = 2\nu_b$ , with the definition of  $\nu_b$  of page 3 of Beidler et al. [2011].

and

$$\operatorname{erf}(x) = \frac{2}{\sqrt{\pi}} \int_0^x \exp(-t^2) dt \quad (3.16)$$

is the error function.

On the left-hand-side of equation (3.9),

$$\Upsilon_b = \frac{\partial_\psi n_b}{n_b} + \frac{\partial_\psi T_b}{T_b} \left( \frac{m_b v^2}{2T_b} - \frac{3}{2} \right) + \frac{Z_b e \partial_\psi \varphi_0}{T_b} \quad (3.17)$$

is a combination of thermodynamical forces ( $Z_b$  the charge number, and the elementary charge is denoted by  $e$ ) and the drift velocity,

$$\mathbf{v}_{D,b} = \mathbf{v}_{M,b} + \mathbf{v}_E, \quad (3.18)$$

is the sum of the (low  $\beta$ ) magnetic drift and the  $E \times B$  drift:

$$\begin{aligned} \mathbf{v}_{M,b} &= \frac{m_b v^2}{Z_b e} \left( 1 - \frac{\lambda B}{2} \right) \frac{\mathbf{B} \times \nabla B}{B^3}, \\ \mathbf{v}_E &= -\frac{\nabla \varphi \times \mathbf{B}}{B^2}. \end{aligned} \quad (3.19)$$

Here,  $\varphi$  is the electrostatic potential, that can be split as

$$\varphi(\psi, \alpha, l) = \varphi_0(\psi) + \varphi_1(\psi, \alpha, l), \quad (3.20)$$

with

$$|\varphi_1| \ll |\varphi_0|, \quad (3.21)$$

which means that  $\varphi_0$  and  $\varphi_1$  will be the dominant contribution to the radial and tangential components of the electric field, respectively (and in turn to the tangential and radial components of the  $E \times B$  drift, respectively). The potentials  $\varphi_0$  and  $\varphi_1$  can be determined by solving two additional equations.

The component of the electrostatic potential that varies on the flux surface,  $\varphi_1$ , is obtained from the quasineutrality equation, which for a pure plasma (i.e., composed of electrons and one ion species) reads

$$\left( \frac{Z_i}{T_i} + \frac{1}{T_e} \right) \varphi_1 = \frac{2\pi}{en_e} \sum_b Z_b \int_0^\infty dv \int_{B_{\max}^{-1}}^{B^{-1}} d\lambda \frac{v^3 B}{|v_\parallel|} g_b. \quad (3.22)$$

The sum is done over kinetic species. Here, we have used that, in terms of our coordinates, velocity space integrals are of the form

$$\int d^3v (...) = \pi \sum_\sigma \int_0^\infty dv v^2 \int_0^{B^{-1}} d\lambda \frac{B}{\sqrt{1 - \lambda B}} (...), \quad (3.23)$$

that  $g_b$  is even in  $\sigma$  and that  $g_b = 0$  for  $\lambda < B_{\max}^{-1}$ . We note that, since  $\varphi_1$  and  $g_b$  appear in equations (3.9) and (3.22), both equations need to be solved consistently.

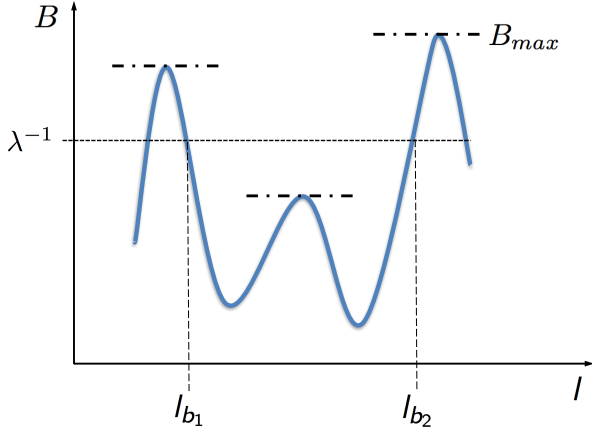


Figure 3.1: Sketch of a particle trajectory at fixed  $\alpha$ . divergences are indicated with dot-dashed horizontal lines.

The radial electric field is given by the radial derivative of the piece of the electrostatic potential that is constant on the flux surface,

$$E_r = -\partial_r \varphi_0 = -\frac{\partial \psi}{\partial r} \partial_\psi \varphi_0, \quad (3.24)$$

where  $r = a\sqrt{\psi/\psi_{LCFS}}$ ,  $\psi_{LCFS}$  being the flux-label at the last closed flux surface and  $a$  the minor radius of the device. The radial electric field is set by the ambipolarity of the neoclassical radial particle fluxes,

$$\sum_b Z_b \Gamma_b (\partial_\psi \varphi_0) = 0. \quad (3.25)$$

In our variables,

$$\Gamma_b \equiv \langle \mathbf{\Gamma}_b \cdot \nabla r \rangle = 2 \frac{\partial r}{\partial \psi} \left\langle \int_0^\infty dv \int_{B_{\max}^{-1}}^{B^{-1}} d\lambda \frac{v^2 B}{\sqrt{1-\lambda B}} g_b \mathbf{v}_{D,b} \cdot \nabla \psi \right\rangle,$$

where  $\langle \dots \rangle$  denotes flux-surface average. Finally, the radial energy flux is given by

$$Q_b \equiv \langle \mathbf{Q}_b \cdot \nabla r \rangle = 2 \frac{\partial r}{\partial \psi} \left\langle \int_0^\infty dv \int_{B_{\max}^{-1}}^{B^{-1}} d\lambda \frac{v^3 B}{\sqrt{1-\lambda B}} g_b \frac{m_b v^2}{2} \mathbf{v}_{D,b} \cdot \nabla \psi \right\rangle. \quad (3.26)$$

**KNOSOS** solves equations (3.9) and (3.22), together with equation (3.25). These equations have been rigorously derived in [Calvo et al., 2018b] under the hypotheses of low collisionality, large aspect ratio and closeness to omnigeneity (we note that large aspect-ratio is a common characteristic of real stellarators [Beidler et al., 2011] while, as noted in the introduction, closeness to omnigeneity is a property sought in present and future devices). At low collisionalities, the motion of particles along the magnetic field is much faster than

collisions, and the distribution function does not depend on the arc length  $l$ . Closeness to omnigeneity makes neoclassical transport describable by a radially-local equation for the deviation of the distribution function of trapped particles from a Maxwellian. In particular, it guarantees that the bounce-averaged radial drift is small enough so that

$$\left| \int_{l_{b_1}}^{l_{b_2}} \frac{dl}{|v_{\parallel}|} \mathbf{v}_{D,b} \cdot \nabla \psi \partial_{\psi} g_b \right| \ll \left| \int_{l_{b_1}}^{l_{b_2}} \frac{dl}{|v_{\parallel}|} \mathbf{v}_{D,b} \cdot \nabla \alpha \partial_{\alpha} g_b \right| \quad (3.27)$$

even in situations of small  $E \times B$  drift. Hence, for stellarators close to omnigenity, terms proportional to  $\partial_{\psi} g$  do not appear in equation (3.9). Finally, the large-aspect ratio approximation allows us to use the pitch-angle collision operator, equation (3.12).

Let us finally discuss the neoclassical regimes that equations (3.9) and (3.22) can describe. The second term on the left-hand side of equation (3.9) includes the radial magnetic and  $E \times B$  drifts caused by the inhomogeneity of the magnetic field strength and of the electrostatic potential on the flux surface, respectively. This means that equation (3.9) can model the  $1/\nu$  regime and the transport caused by  $\varphi_1$ . The first term of the left-hand side includes the precession tangential to the flux surface caused by the radial variation of the electrostatic potential (i.e. the radial electric field  $E_r$ ) and of the magnetic field strength. This implies that we can model the  $\sqrt{\nu}$  and superbanana-plateau regimes. As discussed previously, radially global effects are not accounted for.

## Chapter 4

# Solution of the equations

\* In this chapter, we provide an overview of how equations (3.9) and (3.22) are solved. We first give an explicit expression for equation (3.9) in §4.1 and we discuss how to calculate its bounce-averaged coefficients in §4.2. We then devote §4.3 to build the grid in which we will evaluate the distribution function, and §4.4 to discuss the discretization of the equation. Finally, the solution of quasineutrality, equation (3.22), is addressed in §4.5.

### 4.1 Final expression of the drift-kinetic equation

Using the expressions of the pitch-angle scattering collision operator described in equation (3.12) and of the magnetic and  $E \times B$  drifts in *right handed* Boozer coordinates, equation (3.9) can be written in terms of a few bounce integrals:

$$\begin{aligned} \left( I_{v_{M,\alpha}}(\alpha, \lambda) + \frac{1}{v_{d,b}} I_{v_{E,\alpha}}(\alpha, \lambda) \right) \partial_\alpha g_b &+ \left( I_{v_{M,\psi}}(\alpha, \lambda) + \frac{1}{v_{d,b}} I_{v_{E,\psi}}(\alpha, \lambda) \right) F_{M,b} \Upsilon_b \\ &= \frac{\nu_{\lambda,b}}{v_{d,b}} \partial_\lambda [I_\nu(\alpha, \lambda) \partial_\lambda g_b] , \end{aligned} \quad (4.1)$$

---

\*This chapter corresponds to section 3 and appendices B and C of [Velasco et al., 2019].

with

$$\begin{aligned}
v_{d,b} &\equiv \frac{m_b v^2}{Z_b e}, \\
I_{v_{E,\alpha}} &= \Psi'_t \partial_\psi \varphi_0 \int_{l_{b_1}}^{l_{b_2}} \frac{dl}{\sqrt{1 - \lambda B}}, \\
I_{v_{M,\alpha}} &= \int_{l_{b_1}}^{l_{b_2}} \frac{dl}{\sqrt{1 - \lambda B}} \left(1 - \frac{\lambda B}{2}\right) \left[ \Psi'_t \frac{\partial_\psi B}{B} + \frac{B_\zeta \partial_\theta B - B_\theta \partial_\zeta B}{B|B_\zeta + \iota B_\theta|} \zeta \partial_\psi \iota \right], \\
I_{v_{E,\psi}} &= \int_{l_{b_1}}^{l_{b_2}} \frac{dl}{\sqrt{1 - \lambda B}} \frac{B_\theta \partial_\zeta \varphi_1 - B_\zeta \partial_\theta \varphi_1}{|B_\zeta + \iota B_\theta|}, \\
I_{v_{M,\psi}} &= \int_{l_{b_1}}^{l_{b_2}} \frac{dl}{\sqrt{1 - \lambda B}} \left(1 - \frac{\lambda B}{2}\right) \frac{B_\theta \partial_\zeta B - B_\zeta \partial_\theta B}{B|B_\zeta + \iota B_\theta|}, \\
I_\nu &= \int_{l_{b_1}}^{l_{b_2}} dl \frac{\lambda \sqrt{1 - \lambda B}}{B}.
\end{aligned} \tag{4.2}$$

where  $B_\psi$ ,  $B_\theta$  and  $B_\zeta$  are the covariant components of  $\mathbf{B}$ , and  $B_\psi = 0$  in the low- $\beta$  approximation. We note that only  $v_{d,b}$ ,  $\nu_{\lambda,b}$ ,  $F_{M,b}$  and  $\Upsilon_b$  depend on the species: the bounce-integrals are only determined by the magnetic configuration and the electrostatic potential. The magnetic shear appears explicitly in  $I_{v_{M,\alpha}}$ .

Equation (4.1) is a differential equation in two variables only,  $\alpha$  and  $\lambda$ , which is the origin of the fast performance of KNOSOS that will be demonstrated in chapter 11. The radial coordinate  $\psi$  is a parameter, since we are solving radially local equations;  $v$  is a parameter as well, since  $\varphi_1 \ll \varphi_0$ ; and finally  $l$  has disappeared since the coefficients are bounce-averages of certain quantities. The calculation of these coefficients is described in §4.2.

## 4.2 Calculation of the coefficients of the drift-kinetic equation

The integrals in  $l$  are done using an extended midpoint rule [see e.g. Press et al., 1996, subroutine `midpnt`]. This open formula is appropriate for integrals that are improper in the sense that they have an integrable singularity at the integration limits. This is our case, since by definition  $\lambda B(l_{b_1}) = \lambda B(l_{b_2}) = 1$ . The number of points that we use is not pre-defined: starting from being one, it is tripled until the integral converges.

Let us now note that integrals such as those of equations (4.2) may be difficult to converge if the numerator does not go to zero in the integration limits, or it does, but slower than the denominator. This may happen, first, if  $\lambda$  is such that  $l_{b_1}$  or  $l_{b_2}$  are close to a point  $l_T$  where  $B(l)$  has a local maximum  $B(l_T)$  for fixed  $\alpha$ ; second, if the interval  $(l_{b_1}, l_{b_2})$  contains a point  $l_B$  where  $B(l)$  has a local maximum and  $\lambda$  is close to  $\lambda_B \equiv 1/B(l_B)$ . In such cases,  $I(\lambda)$  may become very large; if the inverse of  $\lambda$  is equal to the corresponding maximum of  $B$ , the integral diverges logarithmically. We can physically identify these situations in the example of figure 3.1: divergences happen at *bifurcations*, where orbits go from being trapped in a particular region in  $l$  to be trapped, for smaller  $\lambda$ , in a wider region (the boundary between passing and trapped particles is a particular case of this).

One can ease the convergence, and thus make the calculation faster, by removing the divergence and solving it analytically as explained in Appendix C of [Calvo et al., 2017]. This is described more in detail in the next subsection. Another subsection discusses how the fact that field lines are straight in magnetic coordinates is used to accelerate the evaluation of the magnetic field strength at each point  $(\alpha, l)$  without loss of accuracy.

#### 4.2.1 Analytical calculation of the divergences of some bounce-integrals

In this subsection, we discuss how integrals such as those in equations (4.2),

$$I(\lambda) = \int_{l_{b_1}}^{l_{b_2}} dl \frac{f(\lambda, l)}{\sqrt{1 - \lambda B(l)}}, \quad (4.3)$$

can be computed efficiently by removing the component that diverges close to bifurcations and solving it analytically. Since integration is done at fixed  $\alpha$ , we ease the notation by not making it explicit that  $B$ ,  $f$ , and  $I$  generally depend on the angular coordinate.

We first expand the magnetic field around the bounce point:

$$B(l) = B(l_{b_1}) + \partial_l B|_{l_{b_1}}(l - l_{b_1}) + \frac{1}{2}\partial_l^2 B|_{l_{b_1}}(l - l_{b_1})^2. \quad (4.4)$$

Close to the bounce point, we have

$$\frac{f(l)}{\sqrt{1 - \lambda B(l)}} \approx \frac{f(l_{b_1})}{\sqrt{-\lambda(l - l_{b_1})[\partial_l B|_{l_{b_1}} + \frac{1}{2}\partial_l^2 B|_{l_{b_1}}(l - l_{b_1})]}} \quad (4.5)$$

since  $\lambda B(l_{b_1}) = 1$ . We can proceed exactly in the same way close to  $l_{b_2}$ , and similarly close to  $\lambda_B$ : there,  $\lambda B(l_B) < 1$  and the first derivative  $\partial_l B|_{l_B}$  is zero, and we have

$$\frac{f(l)}{\sqrt{1 - \lambda B(l)}} \approx \frac{f(l_B)}{\sqrt{-(\lambda - \lambda_B)B(l_B) - \lambda_B \frac{1}{2}\partial_l^2 B|_{l_B}(l - l_B)^2}}. \quad (4.6)$$

We can then split the integral in three contributions:

$$I = I_0 + I_1 + I_2 + I_B, \quad (4.7)$$

with

$$\begin{aligned} I_0 &= \int_{l_{b_1}}^{l_{b_2}} dl \left( \frac{f(l)}{\sqrt{1 - \lambda B(l)}} \right. \\ &- \frac{f(l_{b_1})}{\sqrt{-\lambda(l - l_{b_1})[\partial_l B|_{l_{b_1}} + \frac{1}{2}\partial_l^2 B|_{l_{b_1}}(l - l_{b_1})]}}} \\ &- \frac{f(l_{b_2})}{\sqrt{-\lambda(l - l_{b_2})[\partial_l B|_{l_{b_2}} + \frac{1}{2}\partial_l^2 B|_{l_{b_2}}(l - l_{b_2})]}} \\ &\left. - \frac{f(l_B)}{\sqrt{-(\lambda - \lambda_B)B(l_B) - \lambda_B \frac{1}{2}\partial_l^2 B|_{l_B}(l - l_B)^2}} \right), \end{aligned} \quad (4.8)$$

whose integrand does not diverge anywhere and

$$\begin{aligned} I_1 &= \int_{l_{b_1}}^{l_{b_2}} dl \frac{f(l)}{\sqrt{-\lambda(l-l_{b_1})[\partial_l B|_{l_{b_1}} + \frac{1}{2}\partial_l^2 B|_{l_{b_1}}(l-l_{b_1})]}}, \\ I_2 &= \int_{l_{b_1}}^{l_{b_2}} dl \frac{f(l)}{\sqrt{-\lambda(l-l_{b_2})[\partial_l B|_{l_{b_2}} + \frac{1}{2}\partial_l^2 B|_{l_{b_2}}(l-l_{b_2})]}}, \\ I_B &= \int_{l_{b_1}}^{l_{b_2}} dl \frac{f(l_B)}{\sqrt{-(\lambda - \lambda_B)B(l_B) - \lambda_B \frac{1}{2}\partial_l^2 B|_{l_B}(l-l_B)^2}}, \end{aligned} \quad (4.9)$$

which can be solved analytically. The integral close to the bottom is

$$\begin{aligned} I_B &= \sqrt{\frac{-2}{\lambda_B \partial_l^2 B|_{l_B}}} \left[ \ln \left( x + \sqrt{x^2 + \frac{2(\lambda - \lambda_B)B(l_B)}{\lambda_B \partial_l^2 B|_{l_B}}} \right) \right]_0^{l_B - l_{b_1}} \\ &\quad + \sqrt{\frac{-2}{\lambda_B \partial_l^2 B|_{l_B}}} \left[ \ln \left( x + \sqrt{x^2 + \frac{2(\lambda - \lambda_B)B(l_B)}{\lambda_B \partial_l^2 B|_{l_B}}} \right) \right]_0^{l_{b_2} - l_B}. \end{aligned} \quad (4.10)$$

For the other two integrals, if  $\partial_l^2 B|_{l_{b_1}} < 0$  and  $\partial_l^2 B|_{l_{b_2}} < 0$ , the solution is

$$\begin{aligned} I_1 &= \sqrt{\frac{-2}{\lambda \partial_l^2 B|_{l_{b_1}}}} \times \\ &\quad \left[ \ln \left( 2\lambda \sqrt{\frac{\partial_l^2 B|_{l_{b_1}}}{-2}} \sqrt{-\partial_l B|_{l_{b_1}} x - \frac{1}{2}\partial_l^2 B|_{l_{b_1}} x^2} - \lambda \partial_l^2 B|_{l_{b_1}} x - \lambda \partial_l B|_{l_{b_1}} \right) \right]_0^{l_{b_2} - l_{b_1}}, \\ I_2 &= \sqrt{\frac{-2}{\lambda \partial_l^2 B|_{l_{b_2}}}} \times \\ &\quad \left[ \ln \left( 2\lambda \sqrt{\frac{\partial_l^2 B|_{l_{b_2}}}{-2}} \sqrt{-\partial_l B|_{l_{b_2}} x - \frac{1}{2}\partial_l^2 B|_{l_{b_2}} x^2} - \lambda \partial_l^2 B|_{l_{b_2}} x - \lambda \partial_l B|_{l_{b_2}} \right) \right]_{l_{b_1} - l_{b_2}}^0. \end{aligned} \quad (4.11)$$

These expressions are useful (in the sense of removing large analytical contributions to  $I$ ) close enough to a bifurcation, where they can significantly accelerate the convergence of equations (4.2), but they are in principle valid for any  $\lambda$  (far from bifurcations, when  $\partial_l^2 B|_{l_{b_1}}$  is positive, the expression within the square-root may become negative and cannot be used).

#### 4.2.2 Evaluation of the magnetic field strength along a field line

The fact that field lines are straight in magnetic coordinates can also be used to speed up the calculation of the coefficients of the drift-kinetic equation. We describe how in this subsection.

The bounce-integrals are done, using the algorithm mentioned in §4.2, by following field lines using a fixed step in the Boozer angles given by  $\Delta\zeta$  and  $\Delta\theta = \iota\Delta\zeta$ . After each step, the magnetic field can be calculated without loss of accuracy from its Fourier components

$$\begin{aligned}
 B(\theta, \zeta) &= \sum_{m,n} B_{m,n}^{(c)} (\cos[m\theta + nN\zeta]) \\
 &\quad + \sum_{m,n} B_{m,n}^{(s)} (\cos[m\theta + nN\zeta]), \\
 B(\theta + \Delta\theta, \zeta + \Delta\zeta) &= \sum_{m,n} B_{m,n}^{(c)} \cos[m(\theta + \Delta\theta) + nN(\zeta + \Delta\zeta)] \\
 &\quad + \sum_{m,n} B_{m,n}^{(s)} \sin[m(\theta + \Delta\theta) + nN(\zeta + \Delta\zeta)], \\
 B(\theta + 2\Delta\theta, \zeta + 2\Delta\zeta) &= \sum_{m,n} B_{m,n}^{(c)} \cos[m(\theta + 2\Delta\theta) + nN(\zeta + 2\Delta\zeta)] \\
 &\quad + \sum_{m,n} B_{m,n}^{(s)} \sin[m(\theta + 2\Delta\theta) + nN(\zeta + 2\Delta\zeta)], \\
 &\dots
 \end{aligned} \tag{4.12}$$

Instead of calculating the cosines at every angular position, we can precalculate a few sines and cosines,  $\cos(m\theta + nN\zeta)$ ,  $\sin(m\theta + nN\zeta)$ ,  $\cos(m\Delta\theta + nN\Delta\zeta)$  and  $\sin(m\Delta\theta + nN\Delta\zeta)$ , and use well-known trigonometric identities to iterate:

$$\begin{aligned}
 \cos[m(\theta + \Delta\theta) + nN(\zeta + \Delta\zeta)] &= \cos(m\theta + nN\zeta) \cos(m\Delta\theta + nN\Delta\zeta) \\
 &\quad - \sin(m\theta + nN\zeta) \sin(m\Delta\theta + nN\Delta\zeta), \\
 \sin[m(\theta + \Delta\theta) + nN(\zeta + \Delta\zeta)] &= \cos(m\theta + nN\zeta) \sin(m\Delta\theta + nN\Delta\zeta) \\
 &\quad + \sin(m\theta + nN\zeta) \cos(m\Delta\theta + nN\Delta\zeta),
 \end{aligned} \tag{4.13}$$

and

$$\begin{aligned}
 \cos[m(\theta + 2\Delta\theta) + nN(\zeta + 2\Delta\zeta)] &= \cos[m(\theta + \Delta\theta) + nN(\zeta + \Delta\zeta)] \cos(m\Delta\theta + nN\Delta\zeta) \\
 &\quad - \sin[m(\theta + \Delta\theta) + nN(\zeta + \Delta\zeta)] \sin(m\Delta\theta + nN\Delta\zeta), \\
 \sin[m(\theta + 2\Delta\theta) + nN(\zeta + 2\Delta\zeta)] &= \cos[m(\theta + \Delta\theta) + nN(\zeta + \Delta\zeta)] \sin(m\Delta\theta + nN\Delta\zeta) \\
 &\quad + \sin[m(\theta + \Delta\theta) + nN(\zeta + \Delta\zeta)] \cos(m\Delta\theta + nN\Delta\zeta)
 \end{aligned} \tag{4.14}$$

and so on.

### 4.3 Spatial and velocity grid

In §4.2 we have seen how the integrals of equations (4.2) are calculated. These integrals will be evaluated at the points  $(\alpha, \lambda)$  in which we want to determine the distribution function  $g_b$ . The selection of these points constitute the subject of this section.

Let us start with the spatial grid. We have seen that  $\psi$  is a parameter, and  $l$  does not appear in the bounce-averaged drift-kinetic equation, which leaves us with the field line

label  $\alpha$ . There are, however, two complications: first, at a given  $\alpha$  and  $\lambda$ , several wells may exist (in other words, several pairs of  $l_{b_1}$  and  $l_{b_2}$ ), which means that we need to use an integer label  $w$  for them (as we will discuss more in detail in the following section). Second, even if  $g_b$  does not depend on  $l$ , its integrals over velocities (needed e.g. to compute  $\varphi_1$ , see equation (3.22)) do, so we must define a two-dimensional angular grid. As a general rule, when doing so, we try to minimize the number of points at which  $g_b$  needs to be solved, in order to save computing resources. With this in mind, we make use of periodicity and align the grid points with the field lines. The grid points are also aligned with  $\zeta = 0$ .

We use figure 4.1 (top), which shows one example of stellarator flux surface (the W7-X case discussed in §11.1) to describe how the angular grid is built. We follow several field lines until they have completed a full poloidal turn. The distance between two consecutive field lines  $\Delta\alpha$  is taken to be an integer fraction (one sixth, in the plot) of  $2\pi\ell/N$ , where  $N$  is the number of toroidal periods. This is how the green points are located, with uniform spacing in the toroidal angle. Along the field lines, several maxima of the magnetic field are found, plotted with magenta circles. It is observed that we are dealing with a relatively optimized configuration, in the sense that most trapped particles are so in a major well that coincides with one field period (black continuous arrow). In other words, their bounce points  $l_{b_1}$  and  $l_{b_2}$  are two consecutive magenta points, separated toroidally by a characteristic angular distance  $\sim 2\pi/N$  (smaller for large values of  $\lambda$ , close to the bottom of the magnetic well). In the example, several ripple wells are found (grey arrows). For small enough values of  $\lambda$ , trajectories trapped in more than one field-period exist: in this example, particles may move between  $\zeta = 0$  and  $\zeta = 6\frac{2\pi}{N}$  (black dashed arrow); trajectories with smaller  $\lambda$  (that is, trapped in more than 6 toroidal periods) are ignored in this case; this procedure effectively sets the boundary between passing and trapped particles (following field lines until they have completed more than one poloidal turn would allow us to describe trajectories with smaller  $\lambda$ , but this is not necessary in the light of the results of chapter 11).

Periodicity allows us to project all these grid points onto the first period. The result is a bidimensional grid in  $\alpha$  and  $l$ , with  $\mathcal{N}_\alpha$  and  $\mathcal{N}_l$  points in each direction.  $\mathcal{N}_\alpha$  is the integer quantity such that  $\mathcal{N}_\alpha < \frac{2\pi}{\Delta\alpha} \leq \mathcal{N}_\alpha + 1$ . The  $\mathcal{N}_l$  points along the field line are distributed uniformly in the toroidal angle along a toroidal period, and  $\mathcal{N}_l$  is the largest power of 2 that is smaller than or equal to  $\mathcal{N}_\alpha$ . This will be useful for a fast computation of the Fourier transform, needed when solving quasineutrality. Toroidal periodicity is also enforced at the corners of the grid: for instance, in figure 4.1 bottom, point  $\alpha = \alpha_{\mathcal{N}_\alpha-4}$ ,  $\zeta = 0$ , is not contained in the wells marked in magenta. Using periodicity, the value of the distribution function at this point will be taken to be equal to the value at  $\alpha = \alpha_1$  and  $\zeta = 2\pi/N$ . The number of points where this has to be done can be minimized by putting one of the corners of the grid close to the global maximum of  $B$  on the flux-surface. For each of the nodes of this grid (and for each of the possible values of  $\lambda$ ) the points along the trajectory and the bounce points of particles trapped in one or several field-periods are now clearly identified, and the integrals of equation (4.2) can be evaluated.

Let us turn our attention to the velocity grid, where we are using  $\lambda$  and  $v$  as coordinates. Since we have seen in chapter 3 that only trapped particles need to be calculated, an obvious choice for the former is a uniform grid<sup>†</sup>, with  $\mathcal{N}_\lambda + 1$  values between  $\lambda_1 \equiv 1/B_{max}$  and

---

<sup>†</sup>When the particles are in the  $1/\nu$  regime, special attention should be paid to bifurcations, where  $g_b$  has discontinuous first  $\lambda$ -derivatives [Nemov et al., 1999; Calvo et al., 2014], and a non-uniform grid, adapted

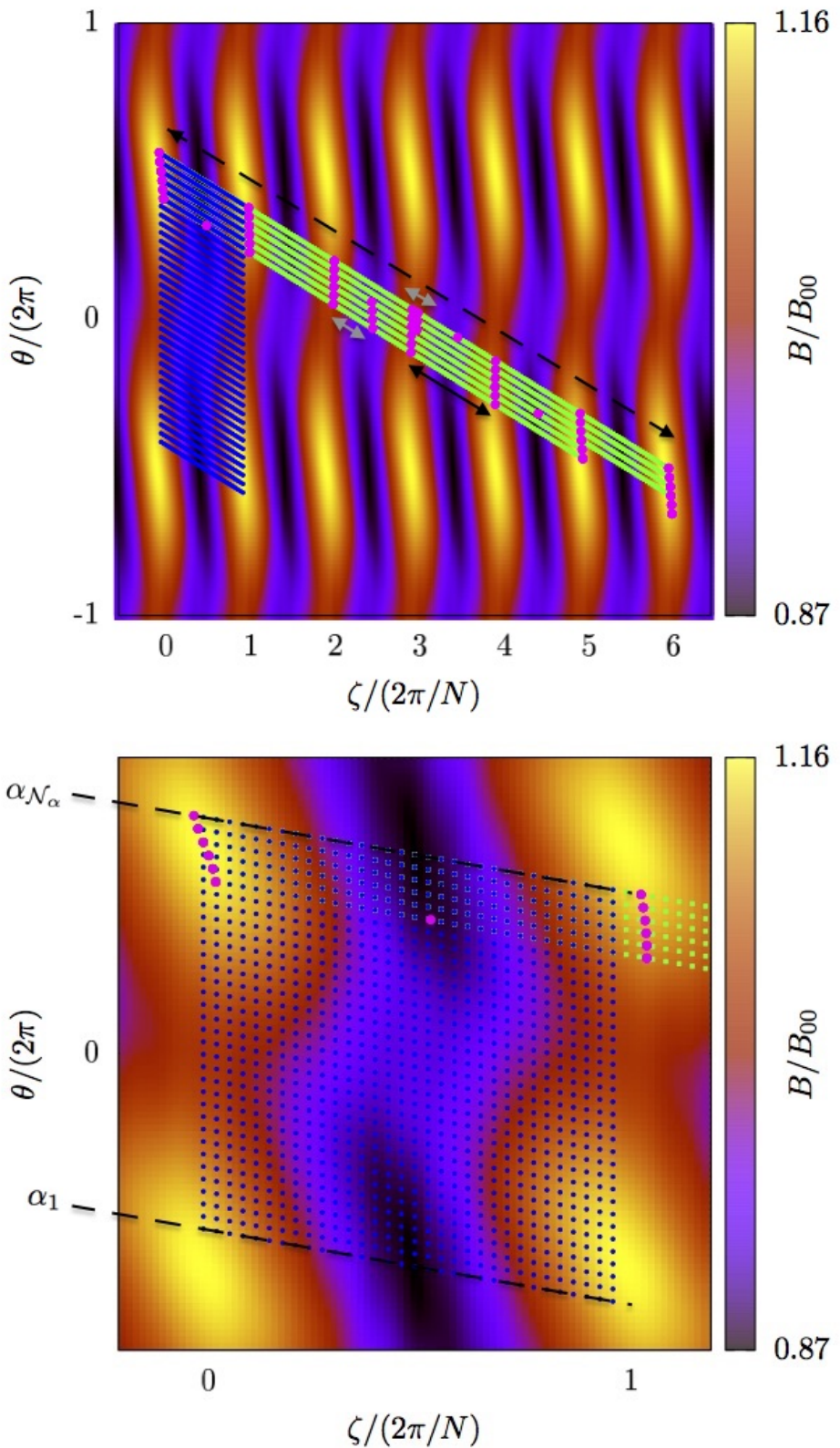


Figure 4.1: Construction of the angular grid (see text) for a flux-surface of W7-X (top); zoom (bottom).

$\lambda_{\mathcal{N}_\lambda+1} \equiv 1/B_{min}$ . The distribution function will not be evaluated at  $\lambda_{\mathcal{N}_\lambda+1}$ , which will be *ghost* points employed for imposing the boundary conditions at the bottom of the well. When integrating in  $\lambda$ , we will use the extended trapezoidal rule [Press et al., 1996].

Finally,  $v$  is a parameter in our calculations: equation (4.1) will be solved for several values  $v_i$  of the velocity and the solution will be numerically integrated in  $v$ . Since the integrand of equations (3.23) contains an exponential coming from the Maxwellian distribution, we will use Gauss-Laguerre of order 64 [Press et al., 1996]:

$$\int_0^\infty d(v^2/v_{th,b}^2) f(v^2/v_{th,b}^2) \exp(-v^2/v_{th,b}^2) \approx \sum_{i=1}^n \omega_i f(v_i^2/v_{th,b}^2), \quad (4.15)$$

being  $v_{th,b}$  the thermal velocity of species  $b$ , and  $\omega_i$  a set of tabulated real numbers. This procedure requires solving the monoenergetic drift-kinetic equation for  $n = 64$  values of  $v/v_{th,b}$ , typically from  $\sim 10^{-2}$  to  $\sim 10^2$ . However, the contribution of the largest  $v_i$  to the integral can be usually neglected, and this allows for an important reduction of computing time. Let us finally note that this is a standard and well-tested choice in neoclassics and gyrokinetics [e.g. Velasco et al., 2011; Barnes et al., 2019], although other velocity-space discretization methods have been proposed in recent years [Landreman and Ernst, 2013] that could be easily implemented in KNOSOS.

## 4.4 Discretization of the drift-kinetic equation

In §4.3 we have built a grid in variables  $\alpha$  and  $\lambda$ . Three integers can be used to label any point  $(\alpha_i, \lambda_j, w)$  of this grid:  $i$  runs from 1 to  $\mathcal{N}_\alpha$ ,  $j$  from 1 to  $\mathcal{N}_\lambda$  and  $w = I, II, \dots$  is an integer that labels wells for a given  $\alpha$  and  $\lambda$ . At a given point, we define  $g_{i,j,w} \equiv g_b(\alpha_i, \lambda_j, w)$ ,  $I_{\nu,i,j,w} \equiv I_\nu(\alpha_i, \lambda_j, w)$  and so on (in order to ease the notation,  $g_{i,j,w}$  does not contain a species index). The final step in the discretization of the drift-kinetic equation is how we approximate the derivatives of  $g_b$  of equation (4.1) at each point of this grid.

Let us start with the collision operator, which divided by  $\frac{\nu_{\lambda,b}}{v_{d,b}}$  reads

$$\partial_\lambda [I_\nu \partial_\lambda g_b], \quad (4.16)$$

and can be expanded into two terms

$$[I_\nu \partial_\lambda^2 + (\partial_\lambda I_\nu) \partial_\lambda] g_b. \quad (4.17)$$

We represent the  $\lambda$  grid at fixed  $\alpha$  in figure 4.2. Here,  $\lambda_1$  is the boundary between passing and trapped particles. In this example, only one complete well is plotted at  $\lambda_2$ , labelled  $I$ . If one moves to larger  $\lambda$ , a bifurcation appears in the vicinity of  $\lambda_{j_0}$ , with two wells labelled  $I$  and  $II$ . At a larger value of  $\lambda$ , there are the bottoms of the wells, where the wells have their minimum magnetic field (different in  $I$  than in  $II$ ) and beyond which no orbits are allowed.

---

to the structure of maxima and minima at fixed  $\alpha$ , is a more efficient choice [Kernbichler et al., 2016]. The same applies to very low collisionalities, when the contribution to the flux is concentrated on very thin  $\lambda$  layers. For the wide parameter range that will be studied with KNOSOS, the uniform grid is considered appropriate.

At a generic point, we make use of equation (4.17) and then employ central finite differences with second-order accuracy

$$\begin{aligned} [I_\nu \partial_\lambda^2 + (\partial_\lambda I_\nu) \partial_\lambda] g_b|_{i,j,w} &= I_{\nu,i,j,w} \frac{g_{i,j+1,w} + g_{i,j-1,w} - 2g_{i,j,w}}{(\Delta\lambda)^2} \\ &\quad + \partial_\lambda I_\nu|_{i,j,w} \frac{g_{i,j+1,w} - g_{i,j-1,w}}{2\Delta\lambda}, \end{aligned} \quad (4.18)$$

with  $\Delta\lambda = \lambda_{j+1} - \lambda_j$ . Differentiation is done at fixed  $\alpha$  and well-label  $w$ . At a bifurcation, such as the one near  $\lambda_{j_0}$  in figure 4.2, we use finite differences with second-order accuracy directly over equation (4.16) and summing over wells,

$$\begin{aligned} \partial_\lambda [I_\nu \partial_\lambda g_b]|_{i,j_0,I} &= \frac{[I_\nu \partial_\lambda g_b]|_{i,j_0+1,I} + [I_\nu \partial_\lambda g_b]|_{i,j_0+1,II} - [I_\nu \partial_\lambda g_b]|_{i,j_0-1,I}}{2\Delta\lambda} \\ &= I_{\nu,i,j_0+1,I} \frac{g_{i,j_0+2,I} - g_{i,j_0,I}}{4(\Delta\lambda)^2} \\ &\quad + I_{\nu,i,j_0+1,II} \frac{g_{i,j_0+2,II} - g_{i,j_0,I}}{4(\Delta\lambda)^2} \\ &\quad - I_{\nu,i,j_0-1,I} \frac{g_{i,j_0,I} - g_{i,j_0-2,I}}{4(\Delta\lambda)^2}. \end{aligned} \quad (4.19)$$

This discretization is designed to obtain the expected relation between different values of  $\partial_\lambda g$  at the bifurcation for the  $1/\nu$  regime [Nemov et al., 1999; Calvo et al., 2014]. Finally, we have two kinds of boundary conditions: one at the boundary between passing and trapped particles, corresponding to equation (3.10),

$$g_{i,1,w} = 0, \quad (4.20)$$

and one at the bottom, corresponding to regularity [Calvo et al., 2013],

$$\partial_\lambda [I_\nu \partial_\lambda g_b]|_{i,\mathcal{N}_\lambda,w} = -I_{\nu,i,\mathcal{N}_\lambda-1,w} \frac{g_{i,\mathcal{N}_\lambda,w} - g_{i,\mathcal{N}_\lambda-2,w}}{4(\Delta\lambda)^2}. \quad (4.21)$$

Here we have employed a ghost point  $\lambda_{\mathcal{N}_\lambda+1}$  at exactly the bottom of the well, where  $I_{\nu,i,\mathcal{N}_\lambda+1,w} = 0$ . One precision must be made: while in omnigenous magnetic fields the values of the maxima and minima of  $B$  are the same when moving in  $\alpha$ , and equation (4.21) can be used as such for all  $\alpha$ , this ceases to be true in a generic stellarator. For instance, the distance from  $\lambda_{\mathcal{N}_\lambda}$  to the local bottom will be exactly  $\Delta\lambda$  for one field line and smaller elsewhere (it may even happen that the contour condition must not be applied to  $\partial_\lambda [I_\nu \partial_\lambda g_b]|_{i,\mathcal{N}_\lambda,w}$ , but to  $\partial_\lambda [I_\nu \partial_\lambda g_b]|_{i,j,w}$  with a smaller  $j$ ). This requires introducing straightforward corrections to equations (4.18), (4.19), (4.20) and (4.21).

Let us now turn our attention to the terms with the first derivative in  $\alpha$  in equation (4.1), which we multiply by  $v_{d,b}$ :

$$(v_{d,b} I_{v_{M,\alpha}} + I_{v_{E,\alpha}}) \partial_\alpha g_b. \quad (4.22)$$

We represent the  $\alpha$  grid at fixed  $\lambda$  in figure 4.3 (top). In this example, there is only one well at  $\alpha_1$ , labelled  $I$ . If one moves from smaller to larger  $\alpha$ , a bifurcation appears in the vicinity of  $\alpha_{i_0}$ , with two wells labelled  $I$  and  $II$ . At a larger value of  $\alpha$ , the wells merge into a single region labelled again  $I$ . The last point of the grid,  $\alpha_{\mathcal{N}_\alpha}$ , is close to  $\alpha_1 + 2\pi$ .

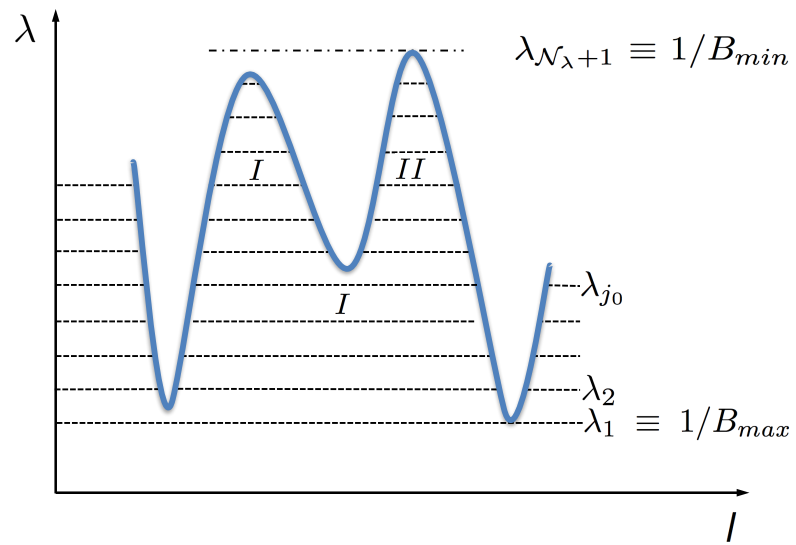


Figure 4.2: Sketch of grid in  $\lambda$  space at fixed  $\alpha$ . The collision operator is discretized as in equation (4.18) except at the top ( $\lambda_1$ ) or bottom ( $\lambda_{N_\lambda}$ ) of the well and at bifurcations (e.g.  $\lambda_{j_0}$ ); there, equations (4.21), (4.20) and (4.19), respectively are used instead.

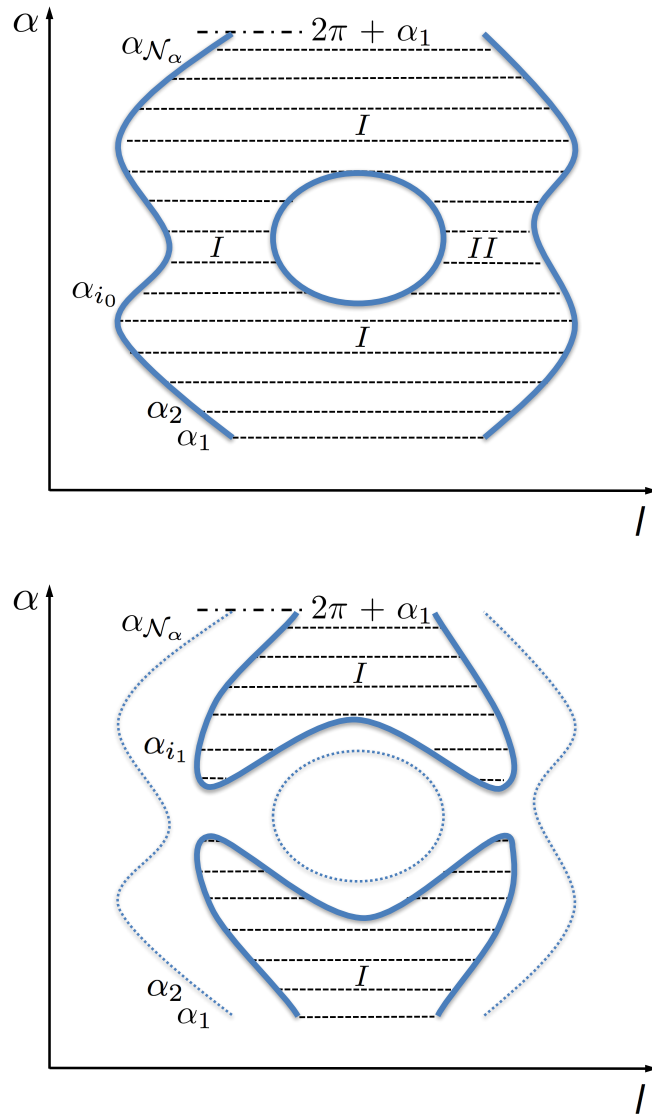


Figure 4.3: Top: sketch of grid in  $\alpha$  space at fixed  $\lambda$ . The tangential derivatives are discretized as in equations (4.23) and (4.24) except close to the limits of the grid ( $\alpha_1$  and  $\alpha_{N_\alpha}$ ) and to bifurcations (e.g.  $\alpha_{i_0}$ ); there, equations (4.25), (4.26), (4.27), (4.28) and (4.29) are used instead. Bottom: sketch of grid in  $\alpha$  space at larger  $\lambda$  (the grid at smaller  $\lambda$  is plotted for reference in dashed thin line).  $\alpha_{i_1}$

is a point where the backward derivative is discretized as discussed in equation (4.30).

Non-centered finite differences with second-order accuracy are used. For a given flux-surface, for each solution of the drift-kinetic equation, the sign of the coefficient in front of  $\partial_\alpha g_b$  (i.e. the direction of the flow in the  $\alpha$  direction) indicates whether forward

$$\partial_\alpha g_b|_{i,j,w} = \frac{-g_{i+2,j,w} + 4g_{i+1,j,w} - 3g_{i,j,w}}{2\Delta\alpha}, \quad (4.23)$$

or backward differences

$$\partial_\alpha g_b|_{i,j,w} = \frac{g_{i-2,j,w} - 4g_{i-1,j,w} + 3g_{i,j,w}}{2\Delta\alpha}, \quad (4.24)$$

should be used, with  $\Delta\alpha = \alpha_{i+1} - \alpha_i$ . To construct the derivatives with respect to  $\alpha$  without much computational cost, we discretize separately the terms  $I_{v_E,\alpha}\partial_\alpha g$  and  $v_{d,b}I_{v_M,\alpha}\partial_\alpha g$  using a total of four matrices for a given flux surface. One corresponds to forward differences being used everywhere, and another one corresponds to backward differences everywhere. When solving equation (4.1), one of these two matrices will describe the  $I_{v_E,\alpha}\partial_\alpha g$  term, depending on the sign of  $E_r$ . The other two matrices correspond to two  $\lambda$  (and  $w$ )-dependent discretizations, in which forward (backward) differences are used according to the sign of  $I_{v_M,\alpha}$ . One of these two matrices will describe the  $v_{d,b}I_{v_M,\alpha}\partial_\alpha g$  term, depending on the sign of  $v_{d,b}$ . Any matrix appropriate for describing equation (4.22) will thus be a linear combination of two of the four pre-calculated matrices, and a neoclassical simulation including ions and electrons and/or different values of the radial electric field will generally make use of the four of them.

Periodicity in  $\alpha$  is easily imposed by replacing equation (4.23) at  $i \geq N_\alpha - 1$  with

$$\begin{aligned} \partial_\alpha g_b|_{N_\alpha-1,j,w} &= \frac{(g_{N_\alpha,j,w} - g_{N_\alpha-1,j,w})(2\pi + \alpha_1 - \alpha_{N_\alpha-1})}{(2\pi + \alpha_1 - \alpha_{N_\alpha})\Delta\alpha} \\ &- \frac{(g_{1,j,w} - g_{N_\alpha-1,j,w})\Delta\alpha}{(2\pi + \alpha_1 - \alpha_{N_\alpha-1})(2\pi + \alpha_1 - \alpha_{N_\alpha})}, \end{aligned} \quad (4.25)$$

$$\begin{aligned} \partial_\alpha g_b|_{N_\alpha,j,w} &= \frac{(g_{1,j,w} - g_{N_\alpha,j,w})(2\pi + \alpha_2 - \alpha_{N_\alpha})}{(2\pi + \alpha_1 - \alpha_{N_\alpha})\Delta\alpha} \\ &- \frac{(g_{2,j,w} - g_{N_\alpha,j,w})(2\pi + \alpha_1 - \alpha_{N_\alpha})}{(2\pi + \alpha_1 - \alpha_{N_\alpha})\Delta\alpha}, \end{aligned} \quad (4.26)$$

respectively, and equation (4.24) at  $i \leq 2$  with

$$\begin{aligned} \partial_\alpha g_b|_{2,j,w} &= -\frac{(g_{1,j,w} - g_{2,j,w})(\alpha_{N_\alpha} - \alpha_2 - 2\pi)}{(\alpha_{N_\alpha} - \alpha_1 - 2\pi)\Delta\alpha} \\ &+ \frac{(g_{N_\alpha,j,w} - g_{2,j,w})\Delta\alpha}{(\alpha_{N_\alpha} - \alpha_2 - 2\pi)(\alpha_{N_\alpha} - \alpha_1 - 2\pi)}, \end{aligned} \quad (4.27)$$

$$\begin{aligned} \partial_\alpha g_b|_{1,j,w} &= -\frac{(g_{N_\alpha,j,w} - g_{1,j,w})(\alpha_{N_\alpha-1} - \alpha_1 - 2\pi)}{(\alpha_{N_\alpha} - \alpha_1 - 2\pi)\Delta\alpha} \\ &+ \frac{(g_{N_\alpha-1,j,w} - g_{1,j,w})(\alpha_{N_\alpha} - \alpha_1 - 2\pi)}{(\alpha_{N_\alpha-1} - \alpha_1 - 2\pi)\Delta\alpha}, \end{aligned} \quad (4.28)$$

respectively. We note that, since  $\iota$  is generally irrational,  $2\pi + \alpha_1 - \alpha_{N_\alpha}$  will e.g. be slightly smaller than  $\Delta\alpha$

We also note that bifurcations do not pose a problem for  $\alpha$ -derivatives, due to  $g_b$  being continuous in  $\alpha$ . For example, in the vicinity of  $\alpha_{i_0}$  in figure 4.3 (top) the forward derivative is discretized

$$\begin{aligned}
\partial_\alpha g_b|_{i_0-2,j,I} &= \frac{-g_{i_0-2,j,I} + 4g_{i_0-1,j,I} - 3g_{i_0,j,I}}{2\Delta\alpha} \\
&= \frac{-g_{i_0-2,j,I} + 4g_{i_0-1,j,I} - 3g_{i_0,j,II}}{2\Delta\alpha}, \\
\partial_\alpha g_b|_{i_0-1,j,I} &= \frac{-g_{i_0-1,j,I} + 4g_{i_0,j,I} - 3g_{i_0+1,j,I}}{2\Delta\alpha} \\
&= \frac{-g_{i_0-1,j,I} + 4g_{i_0,j,II} - 3g_{i_0+1,j,II}}{2\Delta\alpha}, \\
\partial_\alpha g_b|_{i_0,j,I} &= \frac{-g_{i_0,j,I} + 4g_{i_0+1,j,I} - 3g_{i_0+2,j,I}}{2\Delta\alpha}, \\
\partial_\alpha g_b|_{i_0,j,II} &= \frac{-g_{i_0,j,II} + 4g_{i_0+1,j,II} - 3g_{i_0+2,j,II}}{2\Delta\alpha}, \\
\partial_\alpha g_b|_{i_0+1,j,I} &= \frac{-g_{i_0+1,j,I} + 4g_{i_0+2,j,I} - 3g_{i_0+3,j,I}}{2\Delta\alpha}, \\
\partial_\alpha g_b|_{i_0+1,j,II} &= \frac{-g_{i_0+1,j,II} + 4g_{i_0+2,j,II} - 3g_{i_0+3,j,II}}{2\Delta\alpha}, \\
\partial_\alpha g_b|_{i_0+2,j,I} &= \frac{-g_{i_0+2,j,I} + 4g_{i_0+3,j,I} - 3g_{i_0+4,j,I}}{2\Delta\alpha}, \\
\partial_\alpha g_b|_{i_0+2,j,II} &= \frac{-g_{i_0+2,j,II} + 4g_{i_0+3,j,II} - 3g_{i_0+4,j,I}}{2\Delta\alpha}, \\
\partial_\alpha g_b|_{i_0+3,j,I} &= \frac{-g_{i_0+3,j,I} + 4g_{i_0+4,j,I} - 3g_{i_0+5,j,I}}{2\Delta\alpha}, \\
\partial_\alpha g_b|_{i_0+3,j,II} &= \frac{-g_{i_0+3,j,II} + 4g_{i_0+4,j,I} - 3g_{i_0+5,j,I}}{2\Delta\alpha}, \tag{4.29}
\end{aligned}$$

where continuity of  $g_b$  has been used in the first two expressions of equation (4.29). Equivalent expressions can be obtained for the backward derivative.

One final caveat has to be made. In an omnigenous magnetic field, the contours of minimum  $B$  on a flux surface must encircle the plasma (toroidally, poloidally, or helically). This is not true for a generic stellarator, in which local minima of  $B$  exist on the flux surface. Close to these minima, moving in  $\alpha$  at constant large  $\lambda$  is not always possible, as these trajectories may not exist. This situation is illustrated in figure 4.3 (bottom), at  $\alpha_{i_1}$ . At,  $\alpha_{i_1}$ , instead of equation (4.24), we use

$$\partial_\alpha g_b|_{i_1,j,w} = \frac{g_{i_1-2,j_0,w} - 4g_{i_1-1,j,w} + 3g_{i_1,j,w}}{2\Delta\alpha}. \tag{4.30}$$

and we have implemented two models: in one,  $\lambda_{j_0}$  is the value of  $\lambda$  closest to  $\lambda_j$  in which trajectories exist for all  $\alpha$ ; in the second model,  $\lambda_{j_0}$  is the closest value of  $\lambda$  in which trajectories exist at  $\alpha_{i_0-2}$ . The relative differences between the two models are smaller than e.g. the error bars of DKES in figure 11.3. We note that (with different manifestations for other choices of velocity coordinates) an incorrect treatment of this kind of particles is common to all existing radially local codes.

For each of the species  $b$ , we end up with an equation that is linear in  $g_b$  and can be

written as a linear problem in matrix form. The matrix that represents

$$\left( I_{v_{M,\alpha}} + \frac{1}{v_{d,b}} I_{v_{E,\alpha}} \right) \partial_\alpha + \frac{\nu_{\lambda,b}}{v_{d,b}} \partial_\lambda \nu \partial_\lambda \quad (4.31)$$

is square with approximately  $\mathcal{N}_\lambda \times \mathcal{N}_\alpha$  elements per row, and sparse, with  $\sim 6$  non-zero elements per row: between 3 and 5 for the  $\alpha$  derivatives, and typically 2 additional points for the collision operator. Although their relative weight varies with  $\nu_{\lambda,b}$ ,  $v_{d,b}$  and  $\partial_\psi \varphi_0$ , the non-zero elements are always at the same position for a given flux-surface, which can be used to save computing time, by using the four pre-computed matrices described above.

We solve the linear problem with a direct solver from the PETSc library [Balay et al., 1997, 2019a,b] based on LU factorization. The reason is that the matrix is not large enough to require iterative methods, and reusing the LU factorization greatly accelerates the solution of the quasineutrality equation, as discussed in §4.5.

## 4.5 Solution of the quasineutrality equation

We will solve the quasineutrality equation by means of a response matrix approach (similar methods are used in gyrokinetics for the calculation of the electrostatic potential fluctuations [Kotschenreuther et al., 1995]). Let us first rewrite equations (4.1) and (3.22) making explicit the dependence on  $\varphi_1$ :

$$\begin{aligned} & \left( I_{v_{M,\alpha}} + \frac{I_{v_{E,\alpha}}}{v_{d,b}} \right) \partial_\alpha g_b - \frac{\nu_{\lambda,b}}{v_{d,b}} \partial_\lambda I_\nu \partial_\lambda g_b \\ &= \left( I_{v_{M,\psi}} - \int_{l_{b_1}}^{l_{b_2}} \frac{dl}{\sqrt{1-\lambda B}} \frac{B_\theta \partial_\zeta \varphi_1 - B_\zeta \partial_\theta \varphi_1}{|B_\zeta + \iota B_\theta|} \right) F_{M,b} \Upsilon_b, \end{aligned} \quad (4.32)$$

$$\left( \frac{Z_i}{T_i} + \frac{1}{T_e} \right) \varphi_1 = \frac{2\pi}{en_e} \sum_b Z_b \int_0^\infty dv \int_{B_{\max}^{-1}}^{B^{-1}} d\lambda \frac{v^3 B}{|v_\parallel|} g_b. \quad (4.33)$$

It can be observed that equation (4.32) is linear in  $\varphi_1$ , and therefore the response of the distribution function  $g_b$  (and of its velocity integral) of species  $b$  to certain  $\varphi_1$  can be calculated as a superposition of the responses to a complete set of harmonics that parametrize  $\varphi_1(\theta, \zeta)$ . We can perform this parametrization efficiently thanks to the Fast Fourier Transform, using  $\mathcal{N} = 2(2\mathcal{N}_n + 1)(\mathcal{N}_m + 1)$  coefficients:

$$\varphi_1(\theta, \zeta) = \sum_{-\mathcal{N}_n < n < \mathcal{N}_n} \sum_{0 < m < \mathcal{N}_m} \left( \varphi_{mn}^{(c)} \cos(m\theta + Nn\zeta) + \varphi_{mn}^{(s)} \sin(m\theta + Nn\zeta) \right) \quad (4.34)$$

(the grid defined in §4.3 is not uniform in  $\theta$ , so an interpolation is done before the Fourier transform). We can now denote  $u_k(\theta, \zeta)$  each of the  $\mathcal{N}$  basis elements (e.g.  $\cos(\theta + 2N\zeta)$ ) and the combined system of drift-kinetic and quasineutrality equation can be symbolically written as

$$\boldsymbol{\varphi}_1 = \boldsymbol{\varphi}_1^0 + \mathbf{A} \boldsymbol{\varphi}_1, \quad (4.35)$$

where  $\varphi_1$  is a vector whose  $\mathcal{N}$  components are the coefficients of the expansion of  $\varphi_1$  in equation (4.34) and  $\mathbf{A}$  is a generally dense  $\mathcal{N} \times \mathcal{N}$  matrix. In this linear system, the right-hand side  $\varphi_1^0$  can be obtained by solving equation (4.32) for all the kinetic species with  $\varphi_1 = 0$ , inserting the solution into equation (4.33) and then Fourier-transforming the result following equation (4.34). Next, we fill the matrix  $\mathbf{A}$ : the  $k$ th row is obtained by solving equation (4.32) with  $\varphi_1 = u_k$ , inserting the solution into equation (4.33), Fourier-transforming and then subtracting  $\varphi_1^0$  from the result. Once  $\varphi_1^0$  and  $\mathbf{A}$  have been filled, the new linear system can easily be solved, e.g. using a new LU decomposition, to obtain  $\varphi_1$ , i.e., the set of coefficients  $\varphi_{mn}^{(c)}$  and  $\varphi_{mn}^{(s)}$  that parametrize the solution to quasineutrality. Finally, since the response of  $g_b$  to every basis element has already been computed, a simple linear combination yields the distribution function that is solution of the drift-kinetic and quasineutrality equations, without requiring an additional solve of the former.

In summary, the drift-kinetic equation is solved a total of  $\mathcal{N}+1$  times (for each species), but LU factorization is done once (for each value of  $v$ ). The linearity of the system of equations due to the smallness of  $\varphi_1$ , together with the method that we have chosen for solving the drift-kinetic equation, yields a large reduction of the computing time needed to solve the system of equations: the code is roughly  $\mathcal{N}$  faster (with  $\mathcal{N}$  ranging from 100 to 1000), with respect to an equivalent code that allowed the particle orbits be modified by  $\varphi_1$ .

# Chapter 5

## Installing KNOSOS

This chapter describes the steps that you have to take, from the moment when you decide to download KNOSOS, in order to have a correctly working version of the code. At the moment, KNOSOS is being developed at the `euler` cluster at CIEMAT. This means that, if you have access to an account there, everything (compiling, running, etc) will probably be much easier. Note that many problems can be run in your personal computer, as long as you have installed the appropriate libraries.

### 5.1 Public repository

The source code for KNOSOS is [hosted in a GitHub repository](#) at:

<https://github.com/joseluisvelasco/KNOSOS>

You can obtain the KNOSOS source code by:

- Downloading all the files one by one.
- Logging in GitHub and cloning the repository, as described in  
<https://help.github.com/articles/cloning-a-repository/>.

The latter option is preferable, since it makes faster the download of future updates of the code and, if you are a collaborator with writing permissions, allows you to upload your source code.

### 5.2 Setting up KNOSOS on a new system

The first time that you try to run KNOSOS, you may need to install some software, and to set a few environment variables.

#### 5.2.1 System requirements

In order to compile and run KNOSOS, your system administrator should have installed:

- The `PETSc` library for solving large linear systems.

- An implementation of MPI for parallel runs.
- [FFTW](#) for computing the discrete Fourier transform.
- [LAPACK](#) and [BLAS](#) for algebra of small matrices.

You need to determine the `intel` compiler and include PETSc in `LD_LIBRARY_PATH`. At `euler`, you can do that by executing

```
export LD_LIBRARY_PATH=$LD_LIBRARY_PATH:/home/localsoft/petsc-3.7.4/real/lib/
```

and

```
source /home/localsoft/intel-12/bin/compilervars.sh intel64
```

Note that KNOSOS can still run without the two first libraries (PETSc and MPI), although limited to sequential runs and small enough problems.

In a laptop or desktop computer under `macOS`, you will need to take at least the following steps (if you have not before) from a Terminal:

- Install `brew` by executing

```
/usr/bin/ruby -e "$(curl -fsSL https://raw.githubusercontent.com/Homebrew/install/master/install)"
```

- Install the `gfortran` compiler by executing `brew install gcc`
- Install the LAPACK and BLAS libraries by executing `brew install lapack`
- Install the FFTW libraries by executing `brew install fftw`
- Copy file `libfftw3.a` with the sources (and rename with your system name, e.g. `libfftw3_Darwin.a`).

There is an identical procedure for `Linux` if you first install [Linuxbrew](#). Nevertheless, you may prefer the more standard commands: `sudo apt-get install gcc`, `sudo apt-get install fftw`, etc.

### 5.2.2 Makefile

At the moment, KNOSOS runs on the clusters `euler`, `fusco` and `dirac` at CIEMAT, and at workstation `TASK3D-1` and server `egcalc` at NIFS at cluster `ttfamilyl` draco at IPP Greifswald, and at several computers, both under `macOS` and under `xUbuntu Linux`. `Makefile` detects the system where it is running and sets the compiler, compiler flags, library paths, etc, accordingly.

### 5.2.3 Next steps

The following chapters explain how to run KNOSOS: chapter [6](#) provides an overview, and chapters [7](#), [8](#), [9](#) and [10](#) contain all the details of the input and output files. Chapter [11](#) provides examples published in [[Velasco et al., 2019](#)] that can be reproduced by the user.

# Chapter 6

## Running KNOSOS

This brief chapter describes the general workflow of the calculation and gives step-by-step explanation on what files you need to prepare in order to run the code. More details are given in the following chapters.

### 6.1 General workflow

The main loop is contained in `knosos.f90`, and it takes the following steps:<sup>\*</sup>

- Read input files with simulation parameters. See chapter 7. In particular:
  - Determine the equations solved and methods to be used.
  - Determine the species to be calculated and their neoclassical regime(s).
  - Determine the flux-surfaces to be calculated.
- Initialize MPI, PETSc and the random number generator.
- Allocate some transport-related quantities.
- Perform a loop in samples (\* if error bars are calculated, see chapter 8).
  - Perform a loop in time steps \*.
    - \* Perform a first loop in flux-surfaces:
      - Read the magnetic field. See chapter 9.
      - Read the plasma profiles. See chapter 8.
      - Read and/or create database of monoenergetic transport coefficients\*. See appendix B.
      - Calculate the flux for each flux surface (including drift-kinetic eq., ambipolarity and quasineutrality). See chapter 10.
      - **Evolve plasma profiles\***.
  - Average on samples\* .
  - End MPI and PETSc.

---

<sup>\*</sup>In this chapter \* denotes optional tasks.

## 6.2 How to run KNOSOS

In order for KNOSOS to run, several input files should be prepared. Except otherwise, the files can be at the working directory (the folder where KNOSOS is running) or at the parent folder, and KNOSOS will use preferentially the former. In some other cases, the files can only be at the working directory. In the following subsections, we show the default cases (i.e., the simulations that are done if no input is provided) and how to provide input if you want to run different cases (many more details of the input files are given in chapters 7, 8 and 9). If you are using KNOSOS from TASK3D [Yokoyama et al., 2017], the appropriate inputs are automatically generated (in particular, note that multi-species simulations are not available yet).

### 6.2.1 Model

The default calculation solves ambipolarity and quasineutrality, including the effect of the tangential magnetic drift and the correct (compressible)  $\mathbf{E} \times \mathbf{B}$  drift. If you want a different kind of simulation, create a `input.model` file and modify it as follows (more details in §7.1):

<i>If you</i>	<i>you have to</i>
- do not want to solve ambipolarity:	set <code>SOLVE_AMB</code> to .FALSE.
- do not want to solve quasineutrality:	set <code>SOLVE_QN</code> to .FALSE.
- want to solve a trivial version quasineutrality:	set <code>TRIVIAL_QN</code> to .TRUE.
- do not want to include the tangential magnetic drift:	set <code>TANG_VM</code> to .FALSE.
- want to use a DKES-like incompressible $\mathbf{E} \times \mathbf{B}$ drift:	set <code>INC_EXB</code> to .TRUE.
- want to use a DKES database of transport coefficients:	set <code>REGB</code> to -1
- want to calculate a DKES-like database of transport coefficients:	set <code>CALC_DB</code> to .TRUE.
- want to calculate DKES-like database of transport coefficients and exit:	set <code>ONLY_DB</code> to .TRUE.
- want to compare several models of the quasineutrality equation:	set <code>COMPARE_MODELS</code> to .TRUE.
- want to scan in the collisionality, rotational transform, magnetic shear, number of periods, aspect ratio, major radius and/or magnetic field strength:	set values different than 1 for <code>FN</code> , <code>FI</code> , <code>FS</code> , <code>FP</code> , <code>FE</code> , <code>FR</code> and/or <code>FB</code>

- want to solve a particular physics problem:

set `TASK3D`, `NEOTRANSP`, `PENTA`, `SATAKE`, or `JPP` to `.TRUE.`.

### 6.2.2 Species

The default calculation uses adiabatic electrons, hydrogen at low-collisionality and no impurities:  $1/\nu$ ,  $\sqrt{\nu}$  and sb-p (the exception is the calculation of DKES-like coefficients, if you have set `ONLY_DB` to `.TRUE.`, which does not need this information). If you want a different kind of simulation, create a `input.species` file and modify it as follows (more details in §7.4):

<i>If you</i>	<i>you have to</i>
- want to change the main ions:	modify <code>ZB</code> and/or <code>AB</code>
- want some species to be in a different regime (or use DKES):	modify <code>REGB</code>
- want to add more species:	increase <code>NBB</code> , add entries to <code>ZB</code> , <code>AB</code> and <code>REGB</code> and set <code>ZEFF</code>

### 6.2.3 Plasma profiles

You need to provide values for the density, temperature and (except if `SOLVE_AMB` is set to `.TRUE.`), the radial electric field. Again, the exception are the calculation of DKES-like coefficients (which does not need this information), or some specific physics problems (if `SATAKE` or `JPP` or are set to `.TRUE.`). More precisely, you need to provide the electron density (impurities, if any, are trace, and the flux-surface-averaged ion density is trivially set by quasineutrality, even if `SOLVE_QN` is set to `.FALSE.`) and the electron and ion temperature (all ions have the same temperature, and  $T_e = T_i$  is set if the electron temperature is not provided). The radial electric field can be provided if ambipolarity is not solved, otherwise it is zero. All this can be done by (more details in §8.2)

- using files `ne_in.d`, `te_in.d`, `ti_in.d` and/or `ph_in.d` if you want to calculate one flux-surface, or
- using profiles (`neprof_r.d`, `teprof_r.d`, `tiprof_r.d` and/or `phprof_r.d`) and determining the flux surface(s). The default flux-surface is  $s = 1$ , which you can change by creating a file `input.surfaces` in the working directory (see §7.3), and modifying `NS` and/or `S`.
- using file `//profiles.d`, `//profiles_DR.txt`, `//profiles_neotransp.dat`, `//profiles.txt`, `//prof-file.txt` or `//input-prof.txt`, that contain all the profiles, and determining the flux surface(s).

### 6.2.4 Magnetic configuration

For some specific physics problems (e.g. if `JPP` is set to `.TRUE.`), there is a default magnetic configuration. Otherwise, you need to provide the magnetic configuration (Fourier modes of  $B$  in Boozer coordinates, rotational transform  $\iota$ , toroidal and poloidal components of the magnetic field  $B_\theta$  and  $B_\zeta$ , and toroidal flux) at least at the flux-surface of interest, and at one additional close flux-surface if, as usual, you want to account for the tangential magnetic drift in the drift-kinetic equation. All this can be done by (more details in §9.2)

- using file `ddkes2.data` (and maybe `add_ddkes2.data`), which must be at the working directory, or
- using files `boozmn.data` or `boozer.txt`, and determining the flux surface(s). The default flux-surface is  $s = 1$ , which you can change by creating a file `input.surfaces` in the working directory (see §7.3), and modifying `NS` and/or `S`.

### 6.2.5 Parameters

The default values should work for your problem: no unnecessary information is shown, well-tested algorithms are used, the magnetic field is calculated with all the modes available at the input file, and everything is done reasonable precision. However, if you think that your results have not converged or you want to do some debugging, you can create a `input.parameters` file and modify it as follows (more details in §7.2):

<i>If you</i>	<b>you have to</b>
- want to plot many intermediate results:	set <code>DEBUG</code> to <code>.TRUE.</code>
- want to plot the time spent at every major routine:	set <code>TIME</code> to <code>.TRUE.</code>
- want to plot the distribution function:	set <code>PLOTG</code> to <code>.TRUE.</code>
- want to do the bounce-averages over the underlying omnigenous magnetic field:	set <code>USE_B0pB1</code> or <code>USE_B1</code> to <code>.TRUE.</code>
- want to calculate analytically as much as possible of the bounce-integrals:	set <code>REMOVE_DIV</code> to <code>.TRUE.</code>
- do not want to use trigonometric identities to calculate the magnetic field:	set <code>DELTA</code> to <code>.FALSE.</code>
- want to keep less modes of the magnetic field spectrum:	reduce <code>TRUNCATE_B</code>
- want to keep less modes of the magnetic field spectrum:	increase <code>PREC_B</code>

- want to calculate the bounce points with more precision:	reduce <code>PREC_EXTR</code>
- want to calculate the bounce integrals with more precision:	reduce <code>PREC_BINT</code>
- want to calculate the monoenergetic contribution to the flux with more precision:	increase <code>MAL</code> and/or <code>MLAMBDA</code>
- want to calculate the monoenergetic contribution to the flux with more precision:	reduce <code>PREC_DQDV</code>
- want to calculate the velocity convolution of monoenergetic coefficients with more precision:	reduce <code>PREC_INTV</code>
- want less points in your database of monoenergetic transport coefficients:	modify <code>NEFIELD</code> and <code>EFIELD</code> and/or <code>NCMUL</code> and <code>CMUL</code>
- want to modify the number of points or the range of values when solving ambipolarity:	modify <code>NER</code> , <code>ERMIN</code> and/or <code>ERMAX</code>
- want to calculate the ambipolar $E_r$ with more precision:	reduce <code>ERACC</code>
- want to increase the statistics when estimating the error bars:	increase <code>NERR</code>
- want to set error bars for the inputs:	set <code>IPERR</code>

# Chapter 7

## Inputs

In this chapter, we describe all the variables that can be included in four input files:

- `input.model.`
- `input.parameters.`
- `input.surfaces.`
- `input.species.`

Each of them contains a namelist: `model`, `parameters`, `surfaces`, and `species`, respectively. The plasma profiles and magnetic configuration are set by reading different files, as described in chapters 8 and 9 respectively. Note that the variables of these namelist are given specific values if `TASK3D` is set to `.TRUE.`, and the values set by the corresponding files are mostly overwritten. We recommend that you read chapters 3 and 4 in order to understand better what the variables do. Examples of these files are provided later, so that the user can reproduce the results of chapter 11.

### 7.1 The `model` namelist

This namelist is contained in file `input.model`, and it determines what physics equations are solved (what version of the drift-kinetic equation, ambipolarity, quasineutrality...). This means that you should decide the values of all the variables (a summary is available in §6.2.1); otherwise, KNOSOS gives them default values which means that you may end up with a simulation different than what you wanted.

**SOLVE\_AMB**

*Purpose:* Determine the electrostatic potential

*Type:* LOGICAL

*Effect if .TRUE.:* The ambipolarity equation is solved

*Default value:* .TRUE.

*Misc.:* -

*Ref.:* Chapter 3

---

**TRIVIAL\_AMB**

*Purpose:* Determine the electrostatic potential

*Type:* LOGICAL

*Effect if .TRUE.:* The radial electric field is the ion root value, according to the input density and ion temperature, with ions in the  $1/\nu$  regime

*Default value:* .FALSE.

*Misc.:* Overwrites **SOLVE\_AMB**

*Ref.:* e.g. [Maaßberg et al., 1999]

---

**SOLVE\_QN**

*Purpose:* Determine the electrostatic potential

*Type:* LOGICAL

*Effect if .TRUE.:* The quasineutrality equation is solved

*Default value:* .TRUE.

*Misc.:* -

*Ref.:* §4.5, §11.3

---

## TRIVIAL\_QN

*Purpose:* Determine the electrostatic potential

*Type:* LOGICAL

*Effect if .TRUE.:* A simplified version of the quasineutrality equation is solved very fast, without including  $\varphi_1$  in the source of the DKE, and only  $\varphi_1^0$  is obtained

*Default value:* .FALSE.

*Misc.:* Overwrites **SOLVE\_QN**. Correct for the  $\sqrt{\nu}$  and approximately regime valid for others [Calvo et al., 2018b]

*Ref.:* §4.5

---

## TRIVIAL\_QN

*Purpose:* Determine the electrostatic potential

*Type:* LOGICAL

*Effect if .TRUE.:* A simplified version of the quasineutrality equation is solved very fast, without including  $\varphi_1$  in the source of the DKE, and only  $\varphi_1^0$  is obtained

*Default value:* .FALSE.

*Misc.:* Correct for the  $\sqrt{\nu}$  and approximately regime valid for others [Calvo et al., 2018b]

*Ref.:* §4.5

---

## ZERO\_PHI1

*Purpose:* Determine the electrostatic potential

*Type:* LOGICAL

*Effect if .TRUE.:* Set  $\varphi_1 = 0$

*Default value:* .FALSE.

*Misc.:*

*Ref.:* §4.5

---

**ONLY\_PHI1**

*Purpose:* Determine the electrostatic potential

*Type:* LOGICAL

*Effect if .TRUE.:* Quasineutrality equation is solved, but time is saved by not calculating the radial flux of bulk species

*Default value:* .FALSE.

*Misc.:* -

*Ref.:*

---

**TANG\_VM**

*Purpose:* Set details of the drift-kinetic equation

*Type:* LOGICAL

*Effect if .TRUE.:* The tangential magnetic drift is included

*Default value:* .TRUE.

*Misc.:* -

*Ref.:* Chapter 3, §9.3, §11.2, [Calvo et al., 2017]

---

**INC\_EXB**

*Purpose:* Set details of the drift-kinetic equation

*Type:* LOGICAL

*Effect if .TRUE.:* A DKES-like incompressible  $\mathbf{E} \times \mathbf{B}$  drift is used

*Default value:* .FALSE.

*Misc.:* -

*Ref.:* §9.3, §11.2, [Hirshman et al., 1986; Beidler et al., 2007]

---

**CLASSICAL**

*Purpose:* Set details of the drift-kinetic equation  
*Type:* LOGICAL  
*Effect if .TRUE.:* Add classical contribution to neoclassical impurity transport  
*Default value:* .TRUE.  
*Misc.:* Ignored for bulk species; negligible in many cases  
*Ref.:* §A.3

---

**FRICTION**

*Purpose:* Set details of the drift-kinetic equation  
*Type:* LOGICAL  
*Effect if .TRUE.:* Add the contribution of interspecies friction to neoclassical impurity transport  
*Default value:* .TRUE.  
*Misc.:* Ignored for bulk species; negligible in some cases  
*Ref.:* §A.3

---

**ANISOTROPY**

*Purpose:* Set details of the drift-kinetic equation  
*Type:* LOGICAL  
*Effect if .TRUE.:* Add the contribution of pressure anisotropy to neoclassical impurity transport  
*Default value:* .TRUE.  
*Misc.:* Ignored for bulk species; negligible in some cases  
*Ref.:* §A.3

---

**D\_AND\_V**

*Purpose:* Determine the electrostatic potential and set details of the drift-kinetic equation

*Type:* INTEGER

*Effect:* Depending on the value, different quantities characterizing the impurity flux are determined:

- 2: flux driven by pressure anisotropy and by friction
- 3: flux driven by pressure anisotropy and diffusive coefficient and pinch caused by friction
- 5: flux driven by pressure anisotropy and coefficients corresponding to  $E_r/T_i$ ,  $T'_i/T_i$  and  $n'_i/n_i$ .

*Default value:* 5

*Misc.:* -

*Ref.:* -

---

**COMPARE\_MODELS**

*Purpose:* Determine the electrostatic potential and set details of the drift-kinetic equation

*Type:* LOGICAL

*Effect if .TRUE.:* If **SOLVE\_QN**, the calculation is done as specified by **TANG\_VM** and **REGB** and, additionally, with some simplifications from that case: with one adiabatic species (if both **REGB(1)** and **REGB(2)** are set to 3) and as if **TRIVIAL\_QN**.

*Default value:* .FALSE.

*Misc.:* -

*Ref.:* Chapter 10

---

**CALC\_DB**

*Purpose:* Set details of the drift-kinetic equation  
*Type:* LOGICAL  
*Effect if .TRUE.:* A DKES-like database of monoenergetic coefficients is calculated with KNOSOS  
*Default value:* .FALSE.  
*Misc.:* -  
*Ref.:* §11.1, appendix B

---

**ONLY\_DB**

*Purpose:* Set details of the drift-kinetic equation  
*Type:* LOGICAL  
*Effect if .TRUE.:* Only the DKES-like database of monoenergetic coefficients is calculated, not the flux  
*Default value:* .FALSE.  
*Misc.:* Ignored if .NOT.**CALC\_DB**  
*Ref.:* §11.1, appendix B

---

**FN**

*Purpose:* Scan in parameters  
*Type:* REAL\*8  
*Effect:* The collisionality is artificially multiplied by **FN** keeping the densities and temperatures constant  
*Default value:* 1.0  
*Misc.:* -  
*Ref.:* §9.6, [Satake et al., 2018]

---

**FI**

*Purpose:* Scan in parameters

*Type:* REAL\*8

*Effect:* The rotational transform is multiplied by **FI**, keeping the toroidal flux  $\Psi_t$  constant

*Default value:* 1.0

*Misc.:* The poloidal flux  $\Psi_p$  changes accordingly

*Ref.:* §[9.6](#)

---

**FS**

*Purpose:* Scan in parameters

*Type:* REAL\*8

*Effect:* The magnetic shear is multiplied by **FS** keeping the rotational transform  $\iota$  constant

*Default value:* 1.0

*Misc.:* Set to 0 if **ONLY\_DB**. Ignored if .NOT.**TANG\_VM**

*Ref.:* §[9.6](#), citepsatake2018iaea

---

**FP**

*Purpose:* Scan in parameters

*Type:* REAL\*8

*Effect:* The number of periods is multiplied by **FP** keeping the rotational transform  $\iota$  constant

*Default value:* 1.0

*Misc.:* The number of periods needs to be integer

*Ref.:* §[9.6](#)

---

**FE**

*Purpose:* Scan in parameters

*Type:* REAL\*8

*Effect:* The inverse aspect ratio is multiplied by **FS**, keeping the major radius  $R$  constant

*Default value:* 1.0

*Misc.:* The minor radius  $a$ , the toroidal and poloidal fluxes  $\Psi_t$  and  $\Psi_p$ , the radial derivatives and the modes of  $B$  different than  $B_{00}$  change accordingly

*Ref.:* §9.6, [Calvo et al., 2018b]

---

**FR**

*Purpose:* Scan in parameters

*Type:* REAL\*8

*Effect:* The major radius is multiplied by **FR**, keeping the aspect ratio constant

*Default value:* 1.0

*Misc.:* The minor radius  $a$ , the toroidal and poloidal fluxes  $\Psi_t$  and  $\Psi_p$ , the radial derivatives and covariant components of the magnetic field  $B_\zeta$  and  $B_\theta$  change accordingly

*Ref.:* §9.6, [Calvo et al., 2018b]

---

**FB**

*Purpose:* Scan in parameters

*Type:* REAL\*8

*Effect:* The magnetic field is multiplied by **FB**, keeping the size constant

*Default value:* 1.0

*Misc.:* The toroidal and poloidal fluxes  $\Psi_t$  and  $\Psi_p$ , the radial derivatives and covariant components of the magnetic field  $B_\zeta$  and  $B_\theta$  change accordingly

*Ref.:* §9.6

**FNE**

*Purpose:* Scan in parameters

*Type:* REAL\*8

*Effect:* The density of all species  $n_b$  is artificially multiplied by **FNE** keeping its normalized radial derivative  $\partial_\psi \log n_b$  constant

*Default value:* 1.0

*Misc.:* -

*Ref.:*

---

**FTE**

*Purpose:* Scan in parameters

*Type:* REAL\*8

*Effect:* The electron temperature  $T_e$  is artificially multiplied by **FTE** keeping its normalized radial derivative  $\partial_\psi \log T_e$  constant

*Default value:* 1.0

*Misc.:* -

*Ref.:*

---

**FTI**

*Purpose:* Scan in parameters

*Type:* REAL\*8

*Effect:* The ion temperature  $T_i$  is artificially multiplied by **FTI** keeping its normalized radial derivative  $\partial_\psi \log T_i$  constant

*Default value:* 1.0

*Misc.:* -

*Ref.:*

---

**FDLNE**

*Purpose:* Scan in parameters

*Type:* REAL\*8

*Effect:* The normalized radial derivative of the density of all species  $\partial_\psi \log n_b$  is artificially multiplied by **FDLNE** keeping the density  $n_b$  constant

*Default value:* 1.0

*Misc.:* -

*Ref.:* -

---

---

**FDLTE**

*Purpose:* Scan in parameters

*Type:* REAL\*8

*Effect:* The normalized radial derivative of the electron temperature  $\partial_\psi \log T_e$  is artificially multiplied by **FDLTE** keeping the temperature  $T_e$  constant

*Default value:* 1.0

*Misc.:* -

*Ref.:* -

---

---

**FDLTI**

*Purpose:* Scan in parameters

*Type:* REAL\*8

*Effect:* The normalized radial derivative of the electron temperature  $\partial_\psi \log T_i$  is artificially multiplied by **FDLTI** keeping the temperature  $T_i$  constant

*Default value:* 1.0

*Misc.:* -

*Ref.:* -

**FER**

*Purpose:* Scan in parameters

*Type:* REAL\*8

*Effect:* The radial electric field  $E_r$  is artificially multiplied by **FER**

*Default value:* 1.0

*Misc.:* -

*Ref.:*

---

**TASK3D**

*Purpose:* Particular physics problem

*Type:* LOGICAL

*Effect if .TRUE.:* **KNOSOS** is used from **TASK3D**

*Default value:* .FALSE.

*Misc.:* If you are running **KNOSOS** from **TASK3D**, this variable is set to .TRUE. automatically. But you may want to set **TASK3D** to .TRUE. if you want to run **KNOSOS** separately and reproduce **TASK3D** results.

*Ref.:* [Yokoyama et al., 2017]

---

**TASK3Dlike**

*Purpose:* Particular physics problem

*Type:* LOGICAL

*Effect if .TRUE.:* KNOSOS produces an additional output with the same format as if it were used from TASK3D

*Default value:* .FALSE.

*Misc.:* The parameters provided in the input files are not overwritten, as it happens when **TASK3D** is set to .TRUE.

*Ref.:*

---

**PENTA**

*Purpose:* Particular physics problem

*Type:* LOGICAL

*Effect if .TRUE.:* KNOSOS is used from PENTA

*Default value:* .FALSE.

*Misc.:* If you are running KNOSOS from PENTA, this variable is set to .TRUE. automatically. But you may want to set **PENTA** to .TRUE. if you want to run KNOSOS separately and reproduce PENTA results.

*Ref.:* [Spong, 2005]

---

**NEOTRANSP**

*Purpose:* Particular physics problem

*Type:* LOGICAL

*Effect if .TRUE.:* **KNOSOS** is used from **neotransp**

*Default value:* .FALSE.

*Misc.:* If you are running **KNOSOS** from **neotransp**, this variable is set to .TRUE. automatically. But you may want to set **NEOTRANSP** to .TRUE. if you want to run **KNOSOS** separately and reproduce **neotransp** results.

*Ref.:*

---

**SATAKE**

*Purpose:* Particular physics problem

*Type:* LOGICAL

*Effect if .TRUE.:* The shear-dependence of neoclassical toroidal viscosity in a perturbed tokamak is studied

*Default value:* .FALSE.

*Misc.:* -

*Ref.:* [Satake et al., 2018]

---

**JPP**

*Purpose:* Particular physics problem

*Type:* LOGICAL

*Effect if .TRUE.:* The quasineutrality equation is solved in several regimes

*Default value:* .FALSE.

*Misc.:* -

*Ref.:* [Calvo et al., 2018b]

## 7.2 The parameters namelist

This namelist is contained in file `input.parameters` and it includes simulation parameters, such us decisions on how to solve some equations and what to plot. The default values should be a good starting point for your simulation.

---

### GEN\_FLAG

*Purpose:* Debug

*Type:* array of LOGICAL

*Effect if .TRUE.:* Certain, non consolidated, parts of the code are used

*Default value:* .FALSE.

*Misc.:* -

*Ref.:* -

**DEBUG**

*Purpose:* Debug

*Type:* LOGICAL

*Effect if .TRUE.:* Additional information is plotted in files **fort.????**:

- The first figure denotes the type of information:
  - **fort.1???**: magnetic field;
  - **fort.2???**: bounce-averages;
  - **fort.3???**: discretization of the equation;
  - **fort.4???**: solution of DKE, ambipolarity and quasineutrality.
- The second figure determines more specifically the type of information.
- The two last figures denote the MPI process that has written the file.

(e.g. **fort.2003** contains the extreme points of  $B$  found by process **myrank=3**)

*Default value:* .FALSE.

*Misc.:* If MPI is not used, only **fort.??00** exist. This manual does not describe the content of these files, but if you want to switch **DEBUG** to .TRUE., you probably know it already

*Ref.:* -

---

**TIME**

*Purpose:* Debug

*Type:* LOGICAL

*Effect if .TRUE.:* The time spent at several routines is calculated and plot

*Default value:* .TRUE.

*Misc.:* -

*Ref.:* -

**I0**

*Purpose:* Debug

*Type:* INTEGER

*Effect:* Information about line integral is plotted:

- If **I0.GT.0**, those in well/point **I0**
- If **I0.EQ.0**, those in all wells/points

*Default value:* .FALSE.

*Misc.:* Ignored if .NOT.**DEBUG**

*Ref.:* -

---

**PLOTG**

*Purpose:* Debug

*Type:* LOGICAL

*Effect if .TRUE.:* The distribution function is plotted

*Default value:* .FALSE.

*Misc.:* -

*Ref.:*

---

**USE\_B0pB1**

*Purpose:* Describe the magnetic field structure  
*Type:* LOGICAL  
*Effect if .TRUE.:* Bounce integrals are done over  $B_0$  but the radial drift comes from  $B_0 + B_1$   
*Default value:* .FALSE.  
*Misc.:* For the moment,  $B_0$  and  $B_1$  have to be provided explicitly  
*Ref.:* §9.2, [Calvo et al., 2017; Velasco et al., 2018]

---

**USE\_B1**

*Purpose:* Describe the magnetic field structure  
*Type:* LOGICAL  
*Effect if .TRUE.:* Bounce integrals are done over  $B_0$  but the radial drift comes from  $B_1$   
*Default value:* .FALSE.  
*Misc.:* For the moment,  $B_0$  and  $B_1$  have to be provided explicitly  
*Ref.:* §9.2, [Calvo et al., 2017; Velasco et al., 2018]

---

**REMOVE\_DIV**

*Purpose:* Determine algorithms to be used  
*Type:* LOGICAL  
*Effect if .TRUE.:* Infinities are removed from the integrands when calculating bounce integrals  
*Default value:* .FALSE.  
*Misc.:* In cases with many different regions (ripple wells, etc), it does not save much time. It is useful if **USE\_B0pB1** or **USE\_B1**  
*Ref.:* §4.2.1

---

**DELTA**

*Purpose:* Determine algorithms to be used

*Type:* LOGICAL

*Effect if .TRUE.:* Algebraic identities are used to calculate the magnetic field strength along the field line

*Default value:* .TRUE.

*Misc.:* -

*Ref.:* §4.2.2

---

**TRUNCATE\_B**

*Purpose:* Set numerical resolution

*Type:* INTEGER

*Effect:* If positive, a maximum of **TRUNCATE\_B** modes of the Fourier representation of  $B(\theta, \zeta)$  are kept.

*Default value:* -200

*Misc.:* Less modes than **TRUNCATE\_B** may be kept, depending on **PREC\_B**

*Ref.:* §4.2.2

---

**PREC\_B**

*Purpose:* Set numerical resolution

*Type:* REAL\*8

*Effect:* Neglect modes of the Fourier representation of  $B(\theta, \zeta)$  whose amplitude is smaller than **PREC\_B**

*Default value:*  $10^{-5}$

*Misc.:* Modes larger than **PREC\_B** may be neglected as well, depending of on **TRUNCATE\_B**

*Ref.:* §4.2.2

---

**PREC\_EXTR**

*Purpose:* Set numerical resolution

*Type:* REAL\*8

*Effect:* When finding bounce points or integrating along the field line, minimum step is  $\Delta\zeta = \text{PREC\_EXTR}$

*Default value:*  $10^{-7}$

*Misc.:* Extremely small numbers might get the code stuck in infinite loops

*Ref.:* §4.2

---

---

**PREC\_BINT**

*Purpose:* Set numerical resolution

*Type:* REAL\*8

*Effect:* Bounce-integrals are considered to be converged when the relative variation (of the worst-behaving one) is smaller than **PREC\_BINT**

*Default value:* 0.05

*Misc.:* -

*Ref.:* §4.2

---

---

**MAL**

*Purpose:* Set numerical resolution

*Type:* INTEGER

*Effect:* Number of points in the  $\alpha$  grid

*Default value:* 64

*Misc.:* Will be ignored if **PREC\_DQDV>0**

*Ref.:* §4.3

---

**MLAMBDA**

*Purpose:* Set numerical resolution  
*Type:* INTEGER  
*Effect:* Number of points in the  $\lambda$  grid  
*Default value:* 128  
*Misc.:* Will be ignored if **PREC\_DQDV>0**  
*Ref.:* §4.3

---

**PREC\_DQDV**

*Purpose:* Set numerical resolution  
*Type:* REAL\*8  
*Effect:* Monoenergetic calculations are considered to be converged when the relative variation (of the most representative of them) is smaller than **PREC\_DQDV**  
*Default value:* 0.05  
*Misc.:* -  
*Ref.:* §4.3

---

**PREC\_INTV**

*Purpose:* Set numerical resolution  
*Type:* REAL\*8  
*Effect:* I  
*Default value:* f  
*Misc.:* p  
*Ref.:* o

sitive, monoenergetic calculations for large values of  $v$  (and thus low collisionality and harder to converge) are skipped once their relative contribution to the velocity convolution

(in particular, to the transport coefficient proportional to the temperature gradient) is smaller than `PREC_INTV` -1 It is assumed that the size of this contribution decreases with  $v$ . Note that the error in the fluxes maybe (probably not much) larger than `PREC_INTV` §4.3

---

**NEFIELD**

*Purpose:* Set details of monoenergetic database  
*Type:* INTEGER  
*Effect:* `NEFIELD` values of  $E_r/v$  are calculated  
*Default value:* 9  
*Misc.:* Ignored if `.NOT.CALC_DB`. The default value is the maximum possible value (hardwired in the source code)  
*Ref.:* §11.1, appendix B

---

**EFIELD**

*Purpose:* Set details of monoenergetic database  
*Type:* REAL\*8  
*Effect:* Calculated values of  $E_r/v$  T)  
*Default value:* /0E-0,1E-5,3E-5,1E-4,3E-4,1E-3,3E-3,1E-2,3E-2/  
*Misc.:* Ignored if `.NOT.CALC_DB`  
*Ref.:* §11.1, appendix B

---

**NCMUL**

*Purpose:* Set details of monoenergetic database  
*Type:* INTEGER  
*Effect:* **NCMUL** values of  $\nu/v$  are calculated  
*Default value:* 18  
*Misc.:* Ignored if .NOT.**CALC\_DB**. The default value is the maximum possible value (hardwired in the source code)  
*Ref.:* §11.1, appendix B

---

**CMUL**

*Purpose:* Set details of monoenergetic database  
*Type:* REAL\*8  
*Effect:* Calculated values of  $\nu/v (m^{-1})$   
*Default value:* /3E+2,1E+2,3E+1,1E+1,3E+0,1E+0,3E-1,1E-1,3E-2,1E-2,3E-3,1E-3,3E-4,1E-4,3E-5,1E-5,3E-6,1E-6/  
*Misc.:* Ignored if .NOT.**CALC\_DB**  
*Ref.:* §11.1, appendix B

---

**NER**

*Purpose:* Set details of ambipolarity  
*Type:* INTEGER  
*Effect:* **NER** evaluations of the drift-kinetic equation in the  $E_r$  scan previous to bisection  
*Default value:* 21  
*Misc.:* Ignored if .NOT.**SOLVE\_AMB**  
*Ref.:*

---

**ERMIN**

*Purpose:* Set details of ambipolarity  
*Type:* REAL\*8  
*Effect:* Minimum value of  $E_r$  (kV/m) in the scan previous to bisection  
*Default value:* Twice the expected value, according to the input values of density and temperature, with adiabatic electrons and with ions in the  $1/\nu$  regime  
*Misc.:* Ignored if .NOT.[SOLVE\\_AMB](#)  
*Ref.:* e.g. [[Maaßberg et al., 1999](#)]

---

**ERMAX**

*Purpose:* Set details of ambipolarity  
*Type:* REAL\*8  
*Effect:* Maximum value of  $E_r$  (kV/m) in the scan previous to bisection  
*Default value:* Twice the expected value, according to the input values of density and temperature, with adiabatic ions and with electrons in the  $1/\nu$  regime  
*Misc.:* Ignored if .NOT.[SOLVE\\_AMB](#)  
*Ref.:* e.g. [[Maaßberg et al., 1999](#)]

---

**ERACC**

*Purpose:* Set details of ambipolarity  
*Type:* REAL\*8  
*Effect:* Accuracy in the calculation of  $E_r$  (kV/m)  
*Default value:* 0.1  
*Misc.:* Ignored if .NOT.[SOLVE\\_AMB](#)  
*Ref.:*

---

**NERR**

*Purpose:* Estimate error bars

*Type:* INTEGER

*Effect:* If larger than 1, **NERR** samples of the same calculation are done; otherwise, 1 calculation.

*Default value:* 0

*Misc.:* Should be larger than 10, typically 16 works fine

*Ref.:* §8.4

---

**IPERR**

*Purpose:* Estimate error bars

*Type:* REAL\*8

*Effect:* Input profiles  $q$  are left to vary in the interval  $(1 \pm \text{IPERR}) * q$

*Default value:* 0.2

*Misc.:* Ignored if **NERR**<1

*Ref.:* §8.4

### 7.3 The surfaces namelist

This namelist is contained in file `input.surfaces`, and it determines what flux-surfaces are computed.

---

**NS**

*Purpose:* Determine flux-surfaces

*Type:* INTEGER

*Effect:* **NS** flux-surfaces are calculated

*Default value:* 1

*Misc.:* Must be smaller than the number of surfaces contained in `boozmn.data` or `boozier.txt` ( $\sim 100$ ). Ignored if using magnetic field from `ddkes2.data`

*Ref.:*

---

**S**

*Purpose:* Determine flux-surfaces

*Type:* array of REAL\*8

*Effect:* Surfaces s(1) to s(**NS**) are determined

*Default value:* 1.0

*Misc.:* Ignored if using magnetic field from `ddkes2.data`

*Ref.:*

---

**DIRDB**

*Purpose:* Determine flux-surfaces

*Type:* array of CHARACTER\*100

*Effect:* The monoenergetic coefficients are read from directories `DIRDBDIRS(1)` to `DIRDBDIRS(NS)`

*Default value:* “.”/”

*Misc.:* Ignored if `REGB>-1` for all species

*Ref.:* Appendix B, §11.1, §11.2

---

**DIRS**

*Purpose:* Determine flux-surfaces

*Type:* array of CHARACTER\*7

*Effect:* The monoenergetic coefficients are read from directories **DIRDBDIRS(1)** to **DIRDBDIRS(NS)**

*Default value:* “.”/”

*Misc.:* Ignored if **REGB**>-1 for all species

*Ref.:* Appendix B, §11.1, §11.2

## 7.4 The species namelist

This namelist is contained in file **input.species**, and it determines what species are calculated and how. This is ignored if **ONLY\_DB** is set to .TRUE.. Species 1 must be electrons (even if you want them adiabatic) and 2 must be bulk ions, because this information is used later by KNOSOS, e.g., when calculating the transport of trace impurities.

---

**NBB**

*Purpose:* Determine species

*Type:* INTEGER

*Effect:* **NBB** species are included in the calculation

*Default value:* 2

*Misc.:* Must be larger than 1 and smaller than 12. The name “NB” was taken by the density of species b

*Ref.:* -

---

**ZB**

*Purpose:* Determine species

*Type:* REAL\*8

*Effect:* The charge number of species 1 to **NBB** is set

*Default value:* /-1.0, +1.0/

*Misc.:* Species 1 has to corresponds to electrons and 2 to bulk ions. Make sure you use a real number, not a integer number. The charge of the bulk ions is overwritten if **TASK3D**, with input from //input-prof.txt

*Ref.:* -

---

**AB**

*Purpose:* Determine species

*Type:* REAL\*8

*Effect:* The mass number of species 1 to **NBB** is set

*Default value:* / $5.4858 \times 10^{-4}$ , 1.00727/

*Misc.:* Species 1 has to corresponds to electrons and 2 to bulk ions. For the electrons, **AB** is the electron mass in amu. If you set **AB** value smaller than 1, electron mass is used (this means that you do not need to memorize it). The mass of the bulk ions is overwritten if **TASK3D**, with input from //input-prof.txt)

*Ref.:* -

---

## REGB

*Purpose:* Determine species

*Type:* INTEGER

*Effect:* The *regime* of species 1 to **NBB** is set:

- -2: adiabatic
- -1: from DKES database (complemented with KNOSOS if **TANG\_VM**)
- 0: several connected regimes (+1, +2 and +3, see below)
- +1: Pfirsch-Schlüter
- +2: plateau
- +3: low-collisionality ( $1/\nu$ ,  $\sqrt{\nu}$ , sb-p)
- +10: several connected trace impurity regimes (+11, +12 and +13, see below)
- +11: trace impurities in the Pfirsch-Schlüter regime
- +12: trace impurities in the plateau regime
- +13: trace impurities in the  $1/\nu$  regime

*Default value:* /-2, +3/

*Misc.:* Chapter 3 and appendices A and B

*Ref.:* For the calculation of the flux of trace impurities, bulk species are assumed to be in the  $1/\nu$ ,  $\sqrt{\nu}$  or sb-p regimes

---

**ZEFF**

*Purpose:* Determine species

*Type:* REAL\*8

*Effect:* Effective charge **ZEFF** is used to set impurity density (and to modify bulk ion density enforcing quasineutrality)

*Default value:* 1.0000001

*Misc.:* Ignored if **NBB**<3. Impurities have to be trace unless their **REGB** is -1.

*Ref.:* -

If **TASK3D** is set to .TRUE., file //input-prof.txt is read instead. At the end of the file (after the profile coefficients, see §8.2), there is a line with the following data:

B0 R0 a0 zi nmass a99 dfac tfac

with **ZB**=REAL(**zi**) and **AB**=REAL(**ai**)

# Chapter 8

## Plasma profiles

This chapter describes how the kinetic profiles are read and processed. This includes calculating thermal velocities, weights for the velocity integral, and normalization constants.

### 8.1 Workflow

The main loop is contained in file `plasmas.f90` (subroutine `READ_PLASMAS`), and it takes the following steps:

- Read electron density.
- Set the impurity density according to the effective charge (assuming 3 species).
  - It is checked whether impurities are really trace.
- Set the bulk ion density by imposing quasineutrality.
- Read the electron and ion temperatures.
  - Bulk ions and impurities have the same temperature.
- Read the electrostatic potential.
- For specific physics studies (if `JPP` or `SATAKE`), do some manipulations to the profiles.

Later, in subroutine `DKE_CONSTANTS`, velocity-dependent quantities are calculated: the source of the drift-kinetic equation, the thermal velocity, the collision frequency, the convolution weight, normalizations...

### 8.2 Kinetic profiles

The following kinetic profiles (`filename`) and their derivatives are read at every radial position `S`:

- Electron density: `ne`

- Electron temperature: `te`
- Ion temperature: `ti`
- Electrostatic potential: `ph`

The electron temperature is optional, and  $T_e = T_i$  if it is not provided. The electrostatic potential is optional as well; if additionally `SOLVE_AMB` is set to `.FALSE.`, the radial electric field is taken to be the ion root value, according to the input density and temperature, for ions in the  $1/\nu$  regime, see `TRIVIAL_AMB`.

The reading is done in subroutine `READ_PROFILES`, and there are several kind of files (note that the units are different in each case, they are transformed internally to the units used by the code!):

- `//input-prof.txt`

This file contains profiles in the format used by `TASK3D`.

- Line #2: coefficients of  $n_e$  ( $10^{19} \text{ m}^{-3}$ ).
- Line #4: coefficients of  $T_i$  (keV).
- Line #6: coefficients of  $T_e$  (keV).

The values of the quantities and their radial derivatives are calculated analitically, using expressions such as  $q = \sum_{0 \leq n \leq 10} q_n \rho^n$ , with  $\rho = \sqrt{s}$ . The bulk density is taken from quasineutrality (no more than two species are allowed for the moment in this type of calculation).

- `//prof-file.txt`

This file contains profiles in the format used by `TASK3D` (if you are using `KNOSOS` from `TASK3D`, this is the file that is read).

- Column #1:  $\rho = \sqrt{s} = \sqrt{\psi/\psi_{LCMS}}$ .
- Column #2: quantity  $n_e$  ( $\text{m}^{-3}$ ).
- Column #3: quantity  $T_e$  (keV).
- Column #4: quantity  $T_i$  (keV).

The radial derivatives  $\partial_\psi q$  are then calculated at every radial position with second-order accuracy, and both  $q$  and  $\partial_\psi q$  are Lagrange-interpolated at the desired radial position. The bulk density is taken from quasineutrality (no more than two species are allowed for the moment in this type of calculation).

- `//profiles.txt`

This file contains profiles in the format used by `NE02`.

- Column #1:  $s = \psi/\psi_{LCMS}$ .
- Column #2: quantity  $n_i$  ( $\text{m}^{-3}$ ).

- Column #3: quantity  $n_e$  ( $\text{m}^{-3}$ ).
- Column #4: quantity  $T_i$  (eV).
- Column #5: quantity  $T_e$  (eV).
- Column #6: quantity  $-\partial_{\psi_T}\varphi/\text{iota}$  (rad/s).

The radial derivatives  $\partial_\psi q$  are then calculated at every radial position with second-order accuracy, and both  $q$  and  $\partial_\psi q$  are Lagrange-interpolated at the desired radial position.

- **//profiles\_DR.txt**

This file contains profiles in the format provided by the Doppler Reflectometry team at W7-X.

- Column #1:  $\rho = \sqrt{s} = \sqrt{\psi/\psi_{LCMS}}$ .
- Column #2: quantity  $n_e$  ( $10^{19} \text{ m}^{-3}$ ).
- Column #3: quantity  $T_e$  (keV).
- Column #4: quantity  $T_i$  (keV).

The radial derivatives  $\partial_\psi q$  are then calculated at every radial position with second-order accuracy, and both  $q$  and  $\partial_\psi q$  are Lagrange-interpolated at the desired radial position.

- **//profiles\_neotransp.dat**

This file contains profiles in the format used by **neotransp**.

- Column #1:  $r = a\rho = a\sqrt{s} = a\sqrt{\psi/\psi_{LCMS}}$ .
- Column #2: quantity  $n_e$  ( $10^{19} \text{ m}^{-3}$  or  $10^{20} \text{ m}^{-3}$ ).
- Column #3: quantity  $T_e$  (keV or eV).
- Column #4: quantity  $T_i$  (keV or eV).

In the header, the density columns must be marked **n\_20m3\_X** or **n\_19m3\_X** and the temperature columns **T\_keV\_X** or **T\_eV\_X**, where X is a recognised species (e, H, D...). The radial derivatives  $\partial_\psi q$  are then calculated at every radial position with second-order accuracy, and both  $q$  and  $\partial_\psi q$  are Lagrange-interpolated at the desired radial position.

- **//profiles.d**

This file contains profiles in the format used by **EUTERPE** and **stella**.

- Column #1:  $s = \psi/\psi_{LCMS}$ .
- Column #2: quantity  $\partial_s \log T_i$ .
- Column #3: quantity  $T_i$  (eV).
- Column #4: quantity  $\partial_s \log T_e$ .
- Column #5: quantity  $T_e$  (eV).

- ...
- Column # $2\text{NBB}+4$ : quantity  $\partial_s \log n_e$ .
- Column # $2\text{NBB}+5$ : quantity  $n_e$  ( $\text{m}^{-3}$ ).

Both  $q$  and  $\partial_\psi q$  are Lagrange-interpolated at the desired radial position. The bulk density is taken from quasineutrality (impurity density is taken from **ZEFF** and  $T_Z = T_i$ ).

- **//er\_s.dat**

This file contains the radial electric field in the format used by EUTERPE.

- Column #1:  $s = \psi/\psi_{LCMS}$ .
- Column #2:  $E_r$  (V/m).

$E_r$  is Lagrange-interpolated at the desired radial position.

- **//filename//prof\_r.d** (e.g. **neprof\_r.d**)

This file contains profiles in the format used by CIEMAT routines' **neprof** [van Miligen et al., 2011] and **teprof** (after one header line, the number of meaningful points is usually 100, and should be smaller than 200).

- Column #1:  $\rho = \sqrt{s} = \sqrt{\psi/\psi_{LCMS}}$ .
- Column #3: quantity  $q$ .
- Column #5: error in  $q$ .
- Column #6:  $\partial_\rho q$  (except for **ph**, that contains  $E_r = -\partial_r \varphi_0$ ).
- Column #7: error in  $\partial_\rho q$ .

Both  $q$  and  $\partial_\psi q$  are Lagrange-interpolated at the desired radial position.

- **//filename//\_in.d** (e.g. **ne\_in.d**)

The quantities are given just at the desired radial position (after one header line).

- Column #1:  $q$
- Column #2:  $\partial_r \log q$ .

If  $T_e$  is not provided,  $T_e = T_i$  is set. If **SOLVE\_AMB** is set to **.TRUE.**, the **ph** files are ignored.

### 8.3 Scan in the plasma parameters

The **model** namelist allows to modify the kinetic profiles in order to perform an scan (in different runs of KNOSOS):

- **FNE**: the density (keeping the normalized radial derivative constant).
- **FTE**: the electron temperature (keeping the normalized radial derivative constant).

- **FTI**: the ion temperature (keeping the normalized radial derivative constant).
- **FDLNE**: the normalized radial derivative of the density (keeping the density constant).
- **FDLTE**: the normalized radial derivative of the electron temperature (keeping electron temperature constant).
- **FDLTI**: the normalized radial derivative of the ion temperature (keeping the ion temperature constant).
- **FER**: the radial electric field.

This is the complete list of changes in all the relevant variables (where the hats correspond to the old values and \* denotes multiplication, in Fortran style):

$$\begin{aligned}
 n_e &= \hat{n}_e * \text{FNE}, \\
 T_e &= \hat{T}_e * \text{FTE}, \\
 T_i &= \hat{T}_i * \text{FTI}, \\
 \partial_\psi n_e &= \partial_\psi \hat{n}_e * \text{FNE} * \text{FDLNE}, \\
 \partial_\psi T_e &= \partial_\psi \hat{T}_e * \text{FTE} * \text{FDLTE}, \\
 \partial_\psi T_i &= \partial_\psi \hat{T}_i * \text{FTI} * \text{FDLTI}, \\
 E_r &= \hat{E}_r * \text{FER}.
 \end{aligned} \tag{8.1}$$

## 8.4 Error estimates

**KNOSOS** can provide results with error bars caused by uncertainties in the input quantities (densities and temperatures). It does so by using a Monte Carlo procedure: the same calculation is done **NERR** times, each time with a different set of input profiles. These are determined by means of a Gaussian random number generator according to their mean values and error bars, as e.g. in [Velasco et al. \[2011\]](#). If no error was read from the inputs (see §8.2), the value of **IPERR** is used.

# Chapter 9

## Magnetic configuration

This chapter describes how the magnetic geometry is read and how it is processed.

### 9.1 Workflow

The main loop is contained in file `configuration.f90` (subroutine `read_BFIELD(s0)`), and it takes the following steps:

- Read the input files.
  - Read the quantities at `s0` and (if available) neighbour surfaces.
- Calculate missing quantities (e.g. due to different definitions of different possible inputs).
- Keep the largest `TRUNCATE_B` modes of the Fourier spectra of  $B$ .
- Add an extra magnetic field  $B_1$  to the previously read  $B_0$  \*.
- Change from a left-handed to a right-handed coordinate system. See §9.4.
- For specific physics studies (if `JPP` or `SATAKE` are true), do some manipulations to the magnetic configuration.
- Calculate some radial derivatives.
- Copy information to arrays with only one index.
- Calculate several other flux-surface quantities.
- Set, according to the required precision `PREC_EXTR`, step size along the Boozer angles, etc.
- Plot map of the magnetic field on the flux surface.

## 9.2 Input magnetic field

The magnetic configuration, which does not need to be stellarator-symmetric, can be read from three different kind of files:

- `boozmn.data`

This unformatted file is produced by `BOOZER_XFORM`. It contains information of several flux-surfaces, and `READ_BFIELD` reads and interpolates the information of the two closest surfaces to `s0`. If you are using `KNOSOS` from `TASK3D`, this is the file that is read.

- `boozier.txt`

This text file is produced by `COTRANS` (IPP). It contains basically the same information than `boozmn.data` (although units and definitions may slightly differ).

- `ddkes2.data`

This text file is produced by `DKES`, in routine `dkes_input_prepare`, and it contains a namelist with information of a single flux-surface. In case radial derivatives are needed, the major and local minor radius  $R$  and  $a$  (note that  $s = 1$  so  $r = a$ ) are calculated using expressions valid for large-aspect ratio, or they can be read from namelist `radius`. It is included in file `input.radius` and it contains:

`R`

*Purpose:* Set radius

*Type:* `REAL*8`

*Effect:* Major radius in meters

*Default value:*  $B_\zeta/B_{00}$

*Misc.:* §9.3

*Ref.:*

a

*Purpose:* Set radius  
*Type:* REAL\*8  
*Effect:* Minor radius in meters  
*Default value:*  $\partial_{\hat{r}}\psi/B_{00}$ , with  $\hat{r}$  the DKES radial coordinate  
*Misc.:*  $s = 1$ , so  $r = a$   
*Ref.:* §9.3

- **add\_ddkes2.data**

This text file has a similar format than `ddkes2.data`, and it contains a namelist with additional modes of the magnetic field. If `USE_B0pB1` or `USE_B1`, these modes go to  $B_1$ , and the modes read before go to  $B_0$ .

Different inputs include different quantities, e.g. the radial derivatives of the toroidal and poloidal flux instead of the rotational transform, or use different normalization), so some processing is done in subroutine `READ_BFIELD` after reading.

### 9.3 Some useful quantities in Boozer coordinates

In Boozer coordinates  $(\psi, \theta, \zeta)$ , the magnetic field can be expressed in its covariant representation

$$\mathbf{B} = B_\psi \nabla \psi + B_\theta \nabla \theta + B_\zeta \nabla \zeta = B_\theta \nabla \theta + B_\zeta \nabla \zeta, \quad (9.1)$$

where  $B_\psi = 0$  for low  $\beta$ . VMEC\* provides  $B_\zeta = \frac{I_p}{2\pi}$ , where  $I_p$  is the poloidal current, and  $B_\theta = \frac{I_t}{2\pi}$ , where  $I_t$  is the toroidal current. The contravariant representation of  $\mathbf{B}$ , in terms of the radial derivatives of the toroidal and poloidal fluxes, is simply

$$\mathbf{B} = \frac{\Psi'_t}{\sqrt{g}} (\iota \mathbf{e}_\theta + \mathbf{e}_\zeta), \quad (9.2)$$

where  $2\pi\iota$  is the rotational transform. VMEC provides  $\iota$  or  $\partial_{\hat{r}}\Psi_t$  and  $\partial_{\hat{r}}\Psi_p$ , where  $\Psi_p$  is the poloidal flux and  $\hat{r}$  the DKES radial coordinate, and  $\iota = \partial_r\Psi_p/\partial_r\Psi_t$ .

The Jacobian of the magnetic coordinate system  $\sqrt{g}$  can be calculated in terms of known quantities by multiplying the covariant and contravariant representations of the magnetic field:

$$\sqrt{g} = \Psi'_t \frac{B_\theta \iota + B_\zeta}{B^2} = \frac{|B_\theta \iota + B_\zeta|}{B^2}. \quad (9.3)$$

---

\*With VMEC, we will refer to VMEC [Hirshman and Whitson, 1983] and additional codes (such as `BOOZER_XFORM` [Sanchez et al., 2000] or `COTRANS`), that write the equilibrium in Boozer coordinates.

since we have set  $\psi = |\Psi_t|$ , being  $2\pi\Psi_t$  the toroidal flux, and  $\sqrt{g}$  is defined positive in a right-handed coordinate system.

We have seen that we are interested in the set of spatial coordinates  $(\psi, \alpha, l)$ , where  $\alpha$  is an angular coordinate that labels a magnetic field line and  $l$  is the arc length over the magnetic field line. The magnetic field can then be written

$$\mathbf{B} = \nabla\psi \times \nabla\alpha. \quad (9.4)$$

The parallel derivative (i.e., the derivative along the magnetic field lines) can be written

$$\begin{aligned} \frac{\mathbf{B}}{B} \cdot \nabla &= \frac{\Psi'_t}{B\sqrt{g}} \left[ (\iota\mathbf{e}_\theta + \mathbf{e}_\zeta) \cdot \left( \frac{\partial}{\partial s} \nabla s + \frac{\partial}{\partial\theta} \nabla\theta + \frac{\partial}{\partial\zeta} \nabla\zeta \right) \right] \\ &= \frac{\Psi'_t}{B\sqrt{g}} \left( \iota \frac{\partial}{\partial\theta} + \frac{\partial}{\partial\zeta} \right) = \frac{B}{\iota B_\theta + B_\zeta} \left( \iota \frac{\partial}{\partial\theta} + \frac{\partial}{\partial\zeta} \right), \end{aligned} \quad (9.5)$$

and the unit element along the magnetic field line is

$$dl = \frac{\iota B_\theta + B_\zeta}{B} d\zeta. \quad (9.6)$$

We will also use the first and second derivative of the magnetic field strength along the magnetic field line:

$$\begin{aligned} \frac{\partial B}{\partial l} &= \frac{B}{\iota B_\theta + B_\zeta} \left( \iota \frac{\partial B}{\partial\theta} + \frac{\partial B}{\partial\zeta} \right), \\ \frac{\partial^2 B}{\partial l^2} &= \frac{B^2}{(\iota B_\theta + B_\zeta)^2} \left[ \left( \iota^2 \frac{\partial^2 B}{\partial\theta^2} + \frac{\partial^2 B}{\partial\zeta^2} + 2\iota \frac{\partial^2 B}{\partial\zeta\partial\theta} \right) \right] + \\ &\quad + \frac{B}{(\iota B_\theta + B_\zeta)^2} \left[ \iota^2 \left( \frac{\partial B}{\partial\theta} \right)^2 + \left( \frac{\partial B}{\partial\zeta} \right)^2 + 2\iota \left( \frac{\partial B}{\partial\theta} \frac{\partial B}{\partial\zeta} \right) \right]. \end{aligned} \quad (9.7)$$

The magnetic drift  $\mathbf{v}_M$  in low- $\beta$  approximation is:

$$\mathbf{v}_M = \frac{mv^2}{2Ze} (1 + p^2) \frac{\mathbf{B} \times \nabla B}{B^3} = v_d \frac{1 + p^2}{2} \frac{\mathbf{B} \times \nabla B}{B^3}, \quad (9.8)$$

where  $p$  is the pitch-angle variable and we defined  $v_d \equiv mv^2/Ze$ . In our coordinate system the magnetic drift reads

$$\begin{aligned} \mathbf{v}_M &= v_d \frac{1 + p^2}{2} \frac{1}{B^3} (B_\theta \nabla\theta + B_\zeta \nabla\zeta) \times \left( \frac{\partial B}{\partial\psi} \nabla\psi + \frac{\partial B}{\partial\theta} \nabla\theta + \frac{\partial B}{\partial\zeta} \nabla\zeta \right) = \\ &= v_d \frac{1 + p^2}{2} \frac{1}{B^3 \sqrt{g}} \left[ \frac{\partial B}{\partial\psi} (B_\zeta \mathbf{e}_\theta - B_\theta \mathbf{e}_\zeta) + \left( B_\theta \frac{\partial B}{\partial\zeta} - B_\zeta \frac{\partial B}{\partial\theta} \right) \mathbf{e}_\psi \right]. \end{aligned} \quad (9.9)$$

The VMEC equilibrium contains all the information required for calculating the derivatives of  $B$ : the Fourier decomposition of  $B(\theta, \zeta)$  at several radial positions. The radial component of the magnetic drift is

$$\mathbf{v}_M \cdot \nabla\psi = v_d \frac{1 + p^2}{2} \frac{1}{B^3 \sqrt{g}} \left( B_\theta \frac{\partial B}{\partial\zeta} - B_\zeta \frac{\partial B}{\partial\theta} \right), \quad (9.10)$$

and, since we define<sup>†</sup>  $\alpha = \theta - \iota\zeta$ , so that

$$\nabla\alpha = \nabla\theta - \iota\nabla\zeta - \frac{\partial\iota}{\partial\psi}\zeta\nabla\psi, \quad (9.11)$$

the tangential component of the magnetic drift is

$$\mathbf{v}_M \cdot \nabla\alpha = v_d \frac{1+p^2}{2} \frac{1}{B^3\sqrt{g}} \left[ \frac{\partial B}{\partial\psi} (B_\zeta + \iota B_\theta) - \left( B_\theta \frac{\partial B}{\partial\zeta} - B_\zeta \frac{\partial B}{\partial\theta} \right) \frac{\partial\iota}{\partial\psi} \zeta \right] = \quad (9.12)$$

$$= v_d \frac{1+p^2}{2B} \left[ \Psi'_t \frac{\partial B}{\partial\psi} - \frac{1}{|B_\zeta + \iota B_\theta|} \left( B_\theta \frac{\partial B}{\partial\zeta} - B_\zeta \frac{\partial B}{\partial\theta} \right) \frac{\partial\iota}{\partial\psi} \zeta \right]. \quad (9.13)$$

We note that we have been able to keep the effect of the magnetic shear  $\partial_\psi\iota$ .

The  $\mathbf{E} \times \mathbf{B}$  drift, caused by  $\varphi = \varphi_0(\psi) + \varphi_1(\psi, \theta, \zeta)$  with  $\varphi_1 \ll \varphi_0$ , can be written

$$\begin{aligned} \mathbf{v}_E &= \frac{1}{B^2} (\mathbf{E} \times \mathbf{B}) = \frac{1}{B^2} (B_\theta \nabla\theta + B_\zeta \nabla\zeta) \times \left( \frac{\partial\varphi}{\partial\psi} \nabla\psi + \frac{\partial\varphi}{\partial\theta} \nabla\theta + \frac{\partial\varphi}{\partial\zeta} \nabla\zeta \right) = \\ &= \frac{1}{|B_\zeta + \iota B_\theta|} \left[ \frac{\partial\varphi_0}{\partial\psi} (B_\zeta \mathbf{e}_\theta - B_\theta \mathbf{e}_\zeta) + \left( B_\theta \frac{\partial\varphi_1}{\partial\zeta} - B_\zeta \frac{\partial\varphi_1}{\partial\theta} \right) \mathbf{e}_\psi \right]. \end{aligned} \quad (9.14)$$

Its radial component is

$$\mathbf{v}_E \cdot \nabla\psi = \frac{1}{|B_\zeta + \iota B_\theta|} \left( B_\theta \frac{\partial\varphi_1}{\partial\zeta} - B_\zeta \frac{\partial\varphi_1}{\partial\theta} \right), \quad (9.15)$$

and its tangential component is:

$$\mathbf{v}_E \cdot \nabla\alpha = \frac{B_\zeta + \iota B_\theta}{|B_\zeta + \iota B_\theta|} \frac{\partial\varphi_0}{\partial\psi} = \Psi'_t \frac{\partial\varphi_0}{\partial\psi}. \quad (9.16)$$

In the incompressible limit (that used by DKES), equation (9.16) is simplified to

$$\mathbf{v}_E \cdot \nabla\alpha = \Psi'_t \frac{B^2}{\langle B^2 \rangle} \frac{\partial\varphi_0}{\partial\psi}. \quad (9.17)$$

## 9.4 From VMEC left-handed coordinates to standard right-handed coordinates

VMEC provides the following quantities for every flux surface:  $B_\zeta, B_\theta, \Psi_t, \iota, B_{mn}, R_{mn}, Z_{mn}$ ,

---

<sup>†</sup>Other definitions are possible, differing only by a constant factor.

$\Phi_{mn}$ , where the expressions

$$\begin{aligned}
 B(\psi, \theta, \zeta) &= \sum_{m,n} B_{mn}^{(c)} \cos(m\theta - nN_p\zeta), \\
 &+ \sum_{m,n} B_{mn}^{(s)} \sin(m\theta - nN_p\zeta), \\
 R(\psi, \theta, \zeta) &= \sum_{m,n} R_{mn}^{(c)} \cos(m\theta - nN_p\zeta), \\
 &+ \sum_{m,n} R_{mn}^{(s)} \sin(m\theta - nN_p\zeta), \\
 \Phi(\psi, \theta, \zeta) &= \sum_{m,n} \Phi_{mn}^{(c)} \cos(m\theta - nN_p\zeta), \\
 &+ \sum_{m,n} \Phi_{mn}^{(s)} \sin(m\theta - nN_p\zeta), \\
 Z(\psi, \theta, \zeta) &= \sum_{m,n} Z_{mn}^{(c)} \cos(m\theta - nN_p\zeta), \\
 &+ \sum_{m,n} Z_{mn}^{(s)} \sin(m\theta - nN_p\zeta),
 \end{aligned} \tag{9.18}$$

provide the position in cylindrical coordinates of a point  $(\psi, \theta, \zeta)$ , and the value of the magnetic field.  $N_p$  is the number of field periods. We also have, as usual:

$$\begin{aligned}
 \mathbf{B} &= B_\theta \nabla \theta + B_\zeta \nabla \zeta, \\
 \mathbf{B} &= \frac{\Psi'_t}{\sqrt{g}} (\iota \mathbf{e}_\theta + \mathbf{e}_\zeta), \\
 \sqrt{g} &= \frac{B_\theta \iota + B_\zeta}{B^2}.
 \end{aligned} \tag{9.19}$$

In a left-handed system such as that of VMEC we have

$$\begin{aligned}
 \mathbf{e}_\psi &= -\sqrt{g} (\nabla \theta \times \nabla \zeta), \\
 \nabla \psi &= \frac{-\Psi'_t}{\sqrt{g}} (\mathbf{e}_\theta \times \mathbf{e}_\zeta).
 \end{aligned} \tag{9.20}$$

We prefer to work in a right-handed coordinate system  $(\psi, \tilde{\theta}, \zeta)$ , with  $\tilde{\theta} = -\theta$ , so that

$$\begin{aligned}
 \mathbf{e}_\psi &= \sqrt{g} (\nabla \tilde{\theta} \times \nabla \zeta), \\
 \nabla \psi &= \frac{\Psi'_t}{\sqrt{g}} (\mathbf{e}_{\tilde{\theta}} \times \mathbf{e}_\zeta).
 \end{aligned}$$

We then can now write

$$\begin{aligned}
 B(\psi, \tilde{\theta}, \zeta) &= \sum_{m,n} B_{mn}^{(c)} \cos(m\theta + nN_p\zeta) \\
 &\quad + \sum_{m,n} \tilde{B}_{mn}^{(s)} \sin(m\theta + nN_p\zeta), \\
 R(\psi, \tilde{\theta}, \zeta) &= \sum_{m,n} R_{mn}^{(c)} \cos(m\theta + nN_p\zeta) \\
 &\quad + \sum_{m,n} \tilde{R}_{mn}^{(s)} \sin(m\theta + nN_p\zeta), \\
 \Phi(\psi, \tilde{\theta}, \zeta) &= \sum_{m,n} \Phi_{mn}^{(c)} \cos(m\theta + nN_p\zeta) \\
 &\quad + \sum_{m,n} \tilde{\Phi}_{mn}^{(s)} \sin(m\theta + nN_p\zeta), \\
 Z(\psi, \tilde{\theta}, \zeta) &= \sum_{m,n} Z_{mn}^{(c)} \cos(m\theta + nN_p\zeta) \\
 &\quad + \sum_{m,n} \tilde{Z}_{mn}^{(s)} \sin(m\theta + nN_p\zeta),
 \end{aligned} \tag{9.21}$$

and

$$\begin{aligned}
 \mathbf{B} &= B_{\tilde{\theta}} \nabla \tilde{\theta} + B_{\zeta} \nabla \zeta, \\
 \mathbf{B} &= \frac{\Psi'_t}{\sqrt{g}} (\tilde{\iota} \mathbf{e}_{\tilde{\theta}} + \mathbf{e}_{\zeta}),
 \end{aligned} \tag{9.22}$$

with

$$\begin{aligned}
 \mathbf{e}_{\tilde{\theta}} &= -\mathbf{e}_{\theta}, \\
 B_{\tilde{\theta}} &= -B_{\theta}, \\
 \tilde{\iota} &= -\iota, \\
 \tilde{B}_{mn}^{(s)} &= -B_{mn}^{(s)}, \\
 \tilde{R}_{mn}^{(s)} &= -R_{mn}^{(s)}, \\
 \tilde{\Phi}_{mn}^{(s)} &= -\Phi_{mn}^{(s)}, \\
 \tilde{Z}_{mn}^{(s)} &= -Z_{mn}^{(s)}.
 \end{aligned} \tag{9.23}$$

Since the radial coordinate  $\psi = \Psi_t$  does not change, we have  $\tilde{\Psi}_p = -\Psi_p$  as well.

**KNOSOS** works in the right-handed coordinate system, and all along this document we drop the tilde  $\tilde{\cdot}$ .

## 9.5 Relation between Fourier expansions

In some cases, we are going to deal (e.g. when performing fast-Fourier transforms) with Fourier expansions such as<sup>†</sup>

$$B(\theta, \zeta) = \sum_{-\infty < n < \infty} \sum_{-\infty < m < \infty} B_{mn} \exp [i(m\theta + nN_p\zeta)], \quad (9.24)$$

but the information of the magnetic field is given by VMEC (after changing to a right-handed coordinate system, see §9.4) as a summatory of cosines with  $m \geq 0$ :

$$\begin{aligned} B(\theta, \zeta) &= \sum_{-\infty < n < \infty} \sum_{0 \leq m < \infty} \beta_{mn}^{(c)} \cos (m\theta + nN_p\zeta) \\ &+ \sum_{-\infty < n < \infty} \sum_{0 \leq m < \infty} \beta_{mn}^{(s)} \sin (m\theta + nN_p\zeta). \end{aligned} \quad (9.25)$$

It is easy to show that the relation between  $B_{mn}$  and  $\beta_{mn}$  is:

$$\begin{aligned} B_{mn} &= \frac{1}{2} (\beta_{mn}^{(c)} + i\beta_{mn}^{(s)}) \text{ if } m > 0, \\ B_{0n} &= \frac{1}{2} (\beta_{0n}^{(c)} + \beta_{0,-n}^{(c)} + i\beta_{0n}^{(s)} + i\beta_{0,-n}^{(s)}), \\ B_{mn} &= \frac{1}{2} (\beta_{-m,-n}^{(c)} + i\beta_{-m,-n}^{(s)}) \text{ if } m < 0. \end{aligned} \quad (9.26)$$

## 9.6 Scan in the magnetic configuration parameters

The `model` namelist allows to modify the magnetic configuration in order to perform an scan (in different runs of `KNOSOS`) in several 0-D parameters:

- **FI**: the rotational transform (keeping the shear constant).
- **FS**: the magnetic shear (keeping the rotational transform constant).
- **FP**: the number of field periods (keeping the rotational transform constant).
- **FE**: the inverse aspect ratio (keeping the major radius constant).
- **FR**: the size of the device (keeping the aspect ratio and magnetic field strength constant).
- **FB**: the magnetic field strength (keeping the size of the device constant).

As we have already advanced, scanning in a parameter of the configuration requires that we take a decision on which parameters are kept constant and which ones change accordingly during the scan. This is automatically done by `KNOSOS`, and this is the complete list of

---

<sup>†</sup>The expressions in this section are valid for stellarator-symmetric equilibria, but can be straightforwardly generalized.

changes in all the relevant variables (where the hats correspond to the old values and \* denotes multiplication, in Fortran style):

$$\begin{aligned}
 N_p &= \hat{N}_p * \text{FP}, \\
 s &= \hat{s} * \text{FS}, \\
 \iota &= \hat{\iota} * \text{FI}, \\
 \Psi'_p &= \hat{\Psi}'_p * \text{FI} * \text{FB} * \text{FE} * \text{FR}, \\
 \Psi'_t &= \hat{\Psi}'_t * \text{FB} * \text{FE} * \text{FR}, \\
 \partial_\psi &= \hat{\partial}_\psi / (\text{FB} * \text{FE} * \text{FE} * \text{FR} * \text{FR}), \\
 B_\theta &= \hat{B}_\theta * \text{FB} * \text{FR}, \\
 B_\zeta &= \hat{B}_\zeta * \text{FB} * \text{FR}, \\
 R &= \hat{R} * \text{FR}, \\
 a &= \hat{a} * \text{FE} * \text{FR}, \\
 B_{0,0} &= \hat{B}_{0,0} * \text{FB}, \\
 B_{m,n} &= \hat{B}_{m,n} * \text{FB} * \text{FE}, \text{ if } m \neq 0 \text{ or } n \neq 0. \tag{9.27}
 \end{aligned}$$

# Chapter 10

## Output parameters

In this chapter, we list the output files of the code and their content. Generally speaking, the name of the file (e.g. `flux.amb`) indicates the quantities contained (e.g. particle and energy fluxes), and the extension of the file indicates the kind of data contained (e.g. dependence on  $E_r$ ). Additionally:

- If `COMPARE_MODELS` is set to `.TRUE.`, several files are produced calculated as determined by the `model` namelist, but also with additional simplifications). If this is the case, an extension `.comp` is added (e.g. `flux.amb.comp`) and a first column with an integer that indicates the model (instead of the radial flux-surface):
  - 01: Without tangential magnetic drift, not solving quasineutrality.
  - 02: With tangential magnetic drift, not solving quasineutrality.
  - 11: Without tangential magnetic drift, solving quasineutrality.
  - 12: With tangential magnetic drift, solving quasineutrality.
  - 21: Without tangential magnetic drift, solving quasineutrality, all kinetic.
  - 22: With tangential magnetic drift, solving quasineutrality, all kinetic.

(e.g., if `TANG_VM` is set to `.TRUE.`, and quasineutrality is solved with adiabatic electrons, cases 12 and 02 are plotted).

- In parallel runs, several processes may produce the same output file for, e.g., different flux-surfaces or profile samples. If this is the case, an extension is added with the rank number (e.g. `varphi1.map.comp.08`).

### 10.1 Standard output and standard error, warnings

Files `STDOUT` and `STDERR` contain the standard output and error respectively. The amount of information shown is larger if flags `DEBUG` and/or `TIME` are set to `.TRUE..` File `STDERR` also contains warnings (e.g., if you are calculating the flux in the plateau regime but your species are collisionless).

## 10.2 B.map

KNOSOS reads the Fourier modes of the magnetic field in Boozer left-handed coordinates and changes it to a right-handed system (see chapter 9). File `B.map`, contains bidimensional maps of  $B(\zeta, \theta)$  and of the radial magnetic drift for one value of  $\lambda$ . The first line lists all the variables, one per column:

```
s \zeta_{Boozer} \theta_{Boozer}(right-handed) B[T] (v_B.\nabla\psi)[A.U.]
```

Note that the radial magnetic drift has the right sign and it is normalized to be comparable to the map of the  $\mathbf{E} \times \mathbf{B}$  radial drift of `varphi1.map` for protons.

## 10.3 results.knosos: monoenergetic transport coefficients

If `CALC_DB` is set to `.TRUE.`, KNOSOS performs monoenergetic calculations for a set of values of `CMUL` and `EFIELD`, either predetermined (see §B.1) or input in `parameters` namelist (via `NEFIELD`, `EFIELD`, `NCMUL` and `CMUL`). These results can be directly compared with those of DKES (see §11.1). The results should be the same in all cases only if `INC_EXB` is true, see Beidler et al. [2007]. File `results.knosos`, similarly to `results.data`, contains one or several lines, corresponding to different values of `CMUL` (first column) and `EFIELD` (second column). The first line lists all the variables, one per column:

```
cmul efield weov wtov L11m L11p L31m L31p L33m L33p scal11 scal13 scal33
max_residual chip psip btheta bzeta vp
```

The result of such KNOSOS calculation (defined explicitly in equation B.3) is written in columns 5 and 6 (same value, so no error estimate is provided), and the rest of the columns, not used for the moment, contain `NaN`.

## 10.4 knosos.dk

If `NEOTRANSP` is set to `.TRUE.`, KNOSOS writes in `knoosos.dk` the same monoenergetic coefficients than `results.knosos` in a format compatible with `neotransp`.

## 10.5 varphi1.map

If `SOLVE_QN` or `TRIVIAL_QN` is set to `.TRUE.`, KNOSOS solves some version of the quasineutrality equation (see §4.5). File `varphi1.map` contains bidimensional maps of  $\varphi_1(\zeta, \theta)$ , the variation of the species density on the flux-surface (with the adiabatic component removed, but it can be estimated from the other columns), and the  $\mathbf{E} \times \mathbf{B}$  radial drift. The first line lists all the variables, one per column:

```
s \zeta_{Boozer} \theta_{Boozer}(right-handed) \varphi_1[V] e\varphi_1/T_i
(v_E.\nabla\psi)[A.U.] n_{e1}/n_{e0} n_{i1}/n_{i0}
```

Note that the radial  $\mathbf{E} \times \mathbf{B}$  drift has the right sign and it is normalized to be comparable to the map of the radial magnetic drift of `B.map` for protons.

## 10.6 varphi1.modes

If `SOLVE_QN` or `TRIVIAL_QN` are set to `.TRUE.`, KNOSOS solves some version of the quasineutrality equation (see §4.5). File `varphi1.modes`, contains the Fourier decomposition of the maps  $\varphi_1(\zeta, \theta)$  of file `varphi1.map`. The first line lists all the variables, one per column:

```
s cosine(0)/sine(1) n m \varphi_{nm}
```

Cosines are indicated by a "0" in the second column, while sines are indicated by a "1".

## 10.7 flux.amb

If `SOLVE_AMB` is set to `.TRUE.`, KNOSOS solves the ambipolarity equation. File `flux.amb`, contains flux-related quantities as a function of  $E_r$ . The first line lists all the variables, one per column:

```
s E_r[V/m] (\Gamma_b/n_b[m/s] Q_b/n_b/T_b[m/s] L_1^b[m^2/s] L_2^b[m^2/s] n_b[10^{19}m^{-3}] dlnn_b/dr T_b[eV] dlnT_b/dr Z_b , b=1,NBB), size(e\varphi_1/T_i)
```

Note that the number of columns varies, depending on the number of species `NBB`.

## 10.8 knososTASK3D.flux

If `TASK3D` is set to `.TRUE.`, KNOSOS writes in `knososTASK3D.flux` flux-related quantities as a function of  $E_r$  (some of them already contained in file `flux.amb`) in a format compatible with `TASK3D`.

## 10.9 flux.modes

If `SOLVE_QN` is set to `.TRUE.`, KNOSOS solves the quasineutrality equation and calculates the radial fluxes accordingly. Since the radial  $\mathbf{E} \times \mathbf{B}$  drift is only a source in the drift-kinetic equation, the fluxes depend quadratically,  $\sim [(\mathbf{v}_M + \mathbf{v}_E) \cdot \nabla \psi]^2$ , on  $\varphi_1$ . This typically gives a leading contribution from the radial magnetic drift, and then smaller terms with linear and quadratic dependence on  $\varphi_1$ . It is thus easy to calculate the contribution to radial transport of each mode of the Fourier decomposition of  $\varphi_1(\theta, \zeta)$ . The first line lists all the variables, one per column:

```
s E_r[V/m] cosine(0)/sine(1) n m (\Gamma_b/n_b[m/s] Q_b/n_b/T_b[m/s] L_1^b[m^2/s] L_2^b[m^2/s] b=1,NBB)
```

Cosines are indicated by a "0" in the thired column, while sines are indicated by a "1". The first line corresponds to the contribution of the radial magnetic drift to the fluxes (and it is typically the largest); other lines contain the sum of linear and quadratic terms associated to each mode. Note that the number of columns varies, depending on the number of species [NBB](#).

## 10.10 flux.knosos

File **flux.knosos**, contains flux-related quantities for one value of  $E_r$ , that may be fixed from the input or the solution of ambipolarity. The first line lists all the variables, one per column:

```
s E_r[V/m] (\Gamma_b/n_b[m/s] Q_b/n_b/T_b[m/s] L_1^b[m^2/s] L_2^b[m^2/s] n_b[10^{19}m^{-3}]
dlnn_b/dr T_b[eV] dlnT_b/dr Z_b , b=1,NBB), size(e\varphi_1/T_i)
```

Note that the number of columns varies, depending on the number of species [NBB](#).

## 10.11 knososTASK3D.ambEr

If [TASK3D](#) is set to .TRUE., KNOSOS writes in **knososTASK3D.ambEr** flux-related quantities evaluated at  $E_r$  given by ambipolarity (some of them already contained in file **flux.knosos**) in a format compatible with **TASK3D**.

## 10.12 flux.av

If [NERR](#) is greater than 0, error bars are calculated (see §[8.4](#)). File **flux.av**, contains averages and error estimates of flux-related quantities for one value of  $E_r$ , that may be fixed from the input or the solution of ambipolarity. The first line lists all the variables, one per column:

```
s E_r[V/m] err(E_r[V/m]) (\Gamma_b/n_b[m/s] err(Gamma_b/n_b)[m/s] Q_b/n_b/T_b[m/s]
err(Q_b/n_b/T_b)[m/s] , b=1,NBB)
```

Note that the number of columns varies, depending on the number of species [NBB](#).

## 10.13 imp.knosos

File **imp.knosos**, contains quantities related to the impurity flux. The first line lists all the variables, one per column:

```
s Z_z A_z Gamma_z/n_z[m/s] V_z[m/s] D_z[m^2/s] dlnn_z/dr[m^{-1}] D_{E_r}[m^2/s]
eE_r/T_z[m^{-1}] D_T[m^2/s] dlnT_z/dr[m^{-1}] D_n[m^2/s] dlnn_i/dr[m^{-1}]
Gamma_anisot/n_z[m/s]
```

In particular, the last columns allow to estimate the contribution to the flux of the impurity density gradient, the radial electric field, the temperature gradient, the main density gradient and the pressure anisotropy. The number of columns is fixed and each line corresponds to an iteration, value of  $E_r$  o impurity state.

## 10.14 ????\_2d.in

When evaluating transport of trace impurities, **KNOSOS** calculates  $\varphi_1$  and the tensor  $\overset{\leftrightarrow}{M}$  in one period. Files `ph1_2d.in`, `Mbb_2d.in`, `trM_2d.in` contain the quantities  $\varphi_1$ ,  $\overset{\leftrightarrow}{M}_1 :: \hat{b}\hat{b}$ ,  $\overset{\leftrightarrow}{M}_2 :: \hat{b}\hat{b}$  and  $tr(M_2)$  respectively, evaluated in a square grid in *left-handed* Boozer angles  $\zeta$ ,  $\theta$ . These files have a header with the flux-surface label  $s$ , the size of the grid, and the number of periods, and are written in the EUTERPE format.

# Chapter 11

## Examples

\* In this chapter, we show calculations for a variety of three-dimensional magnetic configurations in order to compare **KNOSOS** with widely-benchmarked codes and to illustrate its performance. In §11.1, we will solve a simplified drift-kinetic equation, without the magnetic drift and electric field components tangent to the flux-surface, and we will compare our results with bidimensional databases of **DKES** monoenergetic transport coefficients. The effect of the tangential magnetic drift in the energy flux, calculated for realistic kinetic profiles, will be discussed in §11.2. Finally, solutions of the quasineutrality equation will be compared with **EUTERPE** calculations in §11.3.

### 11.1 DKES-like monoenergetic transport coefficients

† In this section, we will show that **KNOSOS** can be used for creating a **DKES**-like database of monoenergetic transport coefficients at low collisionalities. We will compare our calculations with **DKES**, both in results and computing time. Let us first discuss the rationale behind the monoenergetic approach, which is not specific to **DKES**, and the particular simplifications involved in **DKES**. More details can be found in the overview paper [Beidler et al., 2011].

Predictive transport simulations solve the energy transport equation for every species:

$$\frac{3}{2} \frac{\partial n_b T_b}{\partial t} + \frac{1}{r} \frac{\partial}{\partial r} (r Q_b) = \langle P_b \rangle , \quad (11.1)$$

where  $P_b$  is the net energy input to species  $b$  and the energy flux  $Q_b$  contains a turbulent contribution, at least close to the edge, that is currently provided by simplified models [Turkin et al., 2011]. Calculating the time evolution of the energy, as in [Pedersen et al., 2015], or finding the steady-state solution as in [Geiger et al., 2015], requires evaluating the neoclassical contribution to  $Q_b$  a large number of times. The monoenergetic approach, together with some simplifications to the drift-kinetic equation, provides a way out of solving the drift-kinetic equation many times.

Strictly speaking, monoenergetic transport coefficients can always be calculated if the velocity  $v$  is a parameter in the drift-kinetic equation that is being solved, as in the case of

---

\*This chapter corresponds to section 4 of [Velasco et al., 2019].

†The input and output files of these simulations are provided in folder 'KNOSOS/TESTS/MONO', so that the user can reproduce them.

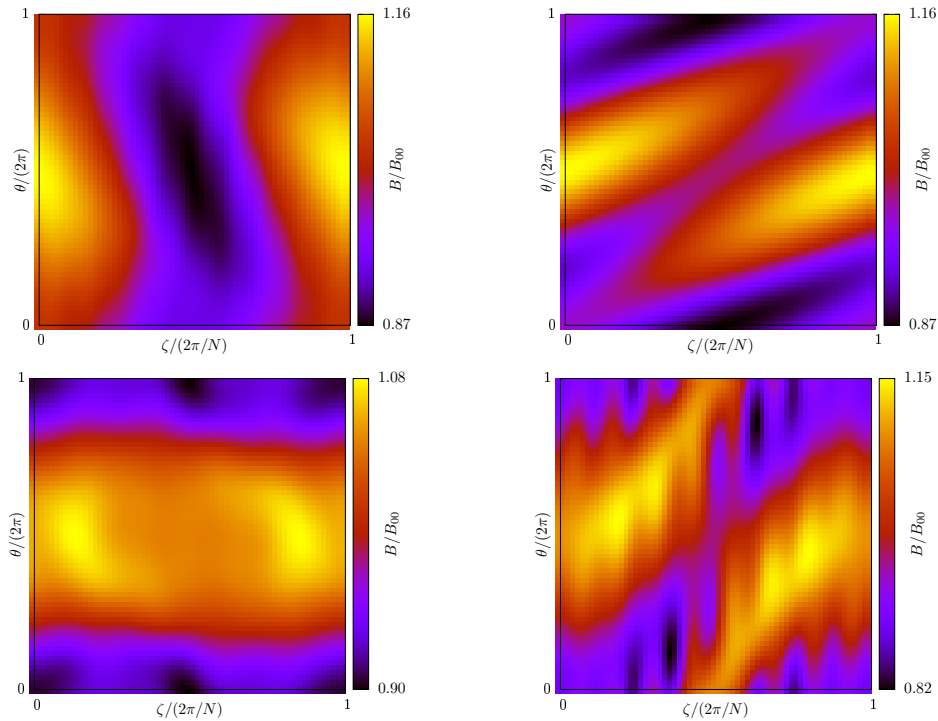


Figure 11.1: Magnetic field strength for surface  $\psi/\psi_{LCFS} = 0.5$  of the W7-X high-mirror configuration (top left), the LHD  $R_{ax} = 3.75$  m configuration (top right), an NCSX equilibrium (bottom left) and the TJ-II standard configuration (bottom right).

equation (4.1): one can rewrite

$$Q_b = \int_0^\infty dv D_{11,b} \frac{m_b v^2}{2} F_{M,b} \Upsilon_b \frac{\partial \psi}{\partial r} \quad (11.2)$$

as a *convolution* of monoenergetic transport coefficients

$$D_{11,b} = 2 \left( \frac{\partial r}{\partial \psi} \right)^2 \left\langle \int_{B_{\max}^{-1}}^{B^{-1}} d\lambda \frac{v^3 B}{|v_\parallel|} \frac{g_b}{F_{M,b} \Upsilon_b} \mathbf{v}_{D,b} \cdot \nabla \psi \right\rangle, \quad (11.3)$$

where  $g_b$  is the solution of equation (4.1). Up to this point, the reduction in computation time associated to the monoenergetic approach stems from the fact that  $v$  is a parameter in equation (4.1), which is then easier to solve than a drift-kinetic equation with energy diffusion in the collision operator.

Additionally, some fundamental simplifications are done by DKES: instead of  $Q_b$ , it calculates

$$\hat{Q}_b = \left\langle \hat{\mathbf{Q}}_b \cdot \nabla r \right\rangle = \int_0^\infty dv \hat{D}_{11,b} \frac{m_b v^2}{2} F_{M,b} \Upsilon_b \frac{\partial \psi}{\partial r}, \quad (11.4)$$

with

$$\hat{D}_{11,b} = 2 \left( \frac{\partial r}{\partial \psi} \right)^2 \left\langle \int_{B_{\max}^{-1}}^{B^{-1}} d\lambda \frac{v^3 B}{|v_\parallel|} \frac{\hat{g}_b}{F_{M,b} \Upsilon_b} \mathbf{v}_{M,b} \cdot \nabla \psi \right\rangle. \quad (11.5)$$

Here,  $\hat{g}_b$  is the solution of a modified version of equation (4.1), simplified as

$$\hat{I}_{v_{E,\alpha}}(\alpha, \lambda) \partial_\alpha \hat{g}_b + I_{v_{M,\psi}}(\alpha, \lambda) v_{d,b} F_{M,b} \Upsilon_b = \nu_{\lambda,b} \partial_\lambda [I_\nu(\alpha, \lambda) \partial_\lambda \hat{g}_b]. \quad (11.6)$$

With respect to equations (4.1) and (11.3), we have set

$$\begin{aligned} \mathbf{v}_E \cdot \nabla \psi &= 0, \\ I_{v_{M,\alpha}} &= 0, \\ I_{v_{E,\psi}} &= 0, \end{aligned} \quad (11.7)$$

and replaced  $I_{v_{E,\alpha}}$  with

$$\hat{I}_{v_{E,\alpha}} = \Psi'_t \partial_\psi \varphi_0 \int_{l_{b_1}}^{l_{b_2}} \frac{B^2}{\langle B^2 \rangle} \frac{dl}{\sqrt{1 - \lambda B}}. \quad (11.8)$$

In other words, the effect of the tangential electric field and the tangential magnetic drift is ignored, and an incompressible  $\mathbf{E} \times \mathbf{B}$  tangential drift is used (this last simplification is specific of DKES and is not used by other codes in [Beidler et al., 2011]). While it is well known [Calvo et al., 2017] that these effects need to be kept in the drift-kinetic equation for an accurate computation of the radial fluxes, there is a range of situations in which  $\hat{Q}_b \approx Q_b$  (this will be discussed in detail in §11.2) and this inaccuracy allows for a very large reduction of the computing time. The reason is that, for a given flux-surface, when normalized by the plateau value

$$\begin{aligned} \hat{D}_{11}^* &\equiv \frac{\hat{D}_{11,b}}{D_{11,b}^p}, \\ D_{11,b}^p &= \frac{\pi v_{d,b}^2 R_0}{4 v_\ell}, \end{aligned} \quad (11.9)$$

the transport coefficients  $\hat{D}_{11}^*$  only depend on two  $v$ -dependent dimensionless parameters, the collisionality

$$\nu_* = \frac{R_0 \nu_\lambda}{\iota v}, \quad (11.10)$$

and the normalized radial electric field

$$v_{E*} = \frac{E_r}{vB_{0,0}}. \quad (11.11)$$

Here,  $R_0$  is the major radius, and the main Fourier mode of  $B$  (see §4.2.2) is  $B_{0,0} \sim 1$  T in all the simulations presented in this paper. Since there is no species dependence, in the rest of the section, we follow the common practice of dropping the species index when discussing monoenergetic calculations. A predictive transport simulation thus requires to precompute a so-called database of (DKES-like) monoenergetic coefficients  $\hat{D}_{11}^*(\nu_*, v_{E*})$ . Once this is done, the calculation of  $\hat{Q}_b$  for given  $n_b$ ,  $T_b$  and  $E_r$  using equation (11.4) requires a few bidimensional interpolations and an integral in  $v$ . The problem then lies in the computation of the database  $\hat{D}_{11}^*(\nu_*, v_{E*})$  for every new magnetic configuration, which typically takes hours, due to the poor convergence of DKES (and most neoclassical codes [Beidler et al., 2011]) at low collisionalities. We will show that the bounce-average technique greatly reduces the computing time by using in KNOSOS equation (11.6) and comparing the results with DKES. Calculations without the simplifications made by DKES are left for §11.2.

In order to illustrate the performance of KNOSOS in a variety of three-dimensional configurations, we choose four very different types of stellarators. Figure 11.1 shows the map of the magnetic field strength on the flux-surface  $\psi/\psi_{LCFS} = 0.3$  of the high-mirror configuration of the helias W7-X (top left), the  $R_{ax} = 3.75$  m configuration of the heliotron LHD (top right), an equilibrium of NCSX close to quasaxisymmetry (bottom left) and the standard configuration of the heliac TJ-II (bottom right)[Ascasíbar et al., 2019].

Figure 11.2 shows the first comparisons between KNOSOS and DKES, in which the normalized monoenergetic transport coefficient  $\hat{D}_{11}^*$  is calculated for several values of the collisionality and the normalized radial electric field. Figure 11.2 (top left) contains data for the W7-X high-mirror configuration, which we discuss in more detail. The expected  $1/\nu$  dependence is observed at the highest collisionalities and, due only to the absence of tangential magnetic drift, for small values of  $v_{E*}$ . There is  $\sqrt{\nu}$  characteristic behaviour elsewhere, with smaller levels of transport for larger  $|E_r|$ . The comparison between KNOSOS and DKES is satisfactory, with agreement within the error bars of the DKES calculation, and only at the highest collisionalities, and for the largest values of  $E_r$ , there are very small differences. The calculation for all the points of this case was made with  $\mathcal{N}_\alpha = 32$  and  $\mathcal{N}_\lambda = 64$ , and it took 2.0 seconds in a single standard CPU. Of this time, around 0.7 seconds were used for setting the grid and performing the bounce-averages, and then it took less than 0.04 seconds to calculate each point. This number may be reduced even further using smaller  $\mathcal{N}_\lambda$  for the cases of largest collisionality and smallest radial electric field. In the  $\sqrt{\nu}$  regime, transport is given by a small layer close to the boundary between passing and trapped particles. The size in  $\lambda$  of this layer is proportional to  $\sqrt{\nu_\lambda/E_r}$  [Calvo et al., 2017], and this determines the required number of grid points  $\mathcal{N}_\lambda$  in the low collisionality cases with radial electric field.

Similar results can be seen for LHD in figure 11.2 (top right).  $\mathcal{N}_\alpha = 32$  and  $\mathcal{N}_\lambda = 64$  grid points were used, and the total computation time was 2.1 seconds. For NCSX, figure 11.2 (bottom left), the agreement is good except for the higher collisionalities, where the  $1/\nu$

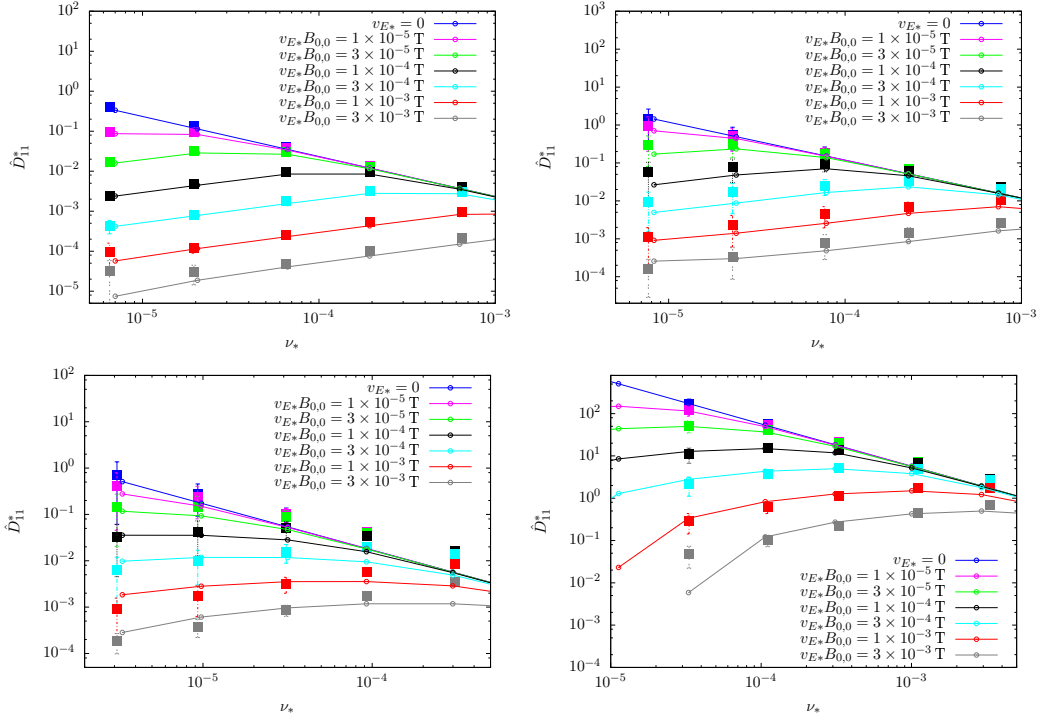


Figure 11.2: Monoenergetic transport coefficients calculated with **DKES** (full squares) and **KNOSOS** (small open circles with lines) as a function of the collisionality at  $\psi/\psi_{LCFS} = 0.5$  surface of W7-X (top left), LHD (top right), NCSX (bottom left) and TJ-II (bottom right). The colour code is:  $v_{E*}B_{0,0} = 0$  (blue),  $1 \times 10^{-5}$  T (magenta),  $3 \times 10^{-5}$  T (green),  $1 \times 10^{-4}$  T (black),  $3 \times 10^{-4}$  T (cyan),  $1 \times 10^{-3}$  T (red), and  $3 \times 10^{-3}$  T (grey).

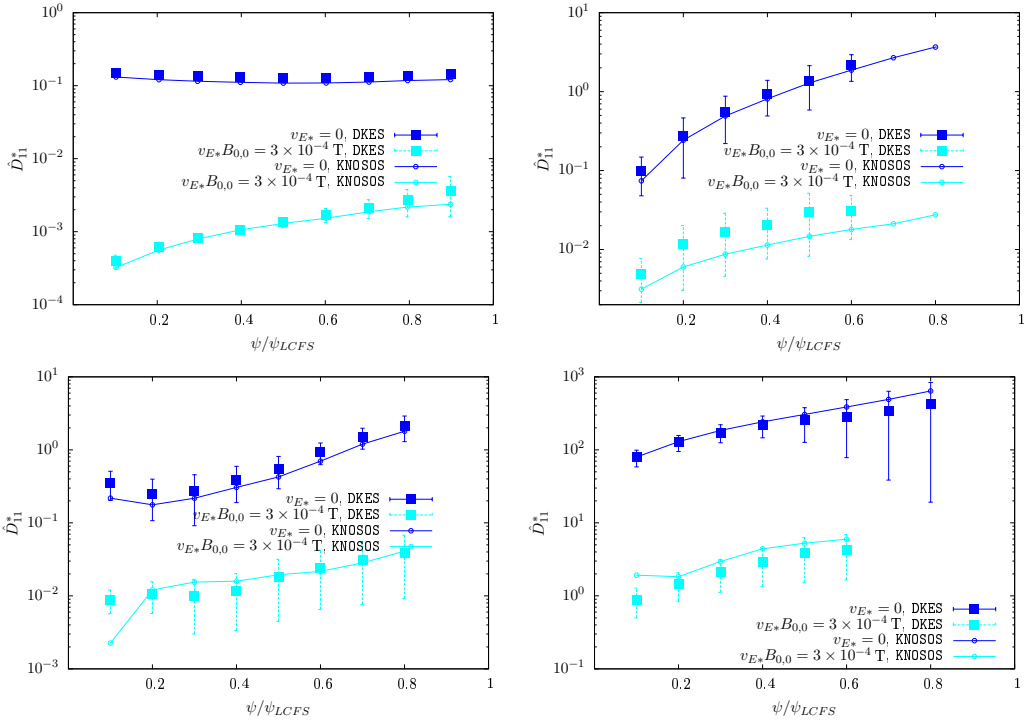


Figure 11.3: Radial profile of normalized monoenergetic transport coefficient calculated with **DKES** (full squares) and **KNOSOS** (small open circles with lines) for W7-X (top left), LHD (top right), NCSX (bottom left) and TJ-II (bottom right). Cyan corresponds to the  $\sqrt{\nu}$  regime ( $v_{E*}B_{0,0} = 3 \times 10^{-4}$  T) and blue to the  $1/\nu$  regime ( $v_{E*} = 0$ ).

regime should connect with a banana regime (see figure 15 of [Beidler et al., 2011]). This regime could be easily implemented in KNOSOS following [Landreman and Catto, 2012].  $\mathcal{N}_\alpha = 32$  and  $\mathcal{N}_\lambda = 64$  grid points were used, and the total computation time was 1.0 seconds. Finally, figure 11.2 (bottom right) contains the results for TJ-II, the hardest case due to its complicated magnetic geometry, see figure 11.1 (bottom right).  $\mathcal{N}_\alpha = 32$  and  $\mathcal{N}_\lambda = 128$  were used, and the simulation took 157 seconds. Here, one can see more clearly that the cases deeper in the  $\sqrt{\nu}$  regime are more difficult to converge, and indeed the points corresponding to  $v_{E*}B_{0,0} \geq 10^{-3}$  T and  $\nu_* < 10^{-4}$  are barely converged. The rest of the simulations agree with DKES and reach even lower collisionalities than those typically required for describing a TJ-II plasma, whose ion temperature never exceeds a few hundred eV.

Figure 11.3 contains, for each of the four configurations, radial profiles of the transport coefficient  $\hat{D}_{11}^*$  for two cases,  $v_{E*} = 0$  and  $v_{E*}B_{0,0} = 3 \times 10^{-4}$  T, for a given collisionality. They are meant to represent the level of transport in the  $1/\nu$  regime ( $\hat{D}_{11}^*$  is by definition proportional to  $\epsilon_{eff}^{3/2}$ , being  $\epsilon_{eff}$  the effective ripple) and the  $\sqrt{\nu}$  regime, respectively. We choose  $\nu_* = 2 \times 10^{-5}$  for W7-X (top left) and LHD (top right),  $\nu_* = 10^{-5}$  for NCSX (bottom left) and  $\nu_* = 3 \times 10^{-5}$  for TJ-II (bottom right). It can be observed that the good agreement holds for all cases at all radial positions. The comparison of the different parts of figure 11.3 provides additional information that may be relevant when devising a stellarator optimization strategy: in general, configurations with lower  $1/\nu$  transport show lower  $\sqrt{\nu}$  transport as well. This is not surprising considering that both quantities are connected to the bounce-averaged radial component of the magnetic drift, which appears in the source of the drift-kinetic equation (3.9) in both regimes, and which is in turn proportional to the variation of the second adiabatic invariant on the flux-surface,  $\partial_\alpha J$ . Inasmuch as the optimization procedure actually reduces the size of  $\partial_\alpha J$ , both the  $1/\nu$  and  $\sqrt{\nu}$  (and superbanana-plateau) regimes will generally be optimized. Nevertheless, using directly the effective ripple as figure of merit of neoclassical transport does not automatically guarantee a reduction of  $\partial_\alpha J$ , and the  $\sqrt{\nu}$  transport may remain unoptimized. Figure 11.3 (top) may represent an example of this situation: while this W7-X configuration is designed to have low level of  $1/\nu$  transport at an intermediate radial position (where the plasma volume is relatively large and neoclassical transport is expected to be at least comparable to anomalous transport), the  $\sqrt{\nu}$  transport is smallest exactly at the magnetic axis. We will argue the relevance of optimizing transport regimes of collisionality lower than the  $1/\nu$ , which has now become possible with KNOSOS, in the next section.

## 11.2 Effect of the tangential magnetic drift on the radial transport of energy

<sup>‡</sup> In §11.1, we have shown solutions of equation (11.6), a simplified drift-kinetic equation that is not accurate when the tangential components of the magnetic drift and of the electric field play a role. In this section, we will demonstrate the importance of solving equation (4.1) instead of equation (11.6), i.e., of computing  $Q_b$  and not  $\hat{Q}_b$ , when calculating

---

<sup>‡</sup>The input and output files of these simulations are provided in folder 'KNOSOS/TESTS/AMB', so that the user can reproduce them.

the radial energy flux in real plasmas. It must be noted that the solution of equation (4.1) with **KNOSOS** is not computationally more expensive than that of equation (11.6): in the superbanana-plateau regime, that may arise in the presence of the tangential magnetic drift for certain values of  $E_r$ , transport is dominated by a resonant layer whose size decreases with  $(\nu_\lambda/E_r)^{1/3}$ , i.e., slower than the boundary layer that determines the  $\sqrt{\nu}$  transport [Calvo et al., 2017]. Calculating  $Q_b$  instead of  $\hat{Q}_b$  does not require a larger value of  $\mathcal{N}_\lambda$  in general.

In this section, we focus on characterizing the effect of the tangential magnetic drift for the particular case of  $\varphi_1 = 0$ . We advance one of the salient results: this effect will be non-negligible even at not very low collisionalities. The reason is that the calculation of the energy flux for a given plasma, characterized by the kinetic profiles, requires the solution of the drift-kinetic equation for several values of the velocity, see equation (4.15), with the normalized particle energy  $(v/v_{th,b})^2$  spanning several orders of magnitude. This means that, even if the thermal particles are in  $1/\nu$  regime, there are particles with higher  $v$  that are in lower collisionality regimes.

Figure 11.4 contains simulations for the high-mirror configuration of W7-X at  $\psi/\psi_{LCFS} = 0.25$ , which corresponds to  $r/a = 0.5$ . We choose a pure hydrogen plasma, with  $n_e = 8.0 \times 10^{19} \text{ m}^{-3}$ ,  $\partial_r n_e/n_e = -2.0 \text{ m}^{-1}$ ,  $T_e = T_i = 4.0 \text{ keV}$ ,  $\partial_r T_e/T_e = \partial_r T_i/T_i = -3.0 \text{ m}^{-1}$ . These are values comparable to those measured in high-performance OP1.2 plasmas of W7-X [Klinger and the W7-X Team, 2019] in the region of crossover between positive and negative radial electric field, corresponding to electron and ion root solutions of the ambipolarity equation [Pablant and et al, 2019]. In these plasmas, neoclassical transport calculated neglecting the tangential magnetic drift typically accounts for around half the total experimental transport. Figure 11.4 (top) contains a plot, in logarithmic scale, of the ion and electron radial energy flux as a function of the radial electric field. Empty and full blue boxes correspond to  $\hat{Q}_i$  and  $Q_i$  respectively, both calculated with **KNOSOS**. We immediately see that  $\hat{Q}_i$  overestimates the radial energy flux at small values of the radial electric field, specially at  $E_r = 0$  (strictly the only point of the figure where  $\hat{Q}_i$  is proportional to  $\varepsilon_{eff}^{3/2}$ ). The tangential drifts make the ion flux decrease, differently in the case of  $\hat{Q}_i$  and  $Q_i$ , as we will discuss below. Finally, empty and full red boxes correspond to  $\hat{Q}_e$  and  $Q_e$  calculated with **KNOSOS**. In this plot, is difficult to notice any difference between the different electron calculations. Figure 11.4 (top) contains additional black lines that are the result of combining calculations with **DKES** and **KNOSOS**. We will leave the discussion of these results for the end of the section.

Figure 11.4 (bottom) contains a blowup in linear scale of the most relevant range of the data in figure 11.4 (top). Here, the effect of the tangential magnetic drift on the energy flux can be observed more clearly: the size of the peak at small  $|E_r|$  is reduced and displaced to positive (negative) values in the case of electrons (ions). The effect is larger for the ions due to their larger normalized Larmor radius  $\rho_{i*}$ , which makes them leave the  $1/\nu$  regimes at relatively higher collisionalities. We have mentioned that these plasmas are close to the crossover between ion and electron root, and this figure can help us discuss some features of transport in both situations. In electron root, the radial electric field is expected to be positive and large, and the electrons are expected to give the largest contribution to energy transport. According to figure 11.4 (bottom),  $Q_e$  provides a minor, although systematic, correction to  $\hat{Q}_e$ , below 10% for this plasma profiles and configuration. The situation is different in ion root, typically characterized by a negative radial electric field that is small

in size, and dominant ion transport. Here, including the tangential magnetic drift can lead to large corrections, above 50% in some cases.

For the sake of completeness, figure 11.5 contains two more cases. In figure 11.5 (top) we repeat the calculation for a W7-X plasma of much higher collisionality, choosing  $n_e = 1.6 \times 10^{20} \text{ m}^{-3}$ ,  $\partial_r n_e/n_e = -2.0 \text{ m}^{-1}$ ,  $T_e = T_i = 2.5 \text{ keV}$ ,  $\partial_r T_e/T_e = \partial_r T_i/T_i = -3.0 \text{ m}^{-1}$ . We first note that the electrons are deep in the  $1/\nu$  regime, since  $\nu_{e*} = 3.4 \times 10^{-2}$  and  $\rho_{e*} = 1.4 \times 10^{-5}$ . Nevertheless,  $Q_e(E_r)$  does not show the linear dependence expected when the  $1/\nu$  dominates. This is an indication of what we advanced at the beginning of this section: even in plasmas nominally in the  $1/\nu$  regime, the contribution of the  $\sqrt{\nu}$  regime is not negligible, and should not be neglected in the optimization procedure. For the ions, even at these higher collisionalities and low temperatures,  $\nu_{i*} = 1.6 \times 10^{-2}$  is not much larger than  $\rho_{i*} = 6.0 \times 10^{-4}$  divided by the inverse aspect ratio. This means that, for ions slightly more energetic than the thermal ions, the tangential magnetic drift is relevant at small values of  $|E_r|$  [Calvo et al., 2018b]. Figure 11.5 (top) shows indeed systematic differences between  $\hat{Q}_i$  and  $Q_i$ .

Finally, figure 11.5 (bottom) contains a calculation with the same kinetic profiles of figure 11.4 (top) for the inward-shifted configuration of LHD. It can be observed that the effects discussed in figure 11.5 (top) are even more pronounced, to the extent of changing qualitatively the  $Q_b(E_r)$  dependence (and making it more similar to that reported in [Matsuoka et al., 2015]: while practically any increase of  $|E_r|$  causes a reduction of  $Q_i$  in W7-X, this is not the case for LHD. For finite ion-root values of  $E_r$ ,  $Q_i(E_r)$  has a peak whose height is determined by superbanana-plateau transport.

In light of these results, two comments related to stellarator optimization can be made. First, the fact that the monoenergetic transport coefficients respond to small tangential  $\mathbf{E} \times \mathbf{B}$  drifts differently in the inward-shifted LHD, with respect to other configurations, was already discussed in [Beidler et al., 2011], and it can be observed more clearly when calculating the energy flux including the tangential magnetic drift. We also note that part of the neoclassical optimization of W7-X comes from its large aspect-ratio, which tends to make the tangential magnetic drift smaller, when compared with the  $E \times B$  drift. It is then clear than a systematic study of the different low-collisionality regimes, and their different configuration dependence, should be addressed when devising an stellarator optimization strategy. Second, a comprehensive optimization strategy will involve, at least, solving energy transport consistently with ambipolarity and quasineutrality. Along this section, we have compared  $Q$  and  $\hat{Q}$  at fixed  $E_r$ , but a more systematic study applied to real discharges of W7-X, including the experimental validation of  $E_r$  predictions, is ongoing [Carralero et al., 2019].

Let us finally discuss the black lines of figures 11.4 and 11.5, which correspond to combining simulations of DKES and KNOSOS. As we have argued at the beginning of this section, calculating the radial energy flux requires solving the drift-kinetic equation for velocities  $(v/v_{th,b})^2$  spanning from  $\sim 10^{-2}$  to  $\sim 10^2$ , typically. Similarly to what we discussed for  $v \gg v_{th,b}$ , this means that particles with  $v \ll v_{th,b}$  could be in the plateau regime, and they would not be described by equation (4.1). In order to quantify this effect, and to show that it is negligible for the high-performance plasmas of W7-X, we perform calculations of  $Q_i(E_r)$

and  $Q_e(E_r)$  combining KNOSOS with DKES. This can be done by rewriting equation (3.26) as

$$Q_b = D_{11,b}^p \int_0^\infty dv \left[ H(v_0 - v) \hat{D}_{11}^*(v) + H(v - v_0) D_{11}^*(v) \right] \frac{m_b v^2}{2} F_{M,b} \Upsilon_b, \quad (11.12)$$

where  $H$  is the Heaviside function,  $v_0$  is a cut-off velocity,  $\hat{D}_{11}^*(v)$  comes from DKES in this case and

$$D_{11}^*(v) = \frac{D_{11,b}}{D_{11,b}^p} \quad (11.13)$$

from KNOSOS. The latter is calculated according to equation (11.3) solving the drift-kinetic equation that is correct at low collisionalities with  $\varphi_1$  set to zero. In other words, monoenergetic transport coefficients  $\hat{D}_{11}^*$  coming from DKES are used above certain collisionality when performing the velocity integral and monoenergetic transport coefficients  $D_{11}^*$  coming from KNOSOS are used below that collisionality. The cut-off velocity  $v_0$  must correspond to particles in the  $1/\nu$  regime, which is correctly described by the two codes. This guarantees that both codes are employed in the parameter region where they are accurate (and fast).

In figures 11.4 and 11.5 (bottom), the black lines corresponding to using equation (11.12) barely separate from the solution of equation (4.1). This means that the contribution of the plateau regime to the energy flux is negligible. Only for ions in the presence of very negative values of the radial electric field, in the high-density W7-X calculation, starts the black line to separate from the blue signs. This is to be expected: due to the approximate (exact in the case of  $\hat{Q}_i$ )  $|E_r|^{-3/2}$ -dependence of the transport coefficients in the  $\sqrt{\nu}$ , the contribution of low collisionalities to transport is reduced for very large values of  $|E_r|$ , and therefore the contribution of the plateau becomes non-negligible.

### 11.3 Tangential electric field

<sup>§</sup> Neoclassical physics gives rise to  $\varphi_1$ , and the associated tangential electric field produces radial drifts in all species. This is the reason why we need to solve consistently the drift-kinetic equations of the bulk species and quasineutrality [Calvo et al., 2017], but the effect is more relevant for impurities, due to their larger charge number, changing even qualitatively transport (e.g. making it depend on the radial electric field in the so-called mixed collisionality regime [Calvo et al., 2018a; Buller et al., 2018]). With impurity transport in mind, simulations of  $\varphi_1$  for the stellarators W7-X, LHD and TJ-II have been performed in the last years with three codes, EUTERPE, SFINCS and recently FORTEC-3D [García-Regaña et al., 2013; García-Regaña et al., 2017, 2018; Mollén et al., 2018; Fujita et al., 2019]. Nevertheless, the number of simulations remains small because they are computationally very demanding, specially at low collisionalities. A more comprehensive study, including dependence on the configuration, collisionality, and bulk plasma profiles thus remains to be done. In this section, we will show that KNOSOS can reproduce the results of EUTERPE (with adiabatic electrons and no tangential magnetic drift) and, by accounting for the effect of the tangential magnetic drift, describe stellarator regimes only simulated before for simplified

---

<sup>§</sup>The input and output files of these simulations are provided in folder 'KNOSOS/TESTS/QN', so that the user can reproduce them.

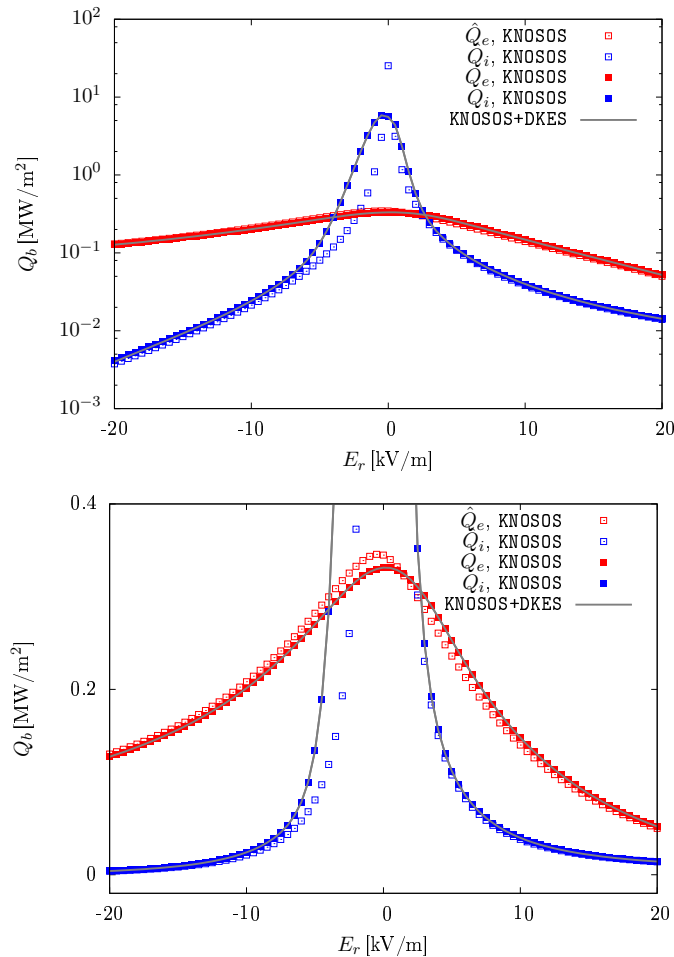


Figure 11.4: Radial energy flux as a function of the radial electric field for a W7-X high-performance plasma: logarithmic (top) and linear (bottom) scale.

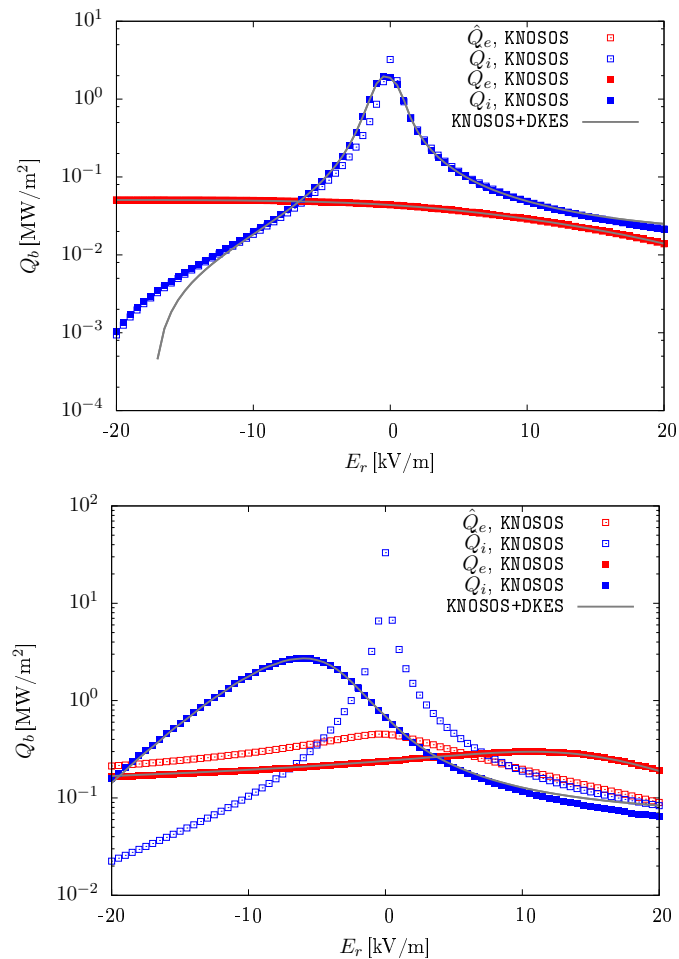


Figure 11.5: Radial energy flux as a function of the radial electric field for a W7-X high density plasma (top) and an LHD plasma (bottom).

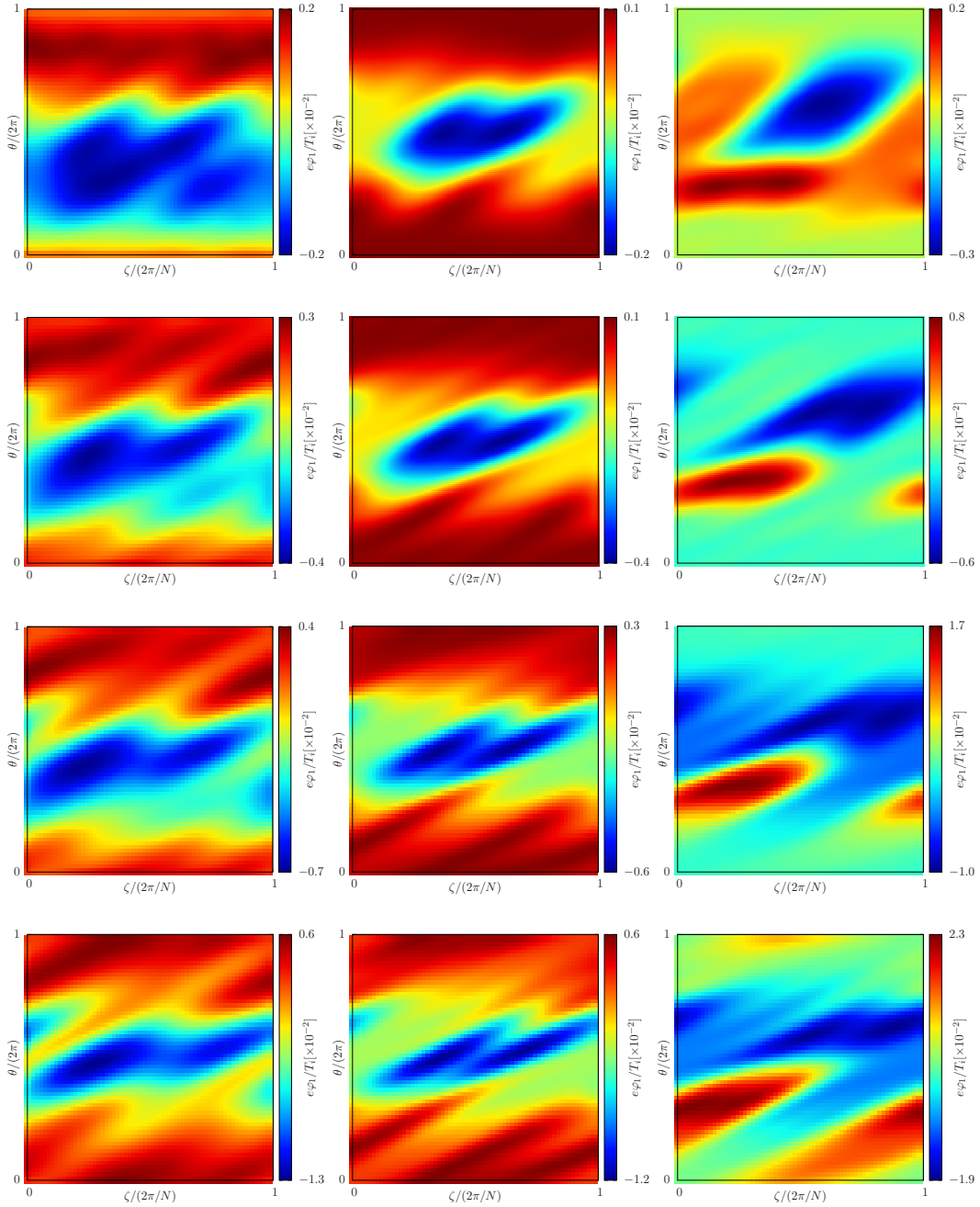


Figure 11.6: Electrostatic potential variation on the flux-surface calculated for the LHD plasma with **EUTERPE** (left) and **KNOSOS** neglecting (center) and including (right) the tangential magnetic drift. The four rows correspond to radial positions  $r/a = 0.2, 0.4, 0.6$  and  $0.8$ .

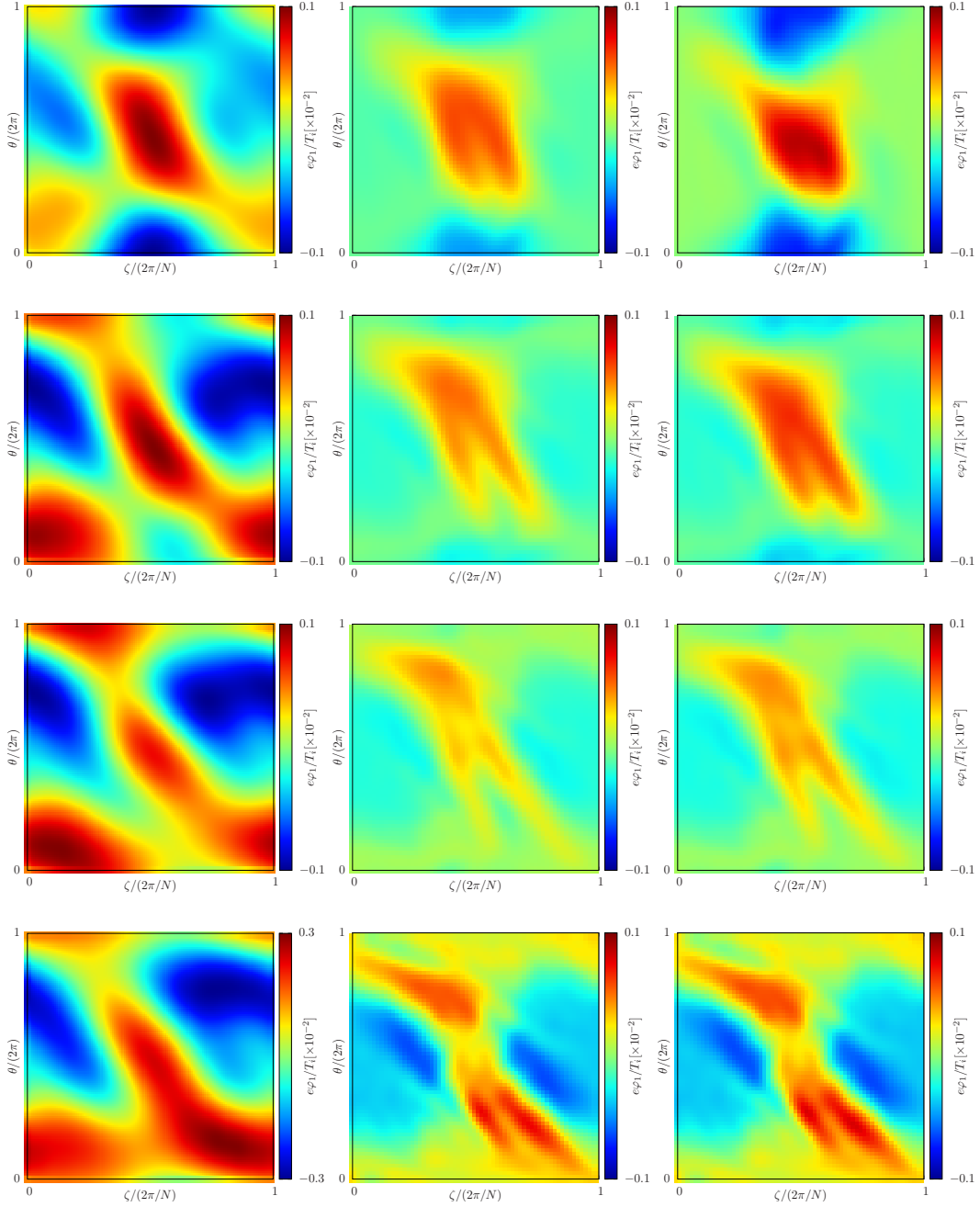


Figure 11.7: Electrostatic potential variation on the flux-surface calculated for the W7X plasma with **EUTERPE** (left) and **KNOSOS** neglecting (center) and including (right) the tangential magnetic drift. The four rows correspond to radial positions  $r/a = 0.2, 0.4, 0.6$  and  $0.8$ .

geometries [Calvo et al., 2018b; Velasco et al., 2018]. Since it can do so while keeping the computing time low, this opens the door to a number of new impurity transport studies.

We start by reproducing the results of [García-Regaña et al., 2017], specifically of two low-collisionality plasmas of LHD and W7-X. These are expected to be the plasma conditions of largest  $e\varphi_1/T_i$  so that, even in optimized magnetic configurations, the effect on the radial transport of impurities may be large. It will be confirmed (as advanced in a previous work [Velasco et al., 2018] in a simplified calculation) that the inclusion of the tangential magnetic field leads to qualitative changes in  $\varphi_1$ , making it larger. Figure 11.6 shows the variation of the electrostatic potential on several flux-surfaces of the inward-shifted configuration of LHD for a low-collisionality plasma (described in [García-Regaña et al., 2017], termed AIII, and characterized by a small negative  $E_r$ ). Each row corresponds to a different flux-surface, and each column to a different calculation method. Let us start by comparing the left column, calculated with **EUTERPE**, with the center column, calculated with **KNOSOS** using equation (11.6). The two methods should give the same results, and it can be observed that, although there are some differences, reasonable agreement between the two codes is obtained. It should be emphasized that differences in calculated values of  $\varphi_1$  similar but smaller to those reported here, have been shown to produce negligible differences in impurity transport [Velasco et al., 2018]. If we now focus on the right column, we observe, as discussed in detail in [Velasco et al., 2018], that the inclusion of the tangential produces relevant differences (in particular, more important than those between the left and center columns): the amplitude becomes larger, and the phase changes, with the angular dependence of  $\varphi_1$  turning from being stellarator-symmetric (as expected for ions in the  $\sqrt{\nu}$  regime), to not having definite symmetry (as corresponds to the superbanana-plateau regime [Calvo et al., 2018b]).

Figure 11.7 contains a similar calculation performed for a low-collisionality plasma of W7-X (described in [García-Regaña et al., 2017], termed IV, and characterized by a larger negative  $E_r$ ). Again, each row corresponds to a different flux-surface, and each column to a different calculation method. The comparison between **EUTERPE** and **KNOSOS** solving the same equation (left and center) is good close to the core, but it becomes slightly worse closer to the edge, where **KNOSOS** underestimates the amplitude of  $\varphi_1$ . When the tangential magnetic drift is included (right), the results change very slightly in the core and do not change elsewhere. This feature is likely caused by the large radial electric field, which leaves the ions in the  $\sqrt{\nu}$  regime (instead of the superbanana-plateau).

The computing time for each of these **KNOSOS** simulations is of the order of a minute in a single processor. We note that including kinetic electrons (which may be necessary for high electron temperature) would roughly double the computing time. This is to be compared with the  $(m_i/m_e)^{1/2} \approx 43$  factor in Monte Carlo codes such as **EUTERPE** and **FORTEC-3D**.

Let us finally mention that the experimental validation of  $\varphi_1$  predictions has drawn much attention in the last years: experimental measurements of  $\varphi_1$  were first obtained at the edge of the TJ-II stellarator Pedrosa et al. [2015], and very recently in its core region [Estrada et al., 2019]. The validation of **KNOSOS** predictions, including finer scans in the magnetic configuration, is left for a forthcoming work.

## Chapter 12

# Concluding remarks

\* **KNOSOS** is a freely-available open-source code that provides a fast computation of neoclassical transport at low collisionality in three-dimensional magnetic confinement devices, thanks to a rigorous application of the orbit-averaging technique to the drift-kinetic equation and an efficient solution of the quasineutrality equation. We have shown that, when solving equivalent equations, **KNOSOS** reproduces the calculations of **DKES** and **EUTERPE** in simulations that can be orders of magnitude faster. This makes it a tool that can be used for a variety of physics problems, that we summarize next.

As a first obvious application, it can provide a fast calculation of the level of transport of a magnetic configuration for low-collisionality transport regimes not usually considered in stellarator optimization, such as the  $\sqrt{\nu}$  and superbanana-plateau regimes. Optimization programmes are slowly starting to provide more accurate characterization of transport by performing predictive simulations with prescribed sources and turbulent transport models. **KNOSOS** can also contribute to overcome two of the main limitations of this approach: the large computing time needed to create a database of mononoenergetic neoclassical transport coefficients and/or the lack of accuracy involved in the monoenergetic approach itself.

But a fast neoclassical code can have uses beyond stellarator optimization. For instance, the transport of impurities caused by their interaction with the bulk ions (via  $\varphi_1$  or through inter-species collisions) has drawn much attention in the last years; however, a systematic study of its dependence on the magnetic configuration, collisionality, and bulk plasma profiles remains to be done, due to the large computing resources needed for the combined solution of the quasineutrality and drift-kinetic equations of the bulk species. This will be addressed in forthcoming papers, in combination with analytical formulas for the radial flux of impurities in a variety of neoclassical regimes [Calvo et al., 2018a, 2019].

Finally even in situations in which turbulence is dominant, a fast neoclassical code may be required. Its output (the radial electric field, the tangential electric field or the complete distribution function of the bulk species) can be read by gyrokinetic codes when studying the effect of neoclassical transport on turbulence. This effect is expected to be largest in those low-collisionality regimes in which the specificities of **KNOSOS** (very small computing time and inclusion of the tangential magnetic drift) are most relevant.

---

\*This chapter corresponds to section 5 of [Velasco et al., 2019].

# Appendix A

## High collisionalities

In this appendix we describe how the code solves transport at higher collisionalities (for which the bounce-average technique cannot be applied). For bulk species, we will recover the results of DKES (i.e., without momentum conservation), while for trace impurities we will obtain those of [Calvo et al., 2018a]\*.

### A.1 Bulk species in the Pfirsch-Schlüter regime

We repeat here the derivation of the appendix of [Igitkhanov et al., 2006]. We want to calculate  $h$ , the deviation of the distribution function from the Maxwellian, and we assume  $\varphi_1 = 0$ . The equation that we want to solve is

$$\left( vp \frac{\mathbf{B}}{B} + \frac{\mathbf{E} \times \mathbf{B}}{B^2} \right) \cdot \nabla h + \mathbf{v}_M \cdot \nabla \psi \Upsilon F_M = \frac{\nu}{2} \frac{\partial}{\partial p} \left( (1 - p^2) \frac{\partial h}{\partial p} \right). \quad (\text{A.1})$$

where we have used a simplified collision operator that is not correct at these collisionalities. The variables in velocity space are the particle speed  $v$  and the pitch-angle  $p = v_{||}/v$ . Finally, we note that, for very high collisionalities, we have to keep the  $\mathbf{E} \times \mathbf{B}$  drift.

Using the expressions derived in §9.3 for right-handed Boozzer coordinates, equation (A.1) becomes

$$\begin{aligned} & \left[ vp \frac{B}{B_\zeta + \iota B_\theta} \left( \iota \frac{\partial}{\partial \theta} + \frac{\partial}{\partial \zeta} \right) + \frac{1}{|B_\zeta + \iota B_\theta|} \frac{\partial \varphi}{\partial \psi} \left( B_\zeta \frac{\partial}{\partial \theta} - B_\theta \frac{\partial}{\partial \zeta} \right) \right] h + \\ & + v_d \frac{1 + p^2}{2} \frac{1}{B |B_\zeta + \iota B_\theta|} \left( B_\theta \frac{\partial B}{\partial \zeta} - B_\zeta \frac{\partial B}{\partial \theta} \right) \Upsilon F_M = \frac{\nu}{2} \frac{\partial}{\partial p} \left( (1 - p^2) \frac{\partial h}{\partial p} \right). \end{aligned} \quad (\text{A.2})$$

We now expand  $h$  (and  $B$ ) in Fourier components

$$h(\theta, \zeta, p) = \Upsilon F_M \sum_{m,n} h_{mn}(p) \exp[i(m\theta + nN_p\zeta)], \quad (\text{A.3})$$

and  $h_{mn}(p)$  in Legendre polynomials:

$$h_{mn}(p) = \sum_l h_{ml} P_l(p) = h_{mn0} + p h_{mn1} + \frac{1}{2} (3p^2 - 1) h_{mn2}. \quad (\text{A.4})$$

---

\*We note that these sections have not been part of any peer-reviewed paper, and it is not impossible that some of the intermediate equations contain typos

We keep only the two first polynomia since it is easy to show that

$$\int_{-1}^{+1} dp(1+p^2)P_2(p) = 0.1 \int_{-1}^{+1} dp(1+p^2)P_0(p). \quad (\text{A.5})$$

and, at large  $\nu$ ,  $h_{mn2} \ll h_{mn0}$ . We now invoke the large aspect-ratio approximation and consider variations of the magnetic field strength to be small compared to its average. In this limit

$$\begin{aligned} \frac{B}{B_\zeta + \iota B_\theta} &\approx \frac{\Psi'_t}{R}, \\ \frac{1}{B} &\approx \frac{1}{\bar{B}}, \end{aligned} \quad (\text{A.6})$$

where  $R$  is the major radius of the device and  $\bar{B}$  some average of the magnetic field strength<sup>†</sup>. The drift-kinetic equation becomes, for each Fourier component

$$\begin{aligned} i \left[ vp \frac{\Psi'_t}{R} (\iota m + n N_p) + \frac{1}{|B_\zeta + \iota B_\theta|} \frac{\partial \varphi}{\partial \psi} (m B_\zeta - n N_p B_\theta) \right] \left( h_{mn0} + p h_{mn1} + \frac{1}{2} (3p^2 - 1) h_{mn2} \right) - \\ + iv_d \frac{1+p^2}{2} \frac{1}{\bar{B} |B_\zeta + \iota B_\theta|} (n N_p B_\theta - m B_\zeta) B_{mn} = \frac{\nu}{2} (-2p h_{mn1} - 3(3p^2 - 1) h_{mn2}) \end{aligned} \quad (\text{A.7})$$

and we have to solve a system of three equations

$$\begin{aligned} i\omega_{mn} h_{mn0} + \left( -\frac{3}{2}\nu - i\frac{1}{2}\omega_{mn} \right) h_{mn2} &= iv_{d,mn}, \\ iu_{mn} h_{mn0} + (i\omega_{mn} + \nu) h_{mn1} &= 0, \\ iu_{mn} h_{mn1} + \left( \frac{9}{2}\nu + i\frac{3}{2}\omega_{mn} \right) h_{mn2} &= iv_{d,mn}, \end{aligned} \quad (\text{A.8})$$

where

$$\begin{aligned} u_{mn} &= v \frac{\Psi'_t}{R} (\iota m + n N_p), \\ \omega_{mn} &= \frac{\partial \varphi}{\partial \psi} (m B_\zeta - n N_p B_\theta), \\ v_{d,mn} &= \frac{v_d}{2} \frac{1}{\bar{B} |B_\zeta + \iota B_\theta|} (m B_\zeta - n N_p B_\theta) B_{mn}, \end{aligned} \quad (\text{A.9})$$

These equations can be combined into two:

$$\begin{aligned} iu_{mn} h_{mn1} + i3\omega_{mn} h_{mn0} &= i4v_{d,mn}, \\ iu_{mn} h_{mn0} + (i\omega_{mn} + \nu) h_{mn1} &= 0, \end{aligned} \quad (\text{A.10})$$

and we can solve for  $h_{mn0}$ , the only one that contributes the the radial flux:

$$h_{mn0} = i \frac{4v_{d,mn} u_{mn}^2 \nu}{(u_{mn}^2 - 3\omega_{mn}^2)^2 + (3\nu\omega_{mn})^2} \approx i \frac{4v_{d,mn} \nu}{u_{mn}^2 \left[ 1 + \left( \frac{3\nu\omega_{mn}}{u_{mn}^2} \right)^2 \right]}, \quad (\text{A.11})$$

---

<sup>†</sup>We take  $\bar{B} \equiv B_{00}$ .

where we have only kept the stellarator-asymmetric part and we have used that  $u_{mn}^2 \gg 3\omega_{mn}^2$ . We can now calculate the neoclassical transport coefficient  $D_{11}$  (note that we drop the species index):

$$D_{11} = -\frac{1}{2} \left( \frac{\partial r}{\partial \psi} \right)^2 \left\langle \int_{-1}^{+1} dp \frac{h}{\Upsilon F_M} \mathbf{v}_M \cdot \nabla \psi \right\rangle, \quad (\text{A.12})$$

where the brackets denote flux-surface-average. Thanks to the large aspect-ratio approximation, we can take the Jacobian to be approximately constant and obtain

$$\begin{aligned} D_{11} &\approx -\frac{1}{2} \left( \frac{\partial r}{\partial \psi} \right)^2 \frac{1}{4\pi^2} \int_0^{2\pi} d\theta \int_0^{2\pi} d\zeta \int_{-1}^{+1} dp \frac{h}{\Upsilon F_M} \mathbf{v}_M \cdot \nabla \psi = \\ &= -\frac{1}{2} \left( \frac{\partial r}{\partial \psi} \right)^2 \sum_{m,n} \int_{-1}^{+1} dp \frac{h_{mn}}{\Upsilon F_M} (\mathbf{v}_M \cdot \nabla \psi)_{-m,-n} = \sum_{m,n} (D_{11})_{mn}, \end{aligned} \quad (\text{A.13})$$

with

$$(D_{11})_{mn} \equiv -\frac{1}{2} \left( \frac{\partial r}{\partial \psi} \right)^2 \int_{-1}^{+1} dp \frac{h_{mn}}{\Upsilon F_M} (\mathbf{v}_M \cdot \nabla \psi)_{-m,-n}, \quad (\text{A.14})$$

and

$$(\mathbf{v}_M \cdot \nabla \psi)_{mn} = -i(1 + p^2) v_{d,mn}. \quad (\text{A.15})$$

Our expressions can be rewritten as

$$(D_{11})_{mn} = -\frac{16}{3} \left( \frac{\partial r}{\partial \psi} \right)^2 \frac{v_{d,mn} v_{d,-m,-n} \nu}{u_{mn}^2 \left[ 1 + \left( \frac{3\nu\omega_{mn}}{u_{mn}^2} \right)^2 \right]}. \quad (\text{A.16})$$

## A.2 Bulk species in the plateau regime

We repeat here the derivation of [Alonso et al., 2017a], and expand it to include the effect of the radial  $E \times B$  drift<sup>‡</sup>. We want to calculate  $h$ , the deviation of the distribution function from the Maxwellian, described by the next equation:

$$vp \frac{\mathbf{B}}{B} \cdot \nabla h + \nu h = -(\mathbf{v}_M + \mathbf{v}_E) \cdot \nabla \psi \Upsilon F_M. \quad (\text{A.17})$$

The variables in velocity space are again the particle speed  $v$  and the pitch-angle  $p = v_{\parallel}/v$ . In Boozer coordinates, equation (A.17) becomes, in the large aspect-ratio approximation:

$$\begin{aligned} vp \frac{\Psi'_t}{R} \left( \iota \frac{\partial}{\partial \theta} + \frac{\partial}{\partial \zeta} \right) h + \nu h &= \Upsilon F_M \frac{1}{|B_{\zeta} + \iota B_{\theta}|} \\ &\times \left[ v_d \frac{1+p^2}{2B} \left( B_{\zeta} \frac{\partial B}{\partial \theta} - B_{\theta} \frac{\partial B}{\partial \zeta} \right) + \left( B_{\zeta} \frac{\partial \varphi_1}{\partial \theta} - B_{\theta} \frac{\partial \varphi_1}{\partial \zeta} \right) \right], \end{aligned} \quad (\text{A.18})$$

---

<sup>‡</sup>Additionally, we note that the derivation of the plateau in [Alonso et al., 2017a] contains a typo that we comment on later in this section.

If we now expand  $h$ ,  $B$  and

$$\varphi_1(\theta, \zeta) = \sum_{m,n} \varphi_{1,mn} \exp [i(m\theta + nN_p\zeta)], \quad (\text{A.19})$$

in Fourier components, we have, for each component

$$vp \frac{\Psi'_t}{R} i(\imath m + nN_p) h_{mn} + \nu h_{mn} = \Upsilon F_M S_{mn}, \quad (\text{A.20})$$

with

$$S_{mn} = i \frac{(mB_\zeta - nN_p B_\theta)}{|B_\zeta + \imath B_\theta|} \left( v_d \frac{1+p^2}{2|B|} B_{mn} + \varphi_{1,mn} \right). \quad (\text{A.21})$$

We arrive to

$$\frac{h_{mn}}{\Upsilon F_M} = \frac{S_{mn}}{\frac{\Psi'_t vp}{R} i(\imath m + nN_p) + \nu} = \frac{S_{mn} \left( \nu - i \frac{\Psi'_t vp}{R} (\imath m + nN_p) \right)}{\left( \frac{vp}{R} \right)^2 (\imath m + nN_p)^2 + \nu^2}. \quad (\text{A.22})$$

Since we are going to calculate the particle and energy flux, we drop the term which is odd in  $p$ :

$$\frac{h_{mn}}{\Upsilon F_M} = \frac{S_{mn} \nu}{\left( \frac{vp}{R} \right)^2 (\imath m + nN_p)^2 + \nu^2}. \quad (\text{A.23})$$

We can rearrange this expression

$$\frac{h_{mn}}{\Upsilon F_M} = \frac{R}{v|\imath m + nN_p|} S_{mn} \frac{\nu^*}{p^2 + (\nu^*)^2}, \quad (\text{A.24})$$

where  $\nu^* = \frac{R\nu}{v|\imath m + nN_p|}$ . Since we are interested in the lowest order (i.e.  $O(\nu^0)$ ) contribution to the flux [Alonso et al., 2017a], we can use the fact that

$$\pi\delta(p) = \lim_{\nu^* \rightarrow 0} \frac{\nu^*}{p^2 + (\nu^*)^2}, \quad (\text{A.25})$$

in order to integrate in the pitch angle and obtain the final expression:

$$\begin{aligned} (D_{11})_{mn} &= \frac{\pi R}{2v|\imath m + nN_p|} \left( \frac{\partial r}{\partial \psi} \right)^2 S_{m,n} S_{-m,-n} \int_{-1}^{+1} dp (1+p^2) \frac{\nu^*}{p^2 + (\nu^*)^2} = \\ &= \frac{\pi R}{2v|\imath m + nN_p|} \left( \frac{\partial r}{\partial \psi} \right)^2 S_{m,n}(p=0) S_{-m,-n}(p=0) \end{aligned} \quad (\text{A.26})$$

The quasineutrality equation reads<sup>§</sup>

$$\begin{aligned} \left( \frac{Z_i}{T_i} + \frac{1}{T_e} \right) e\varphi_1 &= n_i \int_0^\infty dv v^2 \int_{-1}^{+1} dp h \\ &= n_i R \int_0^\infty dv v \Upsilon F_M \sum_{n,m} \frac{S_{mn}}{|\imath m + nN_p|} \end{aligned} \quad (\text{A.27})$$

<sup>§</sup>We note that there is a typo in equation (3.56) of [Alonso et al., 2017a] that leads to equation (3.58) predicting an incorrect value of  $\varphi_1$ , twice that of equation A.27

### A.3 Classical flux and neoclassical flux of trace impurities species in the presence of bulk ions at low collisionalities

Here we follow [[Calvo et al., 2018a, 2019](#)].

# Appendix B

## DKES

In this appendix, we describe how the code can read and use a database of transport coefficients calculated with DKES. This can be done not only in order to compare them with the monoenergetic transport coefficients calculated (as in §11.1) but also to use them in combination with KNOSOS(as in §11.2). The reason is that the plateau approximation of §A.2 does not work for some devices (some examples of this and some discussion can be found in [Beidler et al., 2011]).

### B.1 Input

KNOSOS can read the output summary file `results.data` generated by DKES. In order to be read, the transport coefficients must be distributed in folders and subfolders in a very precise manner. There should be `nefieldx` folders, named `omega_?e???`, corresponding to `nefieldx` values of EFIELD. Each of them should have `ncmulx` subfolders, named `cmul_?e???`, corresponding to `ncmulx` values of CMUL. For the moment, the values are hardwired in `global.f90`, and they are:

```
INTEGER, PARAMETER :: ncmulx=18
REAL*8 cmulx(ncmulx) /3E+2,1E+2,3E+1,1E+1,3E+0,1E+0,3E-1,&
&1E-1,3E-2,1E-2,3E-3,1E-3,3E-4,1E-4,3E-5,1E-5,3E-6,1E-6/
INTEGER, PARAMETER :: nefieldx=9
REAL*8 efieldx(nefieldx) /0E-0,1E-5,3E-5,1E-4,3E-4,1E-3,3E-3,1E-2,3E-2/
```

and the names of the folders and subfolders are:

```
dir_efield(1) ='omega_0e-0/'
dir_efield(2) ='omega_1e-5/'
dir_efield(3) ='omega_3e-5/'
dir_efield(4) ='omega_1e-4/'
dir_efield(5) ='omega_3e-4/'
dir_efield(6) ='omega_1e-3/'
dir_efield(7) ='omega_3e-3/'
dir_efield(8) ='omega_1e-2/'
```

---

```

dir_efield(9) ='omega_3e-2/'
dir_efield(10)='omega_1e-1/'

dir_cmul(1) ='cl_3e+2/'
dir_cmul(2) ='cl_1e+2/'
dir_cmul(3) ='cl_3e+1/'
dir_cmul(4) ='cl_1e+1/'
dir_cmul(5) ='cl_3e-0/'
dir_cmul(6) ='cl_1e-0/'
dir_cmul(7) ='cl_3e-1/'
dir_cmul(8) ='cl_1e-1/'
dir_cmul(9) ='cl_3e-2/'
dir_cmul(10)='cl_1e-2/'
dir_cmul(11)='cl_3e-3/'
dir_cmul(12)='cl_1e-3/'
dir_cmul(13)='cl_3e-4/'
dir_cmul(14)='cl_1e-4/'
dir_cmul(15)='cl_3e-5/'
dir_cmul(16)='cl_1e-5/'
dir_cmul(17)='cl_3e-6/'
dir_cmul(18)='cl_1e-6/'

```

It is not a problem if some extreme values of **EFIELD** and of **CMUL** (specifically, the largest **EFIELD** and the smallest **CMUL**) are not available in the database (i.e., the database may contain e.g. 16 values of **CMUL**, but then they must exactly go from 3E+2 to 1E-5, and they must be distributed as shown above).

## B.2 Use of DKES database

The **DKES** database is used for one or several species if the corresponding **REGB** is -1 or 0. The database stores the logarithm of the monoenergetic transport coefficients (both the upper and the lower limit that **DKES** computes [Hirshman et al., 1986]) as a function of the logarithms of **CMUL** and **EFIELD**, and bidimensional Lagrange polynomial interpolation is done (one dimensional if **EFIELD** is close enough to zero).

if **REGB** is 0, **DKES** is used at high collisionalities **KNOSOS** as low collisionalities, as discussed in detail in §11.2). Alternatively, if **REGB** is -1, the calculation proceeds as follows:

- The usual interpolation of the monoenergetic database is done.
- If **TANG\_VM** is set to .TRUE.:
  - a **KNOSOS** monoenergetic calculation is done with **TANG\_VM** set to .TRUE. and **INC\_EXB** set to .FALSE.;

- a KNOSOS monoenergetic calculation is done with `TANG_VM` set to `.FALSE.` and `INC_EXB` set to `.TRUE.`;
- the result of the latter is added to the interpolation, and the result of former is subtracted.

No momentum conservation, as in [Maaßberg et al. \[2009\]](#), is considered for the moment, since KNOSOS does not calculate other mononenergetic transport coefficients needed, but its effect on radial transport should be negligible.

### B.3 Normalization

DKES calculates the species-independent  $\Gamma_{11}$  coefficient, which is related to  $D_{11}$  via

$$\Gamma_{11} = -\frac{2}{v^3} \left( \frac{Z_b e}{m_b} \right)^2 \left( \frac{\partial \hat{r}}{\partial \psi} \right)^2 D_{11,b}, \quad (\text{B.1})$$

where  $\hat{r}$  is the radial coordinate in DKES. This yields

$$\begin{aligned} \langle \mathbf{\Gamma}_b \cdot \nabla \psi \rangle &= \pi \left( \frac{m_b}{Z_b e} \right)^2 \left( \frac{\partial \psi}{\partial \hat{r}} \right)^2 \int_0^\infty dv v^2 f_{M,b} \Gamma_{11} \Upsilon_b = \\ &= 2\pi \left( \frac{m_b}{Z_b e} \right)^2 \left( \frac{\partial \psi}{\partial \hat{r}} \right)^2 \int_0^\infty dv v^5 f_{M,b} \Gamma_{11} \Upsilon_b. \end{aligned} \quad (\text{B.2})$$

Since, when benchmarking with DKES, we will compare monoenergetic simulations for several values of the parameters `CMUL`=  $\nu/v$  and `EFIELD`=  $E_{\hat{r}}/v$ , we need to keep in mind that

$$E_{\hat{r}} = -\frac{\partial \varphi_0}{\partial \hat{r}} = -\frac{\partial \varphi_0}{\partial \psi} \frac{\partial \psi}{\partial \hat{r}} = E_\psi \frac{\partial \psi}{\partial \hat{r}}, \quad (\text{B.3})$$

and also (see chapter (3))

$$\nu = \nu_\lambda / 2. \quad (\text{B.4})$$

# Bibliography

- A Alonso, I Calvo, J M García-Regaña, and J L Velasco. Can we use the relative phase of electrostatic potential and impurity density asymmetries to control impurity transport in stellarators? In *The 1st JPP Frontiers in Plasma Physics Conference, Abbazia di Spineto, Italy*, 2017a.
- J A Alonso, I Calvo, and J L Velasco. Calculation of impurity density asymmetries and radial transport in a large aspect ratio stellarator in plateau regime. In *02/02/2013*.
- J A Alonso, C D Beidler, I Calvo, A Dinklage, Y Feng, G Fuchert, M Hirsch, M Landreman, A Langenberg, H Maaßberg, N Pablant, H Smith, J L Velasco, G Weir, D Zhang, and the W7-X Team. Ion heat transport in low-density Wendelstein 7-X plasmas. In *44th European Physical Society Conference on Plasma Physics, Belfast, United Kingdom*, 2017b.
- E. Ascasíbar, D. Alba, D. Alegre, A. Alonso, J. Alonso, F. de Aragón, A. Baciero, J.M. Barcala, E. Blanco, J. Botija, L. Bueno, S. Cabrera, E. de la Cal, I. Calvo, A. Cappa, D. Carralero, R. Carrasco, B. Carreras, F. Castejón, R. Castro, A. de Castro, G. Catalán, A.A. Chmyga, M. Chamorro, A.W. Cooper, A. Dinklage, L. Eliseev, T. Estrada, M. Ezzat, F. Fernández-Marina, J.M. Fontdecaba, L. García, I. García-Cortés, R. García-Gómez, J.M. García-Regaña, A. González-Jerez, G. Grenfell, J. Guasp, J. Hernández-Sánchez, J. Hernanz, C. Hidalgo, E. Hollmann, A. Jiménez-Denche, P. Khabanov, N. Kharchev, I. Kirpitchev, R. Kleiber, A.S. Kozachek, L. Krupnik, F. Lapayese, M. Liniers, B. Liu, D. López-Bruna, A. López-Fraguas, B. López-Miranda, J. López-Rázola, U. Losada, E. de la Luna, A. Martín de Aguilera, F. Martín-Díaz, M. Martínez-Fuentes, G. Martín-Gómez, A.B. Martín-Rojo, J. Martínez-Fernández, K.J. McCarthy, F. Medina, M. Medrano, L. Melón, A.V. Melnikov, P. Méndez, R. Merino, F.J. Miguel, B. van Milligen, A. Molinero, B. Momo, P. Monreal, S. Mulas, Y. Narushima, M. Navarro, M. Ochando, S. Ohshima, J. Olivares, E. Oyarzábal, J.L. de Pablos, L. Pacios, N. Panadero, F. Parra, I. Pastor, A. de la Peña, A. Pereira, J.R. Pinzón, A.B. Portas, E. Poveda, J.A. Quintana, F.J. Ramos, G.A. Rattá, M. Redondo, E. Rincón, L. Ríos, C. Rodríguez-Fernández, L. Rodríguez-Rodrigo, B. Rojo, A. Ros, E. Rosa, E. Sánchez, J. Sánchez, M. Sánchez, E. Sánchez-Sarabia, S. Satake, J.A. Sebastián, R. Sharma, C. Silva, E.R. Solano, A. Soletto, B.J. Sun, F.L. Tabarés, D. Tafalla, H. Takahashi, N. Tamura, A. Tolkachev, J. Vega, G. Velasco, J. L. Velasco, S. Yamamoto, and B. Zurro and. Overview of recent TJ-II stellarator results. *Nuclear Fusion*, 59(11):112019, 2019. doi: 10.1088/1741-4326/ab205e. URL <https://doi.org/10.1088%2F1741-4326%2Fab205e>.

- Satish Balay, William D. Gropp, Lois Curfman McInnes, and Barry F. Smith. Efficient management of parallelism in object oriented numerical software libraries. In E. Arge, A. M. Bruaset, and H. P. Langtangen, editors, *Modern Software Tools in Scientific Computing*, pages 163–202. Birkhäuser Press, 1997.
- Satish Balay, Shrirang Abhyankar, Mark F. Adams, Jed Brown, Peter Brune, Kris Buschelman, Lisandro Dalcin, Alp Dener, Victor Eijkhout, William D. Gropp, Dmitry Karpeyev, Dinesh Kaushik, Matthew G. Knepley, Dave A. May, Lois Curfman McInnes, Richard Tran Mills, Todd Munson, Karl Rupp, Patrick Sanan, Barry F. Smith, Stefano Zampini, Hong Zhang, and Hong Zhang. PETSc Web page. <https://www.mcs.anl.gov/petsc>, 2019a. URL <https://www.mcs.anl.gov/petsc>.
- Satish Balay, Shrirang Abhyankar, Mark F. Adams, Jed Brown, Peter Brune, Kris Buschelman, Lisandro Dalcin, Alp Dener, Victor Eijkhout, William D. Gropp, Dmitry Karpeyev, Dinesh Kaushik, Matthew G. Knepley, Dave A. May, Lois Curfman McInnes, Richard Tran Mills, Todd Munson, Karl Rupp, Patrick Sanan, Barry F. Smith, Stefano Zampini, Hong Zhang, and Hong Zhang. PETSc users manual. Technical Report ANL-95/11 - Revision 3.11, Argonne National Laboratory, 2019b. URL <https://www.mcs.anl.gov/petsc>.
- M. Barnes, F.I. Parra, and M. Landreman. stella: An operator-split, implicit-explicit delta-f-gyrokinetic code for general magnetic field configurations. *Journal of Computational Physics*, 391:365 – 380, 2019. ISSN 0021-9991. doi: <https://doi.org/10.1016/j.jcp.2019.01.025>. URL <http://www.sciencedirect.com/science/article/pii/S002199911930066X>.
- C D Beidler, M Yu Isaev, S V Kasilov, W Kernbichler, H Maaßberg S Murakami, V V Nemov, D Spong, and V Tribaldos. ICNTS-Impact of Incompressible  $E \times B$  Flow in Estimating Mono-Energetic Transport Coefficients. In *Proceedings of the 16th Int. Stellarator/Heliotron Workshop, Toki*, volume NIFS-PROC-69, page P2.O31, 2007. URL [http://www.nifs.ac.jp/itc/itc17/file/PDF\\_proceedings/poster2/P2-031.pdf](http://www.nifs.ac.jp/itc/itc17/file/PDF_proceedings/poster2/P2-031.pdf).
- C D Beidler, K Allmaier, M Yu Isaev, S V Kasilov, W Kernbichler, G O Leitold, H Maaßberg, D R Mikkelsen, S Murakami, M Schmidt, D A Spong, V Tribaldos, and A Wakasa. Benchmarking of the mono-energetic transport coefficients. Results from the International Collaboration on Neoclassical Transport in Stellarators (ICNTS). *Nuclear Fusion*, 51(7): 076001, 2011. URL <http://stacks.iop.org/0029-5515/51/i=7/a=076001>.
- A H Boozer. Transport and isomorphic equilibria. *The Physics of Fluids*, 26(2):496–499, 1983. doi: 10.1063/1.864166. URL <https://aip.scitation.org/doi/abs/10.1063/1.864166>.
- S. Buller, H. M. Smith, P. Helander, A. Mollén, S. L. Newton, and I. Pusztai. Effects of flux-surface impurity density variation on collisional transport in stellarators. *Journal of Plasma Physics*, 84(4):905840409, 2018.
- I Calvo, F I Parra, J L Velasco, and J A Alonso. Stellarators close to quasisymmetry. *Plasma Physics and Controlled Fusion*, 55(12):125014, 2013. URL <http://stacks.iop.org/0741-3335/55/i=12/a=125014>.

- I Calvo, F I Parra, J A Alonso, and J L Velasco. Optimizing stellarators for large flows. *Plasma Physics and Controlled Fusion*, 56(9):094003, 2014. URL <http://stacks.iop.org/0741-3335/56/i=9/a=094003>.
- I Calvo, F I Parra, J L Velasco, and J A Alonso. Flow damping in stellarators close to quasisymmetry. *Plasma Physics and Controlled Fusion*, 57(1):014014, 2015. URL <http://stacks.iop.org/0741-3335/57/i=1/a=014014>.
- I Calvo, F I Parra, J L Velasco, and A Alonso. The effect of tangential drifts on neoclassical transport in stellarators close to omnigeneity. *Plasma Physics and Controlled Fusion*, 59 (5):055014, 2017. URL <http://stacks.iop.org/0741-3335/59/i=5/a=055014>.
- I Calvo, F I Parra, J L Velasco, J A Alonso, and J M García-Regaña. Stellarator impurity flux driven by electric fields tangent to magnetic surfaces. *Nuclear Fusion*, 58(12):124005, 2018a. URL <http://stacks.iop.org/0029-5515/58/i=12/a=124005>.
- I Calvo, J L Velasco, F I Parra, J A Alonso, and J M García-Regaña. Electrostatic potential variations on stellarator magnetic surfaces in low collisionality regimes. *Journal of Plasma Physics*, 84(4):905840407, 2018b.
- I Calvo, F I Parra, J L Velasco, and J M García-Regaña. Impact of main ion pressure anisotropy on stellarator impurity transport. *Nuclear Fusion*, <https://arxiv.org/abs/1907.08482>, 2019. URL <https://arxiv.org/abs/1907.08482>.
- D Carralero, T Estrada, T Windisch, J L Velasco, J A Alonso, M Beurskens, S Bozhenkov, H Damm, G Fuchert, E Pasch, G Weir, and the W7-X Team. First V-band Doppler reflectometer results from the OP1.2b campaign in Wendelstein 7-X. In *14th International Reflectometry Workshop, Lausanne, Switzerland*, 2019.
- J R Cary and S G Shasharina. Helical plasma confinement devices with good confinement properties. *Physical Review Letters*, 78:674–677, 1997. URL <http://link.aps.org/doi/10.1103/PhysRevLett.78.674>.
- A Dinklage and the W7-X Team. Magnetic configuration effects on the Wendelstein 7-X stellarator. *Nature Physics*, 14(8):855–860, 2018. doi: 10.1038/s41567-018-0141-9. URL <https://doi.org/10.1038/s41567-018-0141-9>.
- A Dinklage, M Yokoyama, K Tanaka, J L Velasco, D López-Bruna, C D Beidler, S Satake, E Ascasíbar, J Arévalo, J Baldzuhn, Y Feng, D Gates, J Geiger, K Ida, M Jakubowski, A López-Fraguas, H Maassberg, J Miyazawa, T Morisaki, S Murakami, N Pablant, S Kobayashi, R Seki, C Suzuki, Y Suzuki, Yu Turkin, A Wakasa, R Wolf, H Yamada, M Yoshinuma, LHD Exp. Group, TJ-II Team, and W7-AS Team. Inter-machine validation study of neoclassical transport modelling in medium- to high-density stellarator-heliotron plasmas. *Nuclear Fusion*, 53(6):063022, 2013. URL <http://stacks.iop.org/0029-5515/53/i=6/a=063022>.
- T Estrada, E Sánchez, J M García-Regaña, J A Alonso, E Ascasíbar, I Calvo, A Cappa, D Carralero, C Hidalgo, M Liniers, I Pastor, and J L Velasco. Turbulence and perpendicular plasma flow asymmetries measured at TJ-II plasmas. *Nuclear Fusion*, 59:076021,

2019. doi: 10.1088/1741-4326/ab1940. URL <https://doi.org/10.1088%2F1741-4326%2Fab1940>.
- G. Fuchert, S.A. Bozhenkov, N. Pablant, K. Rahbarnia, Y. Turkin, A. Alonso, T. Andreeva, C.D. Beidler, M. Beurskens, A. Dinklage, J. Geiger, M. Hirsch, U. Höfel, J. Knauer, A. Langenberg, H.P. Laqua, H. Niemann, E. Pasch, T. Sunn Pedersen, T. Stange, J. Svensson, H. Trimino Mora, G.A. Wurden, D. Zhang, and R.C. Wolf and. Global energy confinement in the initial limiter configuration of Wendelstein 7-X. *Nuclear Fusion*, 58(10):106029, aug 2018. doi: 10.1088/1741-4326/aad78b. URL <https://doi.org/10.1088%2F1741-4326%2Faad78b>.
- K Fujita, S Satake, R Kanno, M Nunami, M Nakata, and J M García-Rega na. Global effects on the variation of ion density and electrostatic potential on the flux surface in helical plasmas. *Plasma and Fusion Research*, 14:3403102, 2019.
- J M García-Regaña, R Kleiber, C D Beidler, Y Turkin, H Maassberg, and P Helander. On neoclassical impurity transport in stellarator geometry. *Plasma Physics and Controlled Fusion*, 55(7):074008, 2013. URL <http://stacks.iop.org/0741-3335/55/i=7/a=074008>.
- J M García-Regaña, T Estrada, I Calvo, J L Velasco, J A Alonso, D Carralero, R Kleiber, M Landreman, A Mollén, E Sánchez, C Slaby, TJ-II Team, and W7-X Team. On-surface potential and radial electric field variations in electron root stellarator plasmas. *Plasma Physics and Controlled Fusion*, 60(10):104002, 2018. URL <http://stacks.iop.org/0741-3335/60/i=10/a=104002>.
- J.M. García-Regaña, C.D. Beidler, R. Kleiber, P. Helander, A. Mollén, J.A. Alonso, M. Landreman, H. Maassberg, H.M. Smith, Y. Turkin, and J.L. Velasco. Electrostatic potential variation on the flux surface and its impact on impurity transport. *Nuclear Fusion*, 57 (5):056004, 2017. URL <http://stacks.iop.org/0029-5515/57/i=5/a=056004>.
- J Geiger, C D Beidler, Y Feng, H Maassberg, N B Marushchenko, and Y Turkin. Physics in the magnetic configuration space of W7-X. *Plasma Physics and Controlled Fusion*, 57 (1):014004, 2015. URL <http://stacks.iop.org/0741-3335/57/i=1/a=014004>.
- S P Hirshman and J C Whitson. Steepest-descent moment method for three-dimensional magnetohydrodynamic equilibria. *The Physics of Fluids*, 26(12):3553–3568, 1983. doi: 10.1063/1.864116. URL <https://aip.scitation.org/doi/abs/10.1063/1.864116>.
- S P Hirshman, K C Shaing, W I van Rij, C O Beasley, and E C Crume. Plasma transport coefficients for nonsymmetric toroidal confinement systems. *Physics of Fluids*, 29(9): 2951–2959, 1986. URL <http://link.aip.org/link/?PFL/29/2951/1>.
- Darwin D.-M. Ho and Russell M. Kulsrud. Neoclassical transport in stellarators. *The Physics of Fluids*, 30(2):442–461, 1987. doi: 10.1063/1.866395. URL <https://aip.scitation.org/doi/abs/10.1063/1.866395>.
- Y Igitkhanov, E Polunovsky, and C D Beidler. Impurity dynamics in nonaxisymmetric plasmas. *Fusion science and technology*, 50(2):268, 2006. URL <http://pubs.ans.org/?a=1245>.

- W Kernbichler, S Kasilov, G Kupper, A Martitsch, V Nemov, C Albert, and M Heyn. Solution of drift kinetic equation in stellarators and tokamaks with broken symmetry using the code NEO-2. *Plasma Physics and Controlled Fusion*, 58:104001, 2016.
- T. Klinger and the W7-X Team. Overview of first Wendelstein 7-X high-performance operation. *Nuclear Fusion*, 59(11):112004, 2019. doi: 10.1088/1741-4326/ab03a7. URL <https://doi.org/10.1088%2F1741-4326%2Fab03a7>.
- T Klinger, A Alonso, S Bozhenkov, R Burhenn, A Dinklage, G Fuchert, J Geiger, O Grulke, A Langenberg, M Hirsch, G Kocsis, J Knauer, A Krämer-Flecken, H Laqua, S Lazer son, M Landreman, H Maafberg, S Marsen, M Otte, N Pablant, E Pasch, K Rahbarnia, T Stange, T Szepesi, H Thomsen, P Traverso, J L Velasco, T Wauters, G Weir, T Windisch, and the Wendelstein 7-X Team. Performance and properties of the first plasmas of Wendelstein 7-X. *Plasma Physics and Controlled Fusion*, 59(1):014018, 2017. URL <http://stacks.iop.org/0741-3335/59/i=1/a=014018>.
- Mike Kotschenreuther, G. Rewoldt, and W.M. Tang. Comparison of initial value and eigenvalue codes for kinetic toroidal plasma instabilities. *Computer Physics Communications*, 88(2):128 – 140, 1995. ISSN 0010-4655. doi: [https://doi.org/10.1016/0010-4655\(95\)00035-E](https://doi.org/10.1016/0010-4655(95)00035-E). URL <http://www.sciencedirect.com/science/article/pii/001046559500035E>.
- M Landreman and P J Catto. Omnigenity as generalized quasisymmetry. *Physics of Plasmas*, 19:056103, 2012.
- M Landreman and D R Ernst. New velocity-space discretization for continuum kinetic calculations and Fokker–Planck collisions. *Journal of Computational Physics*, 243:130 – 150, 2013. ISSN 0021-9991. doi: <https://doi.org/10.1016/j.jcp.2013.02.041>. URL <http://www.sciencedirect.com/science/article/pii/S0021999113001605>.
- M Landreman, H Smith, A Mollén, and P Helander. Comparison of particle trajectories and collision operators for collisional transport in nonaxisymmetric plasmas. *Physics of Plasmas*, 21(4):042503, 2014. URL <http://scitation.aip.org/content/aip/journal/pop/21/4/10.1063/1.4870077>.
- H Maafberg, C D Beidler, and E E Simmet. Density control problems in large stellarators with neoclassical transport. *Plasma Physics and Controlled Fusion*, 41(9):1135, 1999. URL <http://stacks.iop.org/0741-3335/41/i=9/a=306>.
- H Maafberg, C D Beidler, and Y Turkin. Momentum correction techniques for neoclassical transport in stellarators. *Physics of Plasmas*, 16(7):072504, 2009. URL <http://link.aip.org/link/?PHP/16/072504/1>.
- Seikichi Matsuoka, Shinsuke Satake, Ryutaro Kanno, and Hideo Sugama. Effects of magnetic drift tangential to magnetic surfaces on neoclassical transport in non-axisymmetric plasmas. *Physics of Plasmas*, 22(7):072511, 2015. doi: 10.1063/1.4923434. URL <http://dx.doi.org/10.1063/1.4923434>.

- A Mollén, M Landreman, H M Smith, J M García-Regaña, and M Nunami. Flux-surface variations of the electrostatic potential in stellarators: impact on the radial electric field and neoclassical impurity transport. *Plasma Physics and Controlled Fusion*, 60(8):084001, 2018. URL <http://stacks.iop.org/0741-3335/60/i=8/a=084001>.
- H E Mynick, T K Chu, and A H Boozer. Class of model stellarator fields with enhanced confinement. *Physics Review Letters*, 48:322–326, 1982. URL <http://link.aps.org/doi/10.1103/PhysRevLett.48.322>.
- V V Nemov, S V Kasilov, W Kernbichler, and M F Heyn. Evaluation of  $1/\nu$  neoclassical transport in stellarators. *Physics of Plasmas*, 6:4622, 1999.
- N A Pablant and et al. Investigations of the role of neoclassical transport in ion-root plasmas on W7-X. *Nuclear Fusion*, submitted, 2019.
- F I Parra, I Calvo, P Helander, and M Landreman. Less constrained omnigenous stellarators. *Nuclear Fusion*, 55:033005, 2015.
- T Sunn Pedersen, T Andreeva, H-S Bosch, S Bozhenkov, F Effenberg, M Endler, Y Feng, D A Gates, J Geiger, D Hartmann, H Höibe, M Jakubowski, R König, HP Laqua, S Lazerson, M Otte, M Preynas, O Schmitz, T Stange, Y Turkin, and the W7-X Team. Plans for the first plasma operation of Wendelstein 7-X. *Nuclear Fusion*, 55(12):126001, 2015. URL <http://stacks.iop.org/0029-5515/55/i=12/a=126001>.
- M A Pedrosa, J A Alonso, J M García-Regaña, C Hidalgo, J L Velasco, I Calvo, C Silva, and P Helander. Electrostatic potential variations along flux surfaces in stellarators. *Nuclear Fusion*, 55(5):052001, 2015. URL <http://stacks.iop.org/0029-5515/55/i=5/a=052001>.
- W H Press, S A Teukolsky, W T Vetterling, and B P Flannery. *Numerical Recipes in Fortran 77: the Art of Scientific Computing. Second Edition*, volume 1. Cambridge University Press, 1996. ISBN 052143064X.
- A Sagara, Y Igitkhanov, and F Najmabadi. Review of stellarator/heliotron design issues towards mfe demo. *Fusion Engineering and Design*, 85(7):1336 – 1341, 2010. ISSN 0920-3796. doi: <https://doi.org/10.1016/j.fusengdes.2010.03.041>. URL <http://www.sciencedirect.com/science/article/pii/S0920379610001122>. Proceedings of the Ninth International Symposium on Fusion Nuclear Technology.
- R Sanchez, S P Hirshman, A S Ware, L A Berry, and D A Spong. Ballooning stability optimization of low-aspect-ratio stellarators. *Plasma Physics and Controlled Fusion*, 42 (6):641, 2000. URL <http://stacks.iop.org/0741-3335/42/i=6/a=303>.
- S Satake, M Okamoto an N Nakajima, H Sugama, and M Yokoyama. Non-local simulation of the formation of neoclassical ambipolar electric field in non-axisymmetric configurations. *Plasma and Fusion Research*, 1:002, 2006. URL [https://www.jstage.jst.go.jp/article/pfr/1/0/1\\_0\\_002/\\_article](https://www.jstage.jst.go.jp/article/pfr/1/0/1_0_002/_article).

- S Satake, S Matsuoka, J L Velasco, I Calvo, and M Honda. Effect of magnetic shear and the finite banana-orbit width on the neoclassical toroidal viscosity in perturbed tokamaks . In *27th IAEA Fusion Energy Conference (FEC 2018)*, 2018.
- D A Spong. Generation and damping of neoclassical plasma flows in stellarators. *Physics of Plasmas*, 12(5):056114, 2005. URL <http://link.aip.org/link/?PHP/12/056114/1>.
- T Sunn-Pedersen, M Otte, S Lazerson, P Helander, S Bozhenkov, C Biedermann, T Klinger, R Wolf, H S Bosch, and the Wendelstein 7-X Team. Confirmation of the topology of the Wendelstein 7-X magnetic field to better than 1:100,000. *Nature Communications*, 7 (13493), 2016.
- Y. Takeiri and the LHD team. Extension of the operational regime of the LHD towards a deuterium experiment. *Nuclear Fusion*, 57(10):102023, 2017. URL <http://stacks.iop.org/0029-5515/57/i=10/a=102023>.
- Y Turkin, C D Beidler, H Maaßberg, S Murakami, V Tribaldos, and A Wakasa. Neoclassical transport simulations for stellarators. *Physics of Plasmas*, 18(2):022505, 2011. URL <http://link.aip.org/link/?PHP/18/022505/1>.
- B. Ph. van Milligen, T. Estrada, E. Ascacíbar, D. Tafalla, D. López-Bruna, A. López Fraguas, J. A. Jiménez, I. García-Cortés, A. Dinklage, and R. Fischer. Integrated data analysis at TJ-II: The density profile. *Review of Scientific Instruments*, 82(7):073503, 2011. URL <http://dx.doi.org/10.1063/1.3608551>.
- J L Velasco, K Allmaier, A López Fraguas, C D Beidler, H Maaßberg, W Kernbichler, F Castejón, and J A Jiménez. Calculation of the bootstrap current profile for the TJ-II stellarator. *Plasma Physics and Controlled Fusion*, 53(11):115014, 2011. URL <http://stacks.iop.org/0741-3335/53/i=11/a=115014>.
- J L Velasco, I Calvo, J M García-Regaña, F I Parra, S Satake, J A Alonso, and the LHD team. Large tangential electric fields in plasmas close to temperature screening. *Plasma Physics and Controlled Fusion*, 60(7):074004, 2018. URL <http://stacks.iop.org/0741-3335/60/i=7/a=074004>.
- J L Velasco, I Calvo, F I Parra, and J M García-Regaña. KNOSOS: a fast orbit-averaging neoclassical code for arbitrary stellarator geometry. *Journal of Computational Physics*, submitted, <https://arxiv.org/abs/1908.11615>, 2019.
- R C Wolf and et al. Major results from the first plasma campaign of the Wendelstein 7-X stellarator. *Nuclear Fusion*, 57(10):102020, 2017. URL <http://stacks.iop.org/0029-5515/57/i=10/a=102020>.
- H Yamada, JH Harris, A Dinklage, E Ascacíbar, F Sano, S Okamura, J Talmadge, U Stroth, A Kus, S Murakami, M Yokoyama, CD Beidler, V Tribaldos, KY Watanabe, and Y Suzuki. Characterization of energy confinement in net-current free plasmas using the extended International Stellarator Database. *Nuclear Fusion*, 45(12):1684, 2005. URL <http://stacks.iop.org/0029-5515/45/i=12/a=024>.

M. Yokoyama, R. Seki, C. Suzuki, M. Sato, M. Emoto, S. Murakami, M. Osakabe, T.Ii. Tsujimura, Y. Yoshimura, T. Ido, K. Ogawa, S. Satake, Y. Suzuki, T. Goto, K. Ida, N. Pablot, D. Gates, F. Warmer, P. Vincenzi, and and. Extended capability of the integrated transport analysis suite, TASK3D-a, for LHD experiment. *Nuclear Fusion*, 57(12):126016, 2017. doi: 10.1088/1741-4326/aa800a. URL <https://doi.org/10.1088%2F1741-4326%2Faa800a>.

M C Zarnstorff, L A Berry, A Brooks, E Fredrickson, G-Y Fu, S Hirshman, S Hudson, L-P Ku, E Lazarus, D Mikkelsen, D Monticello, G H Neilson, N Pomphrey, A Reiman, D Spong, D Strickler, A Boozer, W A Cooper, R Goldston, R Hatcher, M Isaev, C Kessel, J Lewandowski, J F Lyon, P Merkel, H Mynick, B E Nelson, C Nuehrenberg, M Redi, W Reiersen, P Rutherford, R Sanchez, J Schmidt, and R B White. Physics of the compact advanced stellarator NCSX. *Plasma Physics and Controlled Fusion*, 43(12A):A237–A249, 2001. doi: 10.1088/0741-3335/43/12a/318. URL <https://doi.org/10.1088%2F0741-3335%2F43%2F12a%2F318>.